

See discussions, stats, and author profiles for this publication at: <https://www.researchgate.net/publication/234628366>

# Electron Microscopy, Nanoscopy and Scanning Micro-and Nanoanalysis

Chapter · September 2012

DOI: 10.1002/9780470027318.a2506.pub2

---

CITATIONS

5

---

READS

651

3 authors, including:



Vladimir P Oleshko

National Institute of Standards and Technology

157 PUBLICATIONS 1,481 CITATIONS

SEE PROFILE

# Electron Microscopy, Nanoscopy, and Scanning Micro- and Nanoanalysis

**Vladimir P. Oleshko**

*National Institute of Standards and Technology,  
Gaithersburg, MD, USA*

**Renaat Gijbels**

*University of Antwerp, Antwerp, Belgium*

**Severin Amelinckx\***

*EMAT, University of Antwerp, Antwerp, Belgium*

<b>1 Introduction</b>	<b>2</b>
1.1 Electron Microscopy and Nanoscopy: Subject, Advantages, and Limitations	2
1.2 Short History and Stages of Development	3
<b>2 Theory and Instrumentation</b>	<b>3</b>
2.1 Electron–Solid Interactions	3
2.2 Diffraction by Crystals	6
2.3 Inelastic Scattering Processes	14
2.4 Auger Electrons	14
2.5 X-rays	15
2.6 Cathodoluminescence	17
2.7 Overview of Instrumentation	17
<b>3 Analytical Methods</b>	<b>23</b>
3.1 X-ray Emission Spectrometry in the Transmission Electron Microscopy, Scanning Transmission Electron Microscopy, and Scanning Electron Microscopy Modes	23
3.2 Cathodoluminescence Spectroscopy in the Scanning Electron Microscopy, Scanning Transmission Electron Microscopy, and Transmission Electron Microscopy Modes	25
3.3 Energy-filtering Transmission Electron Microscopy and Electron Energy-Loss Spectroscopy	25
<b>4 In Situ Electron Microscopy</b>	<b>26</b>

<b>5 Special Modes (Holography and Tomography)</b>	<b>26</b>
<b>6 Digital Image Analysis</b>	<b>27</b>
<b>7 Sample Preparation Techniques</b>	<b>27</b>
<b>8 Quantification</b>	<b>27</b>
8.1 X-ray Microanalysis	27
8.2 Quantitative Electron Energy-Loss Spectroscopy	31
<b>9 Applications</b>	<b>33</b>
9.1 In Situ Real-Time Environmental Transmission Electron Microscopy of Gas Phase Ziegler–Natta Catalytic Polymerization of Propylene	33
9.2 Electron Tweezers	33
9.3 Automated Population Analysis: Size–Thickness–Elemental Composition	34
9.4 X-ray and Electron Energy-Loss Spectroscopic Imaging	36
9.5 Sample Thickness Determination	38
<b>10 Current Trends</b>	<b>38</b>
<b>Acknowledgments</b>	<b>40</b>
<b>Abbreviations and Acronyms</b>	<b>40</b>
<b>Related Articles</b>	<b>41</b>
<b>References</b>	<b>41</b>

*The article considers the history and stages of development of electron microscopy (EM) and scanning microanalysis, including theoretical aspects of electron beam–solid interactions, instrumentation, methodology of particular techniques and image analysis, sample preparation, and some typical applications as well. Major classes of EM techniques, i.e. stationary beam (transmission) and scanning beam EM methods, analytical electron microscopy (AEM), in situ EM, holography, and tomography are overviewed. In AEM, several imaging, diffraction, and analytical modes are integrated in a design to provide analytical synergism having obvious advantages over any single instrument. The subject of EM is to determine the morphology, crystallinity, defect structure, phase and elemental compositions, and electronic properties of a material using the focused electron beam and signals generated in the course of its interaction with the specimen. Various electron–specimen interactions generate a great deal of structural and analytical information in the form of emitted electrons and/or photons and internally*

Update based on the original article by Vladimir Oleshko, Renaat Gijbels and Severin Amelinckx, *Encyclopedia of Analytical Chemistry*, © 2000, John Wiley & Sons, Ltd

\* This article is dedicated to the memory of the late Professor Emeritus Severin Amelinckx.

*produced signals, such as elastically and inelastically scattered electrons, Auger electrons (AEs), X-rays, and cathodoluminescence (CL), which can be analyzed in different operating modes. Imaging of solid materials is essentially due to elastic scattering (diffraction) of electrons by the periodic arrangement of atoms in crystals (diffraction contrast) and/or interference of several diffracted and transmitted beams (phase contrast). High-resolution imaging in scanning transmission mode is possible by using incoherently scattered electrons (Z-contrast). Inelastic interactions form the basis for all chemical analytical techniques (energy-dispersive (EDS) and wavelength-dispersive (WDS) X-ray spectroscopy, electron energy-loss spectroscopy (EELS) energy-filtering transmission electron microscopy (EFTEM), AE-, and CL-spectroscopy). The introduction of aberration-corrected and monochromatic electron optics during the last decade opened a new era of nanoscopy and nanoanalysis at sub-0.1 nm lateral resolution and sub-electronvolt energy resolution levels with improved signal-to-noise ratio (SNR). Basic data characterizing the current state-of-the-art and trends in development of electron nanoscopy and nanoanalysis are presented.*

## 1 INTRODUCTION

### 1.1 Electron Microscopy and Nanoscopy: Subject, Advantages, and Limitations

Electron microscopes (EMs) constitute one of the today's largest families of optical instrumentation for materials microstructural and analytical characterization comprising more than 40 methods and associated techniques.<sup>(1,2)</sup> There are two main essentially different classes of EM techniques. In the first class, the electron probe is a stationary beam incident along a fixed direction. This incident beam can be either parallel (transmission electron microscopy (TEM), high-resolution transmission electron microscopy (HRTEM), high-voltage transmission electron microscopy (HVTEM), selected-area electron diffraction (SAED), nanobeam diffraction (NBD)), or convergent (convergent-beam electron diffraction (CBED)). The resolution is determined by the quality of the imaging optics behind the specimen. Instruments implementing these techniques are conceptually related to classical light microscopes.

In the second class of methods, a fine electron probe is scanned across the specimen and transmitted electrons (TEs) (scanning transmission electron microscopy (STEM)) or the desired excited signal such as secondary electrons (SEs) or backscattered electrons (BSEs) (scanning electron microscopy, SEM), and/or AE (Auger electron spectroscopy (AES), scanning Auger microscopy

(SAM)) are selected, detected, amplified, and used to modulate the intensity of another electron beam, which is scanned synchronously with the first one over the monitor screen. The stationary beam methods are based on image formation processes, whereas the scanning methods are essentially 'mapping' techniques. In the last case, the resolution is mainly determined by the probe size, i.e. by the probe formation electron optics. The magnification is geometric; it is determined by the ratio of the areas scanned by the electron beam on the screen and synchronously by the electron probe on the specimen.

AEM is a logical extension of a concept referred to as an *integrated modular EM system*, which combines several electron imaging and diffraction modes and a number of analytical facilities. In this concept, imaging modes (conventional transmission electron microscopy (CTEM), HRTEM, STEM, SEM, EFTEM, Lorentz microscopy, holography, and tomography), diffraction modes (SAED, CBED, and NBD), and analytical modes (EDS and WDS X-ray spectrometry, EELS and/or CL spectroscopy) are integrated in a design to provide analytical synergism having obvious advantages over any single instrument.

Moreover, the number of signals and contrast effects available in AEM often require an optimum strategy for its application to the structural and analytical characterization of specific materials. This should take into account coordination of the methods used, image processing, storage of data, separation and preparation techniques involved, and mechanisms of the electron beam-specimen interactions and solid-state models of the material under study.<sup>(1–5)</sup> The potential of AEM has become exploited intensively with the development of nanochemistry and emerging nanotechnologies related primarily to cluster-matter (cluster-produced thin films, nanocrystalline materials) and cluster-matrix systems (metal-nonmetal systems, granular superconductors, cluster tunnel junctions, cermets, nanocatalysts, energy materials, biocompatible hybrid systems, etc.).

The purpose of AEM is to determine both qualitatively and quantitatively the morphology, crystallinity, defect structure, phase and elemental compositions, and electronic properties of a material at lateral spatial resolutions down to 0.1 nm within a single instrument using the focused electron beam and signals generated in the course of its interaction with the specimen. In principle, because of the common origin of the interactions of fast electrons with a solid, all electron beam-based analytical techniques such as electron probe X-ray microanalysis (EPXMA), analytical SEM, and AES/SAM may be associated with AEM.<sup>(3–6)</sup>

With multipole-based aberration correctors, monochromators, and the improved stability in EM, medium-voltage (200–300 kV) S/TEMs developed during the last

decade achieve image resolution at or below 0.1 nm and sub-electronvolt energy resolution with improved SNR, thus entering the era of nanoscopy and nanoanalysis.

Since inelastic scattering of the incident electrons causes radiation damage, EM methods, and EM in general, are destructive, although the extent of the damage is influenced by the electron dose needed to collect a useful signal, which in its turn depends on the instrumental performance. Moreover, TEM techniques require very thin specimens, which often implies cutting and thinning.

## 1.2 Short History and Stages of Development

On the basis of the discovery of the electron<sup>(7)</sup> and new laws of quantum physics at the beginning of the twentieth century, the first prototype TEM was built by Ruska and Knoll in 1931 and the physical principles of the SEM were demonstrated by Knoll (1935) and von Ardenne (1937). Since then, EM methods in various forms have rapidly evolved into sophisticated characterization tools capable of atomic-resolution imaging and complementary diffraction modes together with nanoscale spectroscopy analyses. EM has made unique contributions to key problems in materials science, physics, chemistry, and biology, and it also plays a critical role in many industrial fields. As one of the most important innovations of the twentieth century, the invention of the EM has been recognized by the Nobel Prize in Physics in 1986. One-half of the Prize was awarded to Ernst Ruska 'for his fundamental work in electron optics, and for the design of the first electron microscope,' the other half was awarded jointly to Gerd Binnig and Heinrich Rohrer 'for their design of the scanning tunneling microscope.'<sup>(8)</sup>

Imaging and microanalysis by electrons and beam-generated X-rays and its basic concepts were first developed in the 1940–1960s.<sup>(6,9)</sup> Instruments for analytical SEM, EPXMA, TEM and STEM equipped with imaging filters, EDS and/or WDS, and EELS were successfully used for the elemental and compositional characterization of advanced materials in a variety of fields of materials science. In the mid-1960s, when the advantage of using thin foils as specimens for X-ray analyses was recognized, Duncumb<sup>(10)</sup> developed the first electron microscope microanalyzer (EMMA), which comprised a 100-keV TEM and WDS X-ray spectrometers. However, the efficiency of detection for WDS was low, and a higher beam current was required, which increased the probe size to more than 100 nm. Fortunately, an EDS instrument was invented in the early 1970s and was fitted to an AE microscope. It was placed within 1–2 cm of the probe and thus enabled one to measure a sufficiently large fraction of the X-ray flux produced by electron probes even smaller than 10 nm in diameter.

EELS records the energy distribution of electrons, i.e. TE after having interacted with a thin specimen without reflection or absorption. Hence, the interaction takes place inside the specimen, and information about its structure could be obtained by using an electrostatic or a magnetic electron spectrometer. The first low-loss EEL spectrum of 5.3-keV electrons transmitted through a thin self-supported Al foil was recorded by Rutherman.<sup>(11)</sup> Hillier and Baker<sup>(12)</sup> reported inner-shell EEL spectra: K-ionization edges of several elements and Fe L- and M-edges using the first electron microanalyzer, which could focus 25- to 75-keV electrons into a 20-nm probe. A 180° magnetic spectrometer was used to record energy losses of TE. A prism–mirror–prism energy filter incorporated into the column of a TEM instrument as proposed by Castaing and Henry<sup>(13)</sup> was applied not only to acquire EEL spectra but also to display images and diffraction patterns of a specimen at a selected energy loss. An alternative method of energy filtering is the use of an STEM instrument equipped with an electrostatic energy analyzer.<sup>(14)</sup> During the last three decades, various electrostatic and magnetic electron analyzers and energy filters (Mollenstedt analyzer, Wien filter, omega filter, mandoline filter, single-prism spectrometers, prism–mirror–prism filter, postcolumn quadrupole, and sextupole lens spectrometers/imaging filters) have been developed.<sup>(6,15,16)</sup>

AEM systems employ computer-controlled parallel electron energy-loss (PEEL) spectrometers and energy filters equipped with charge-coupled device (CCD) cameras in a combination with solid-state Si drift (SDD), Si/Li and intrinsic Ge (EDS), and crystal (WDS) detectors as well as scanning attachments fitted with multidetector systems for imaging in bright field (BF) and dark field (DF) TEM/STEM and diffraction (SAED, CBED, and NBD) modes, in SE/BSE/SEM, and in high-angle annular dark-field (HAADF) STEM modes.

## 2 THEORY AND INSTRUMENTATION

### 2.1 Electron–Solid Interactions

EM is based on the effects of elastic and inelastic scattering of an accelerated electron beam on interaction with atoms and electrons of the material to be examined.<sup>(17,18)</sup> The final signals used for image formation and for analyses are normally not the result of single scattering but of some electron diffusion caused by the gradual loss of the electron energy and by some lateral spreading, mainly due to multiple elastic large-angle scattering. Figure 1 schematically shows the most important interaction processes and signals detected in different operating modes and their information volumes

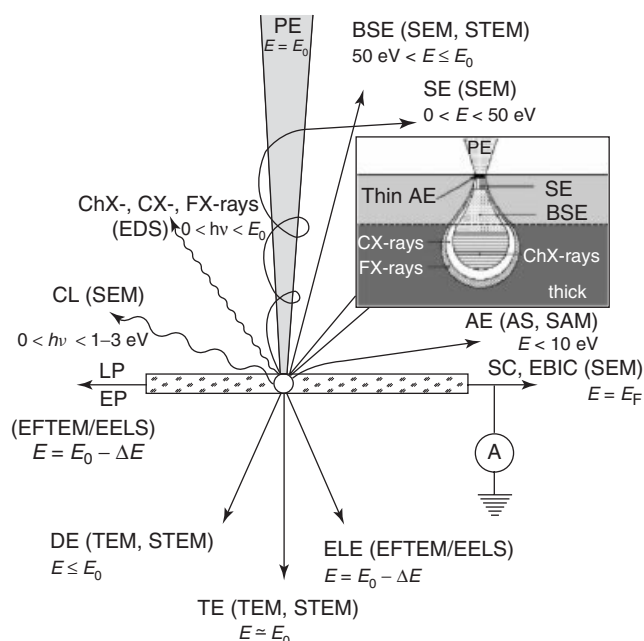


**Figure 1** Main processes of electron beam interactions and signals detected in different operating and analytical modes and schematic arrangement of their information volumes: PE, primary electrons; TE, transmitted electrons; DE, diffracted electrons; ELE, electrons with losses of energy; BSE, backscattered electrons; SE, secondary electrons; the information depth of SE is 5–50 nm; AE, Auger electrons; the information depth of AE is about 1 nm; SC, sample current; ChX-rays, characteristic X-rays; CX-rays, continuous X-rays; FX-rays, secondary X-ray fluorescence; CL, cathodoluminescence; EP, electron plasmons; and LP, lattice phonons.

(inset). The complete energy spectrum comprises primary electrons (PEs) with energy  $E_0$ , emitted electrons, ions, heat, photons, and internally generated signals: TE; wide-angle and narrow-angle elastically scattered electrons and diffracted electrons (DEs); BSE; SE; inelastically scattered electrons with loss of energy; sample current (SC) or absorbed electrons; AEs; hard and soft characteristic and continuous X-ray photons; CL; and electron plasmons (EPs) and lattice phonons (LPs).

Usually, only a comparatively small fraction of the characteristic X-rays isotropically emitted from the specimen are detected because of the small solid angle of collection ( $10^{-3}$ – $1 \text{ sr}$ ). Moreover, inner-shell ionizations result in the emission not only of X-rays but also of AE, and the X-ray fluorescence yield decreases with decreasing sample atomic number  $Z$ , even below 1% for light elements. A large fraction of about 10–70% of the inner-shell ionization processes are associated with inelastically scattered electrons concentrated in small scattering angles, which also pass through the objective aperture. Atomic electrons can be excited from an inner

shell to unoccupied energy states above the Fermi level, resulting in a characteristic edge in the EEL spectrum. Complementary to X-ray spectroscopy, in specimens with thickness of about, or smaller than, the mean-free electron path, the well-defined ionization edges for elements with atomic number  $2 \leq Z \leq 92$  can be analyzed.<sup>(6,19)</sup>

The plasmons and inelastic intra- and interband excitations of the outer shell electrons near the Fermi level that normally can be observed with energy losses  $\Delta E$  smaller than 50 eV are influenced by chemical bonds and the electronic band structure by analogy with optical excitations. In semiconductors, the electron impact results in the generation of electron–hole pairs and causes an electron beam-induced current (EBIC). Electron–hole pairs can recombine with emission of luminescent photons, either in the ultraviolet, visible, or infrared (IR) regions or by nonradiative LP. Some fraction of the  $E_0$  that is lost in the course of a cascade of inelastic scattering processes is converted into phonons and/or heat and causes radiolysis, thermal damage, bond rupture, and loss of mass and crystallinity by the sputtering of specimen matter.

Ionization of an inner electron shell by the inelastic impact results in a hole, which can be filled by an electron from a higher state. The energy difference can then be emitted either as a characteristic X-ray quantum or as an AE. Hence, the X-ray spectrum represents the transition between two energy levels, and the generated intensities are the product of the state density and the transition rate governed by the selection rules.

Since the actual mechanisms of electron–solid interactions are complicated, estimations of the information volume of generated signals based on Monte Carlo simulations (Figure 2a–c) are of importance, in particular for understanding relationships between scattered electrons and produced X-rays.<sup>(20–23)</sup> The consequence of the gradual decrease of the electron energy is that the electrons have a finite depth range of the order of several nanometers up to tens of micrometers depending on the  $E_0$  value and the thickness and density of the specimen. The depth and the lateral extent of the information volume governing the resolution of the corresponding operating modes contribute to each of the possible signals, decreasing considerably with a decrease in specimen thickness and an increase in its density. Hence, the various electron–specimen interactions can generate a great deal of structural and analytical information in the form of emitted electrons and/or photons and internally produced signals. Inelastic interactions form the basis for all chemical analytical techniques.

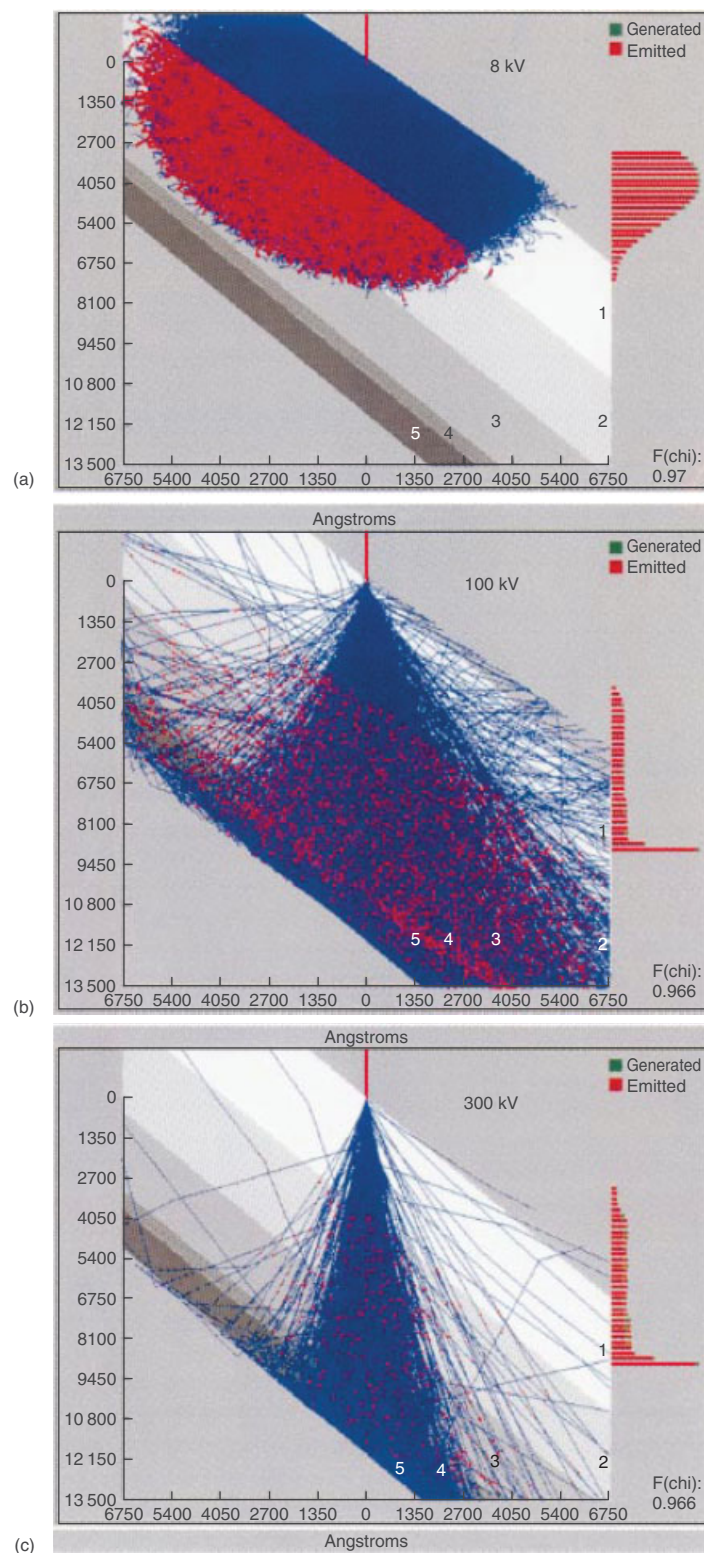


**Figure 2** Monte Carlo simulations of a lateral electron distribution (blue) and Si K $\alpha$  X-ray emission (red) in a multilayer composite film at (a) 8, (b) 100, and (c) 300 keV, 32 000 trajectories, 40° tilt. Histogram of normalized yield of Si K $\alpha$  emission,  $\phi(\rho z)$ , is plotted on the right-hand side of the graphs starting at the crystal surface; the length of bars shows the relative value of  $\phi(\rho z)$  at that depth. 1, Al, 300 nm; 2, SiO<sub>2</sub>, 250 nm; 3, Si<sub>3</sub>N<sub>4</sub>, 200 nm; 4, WSi<sub>2</sub>, 50 nm; and 5, SiO<sub>2</sub>, 100 nm. Calculations indicate a possibility of analyzing the top layer by reducing the accelerating voltage to  $\leq 8$  kV and an improvement in lateral resolution and sensitivity at 300 kV compared with 100 kV.



## 2.2 Diffraction by Crystals

### 2.2.1 Diffraction Effects: General Considerations

The complete characterization of solid compounds, especially of crystalline matter requires, apart from knowledge of the chemical composition, a description of the crystallographic features, i.e. lattice parameters, space group, and crystal structures. Moreover, a number of technologically important properties are 'structure' sensitive, i.e. they are influenced by the state of perfection and purity of the crystals and may depend on the microtexture.

Images of solid materials produced in TEM are essentially due to elastic scattering, i.e. diffraction of electrons by the periodic arrangement of atoms in crystals (diffraction contrast). Not only is diffraction responsible for the formation of the images, but also the diffraction pattern allows the determination of the crystallographic features.<sup>(24–27)</sup> In the same instrument, it is easily possible to obtain the electron diffraction (ED) pattern of a small crystal fragment and the image of the same small area without changing the relative orientation of the specimen and the beam. The knowledge of the relative orientation of image and diffraction pattern is essential for a detailed interpretation of the image.

### 2.2.2 Scattering by Atoms

The elastic scattering of electrons by atoms is governed by Coulomb interaction; it contains two contributions of opposite sign. The first is due to the positively charged nucleus, whereas the second one is due to the negatively charged electron cloud. It is described by the atomic scattering factor according to the following equation<sup>(24)</sup>:

$$f_e(\theta) = \frac{me^2\lambda}{2h^2} \left[ \frac{Z - f_x(\theta)}{\sin^2 \theta} \right] \quad (1)$$

where  $Z$  is the atomic number,  $f_x(\theta)$  is the scattering factor for X-rays,  $m$  is the electron mass,  $e$  is the electron charge,  $\lambda$  is the de Broglie wavelength of the electron, and  $h$  is Planck's constant. The interaction with atoms is stronger for electrons than for X-rays. As a result, scattering processes in crystals are best described by dynamic diffraction theory, which takes multiple scattering events into account. However, for many applications, kinematic diffraction theory is a sufficiently good approximation.

### 2.2.3 Geometry of Diffraction by Periodic Structures

The direct lattice of a crystal has node points at positions  $\mathbf{r}_L$  (Equation 2):

$$\mathbf{r}_L = l_1\mathbf{a}_1 + l_2\mathbf{a}_2 + l_3\mathbf{a}_3 \quad (2)$$

where  $\mathbf{a}_1$ ,  $\mathbf{a}_2$ , and  $\mathbf{a}_3$  are the basic lattice vectors and  $l_1$ ,  $l_2$ , and  $l_3$  are integers. Reciprocal space, also called *diffraction space*, consists of reciprocal lattice nodes at positions (Equation 3):

$$\mathbf{b}_H = h_1\mathbf{b}_1 + h_2\mathbf{b}_2 + h_3\mathbf{b}_3 \quad (3)$$

where the  $\mathbf{b}_i$  are the basic vectors of the reciprocal lattice defined by the relations  $\mathbf{a}_i\mathbf{b}_j = \delta_{ij}$  and  $\mathbf{H} = (h_1, h_2, h_3)$  are integers called *Miller indices*. The interplanar spacing of lattice planes with Miller indices  $\mathbf{H}$  is  $d_H = 1/|\mathbf{b}_H|$ .

**2.2.3.1 Bragg's Law** The condition for diffraction to occur can be expressed either in direct space by Bragg's law or in reciprocal space by Ewald's condition. Bragg's law (Figure 3a)<sup>(28)</sup>; Equation 4):

$$2d_H \sin \theta_H = n\lambda \quad (4)$$

( $n$  = integer) states that a strongly diffracted beam will form whenever the incident beam with wavelength  $\lambda$  encloses a Bragg angle  $\theta_H$  with the set of lattice planes with Miller indices  $\mathbf{H}$ . It expresses the condition that the path difference  $\Delta$  between beams 'reflected' by successive lattice planes with spacing  $d_H$  should be an integral number  $n$  of electron wavelengths  $\lambda$ . In ED, because of the small wavelength of the electrons, Bragg angles  $\theta_n$  are only a few degrees at most.

**2.2.3.2 Ewald Construction** The Ewald condition (Figure 3b) for strong diffraction by the set of planes with indices  $\mathbf{H}$  can be formulated as Equation (5):

$$\mathbf{k}_g = \mathbf{k}_0 + \mathbf{g} \quad (5)$$

where  $\mathbf{g} = \mathbf{b}_H$ ,  $\mathbf{k}_g$  is the wavevector of the scattered wave and  $\mathbf{k}_0$  that of the incident wave and  $\mathbf{g}$  is the

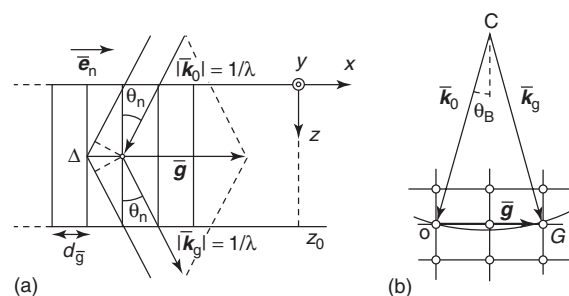


**Figure 3** Illustration of the diffraction conditions. (a) Bragg's law. The diffracting planes with interplanar spacing  $d_g$  are perpendicular to the foil plane. Bragg's law follows from the requirement that the path difference  $\Delta = n\lambda$ . The diffraction vector is  $\mathbf{g}$ ; the Bragg angle  $\theta_n$  is of order  $n$ . (b) Ewald construction ( $\bar{k}$ , wavevector of incident beam;  $\bar{k}_g$ , wavevector of diffracted beam; and  $\mathbf{g}$ , = diffraction vector);  $\bar{k}_g = \bar{k}_0 + \bar{g}$ .

diffraction vector. The physical content of the Ewald condition is the same as that of Bragg's law since  $|\mathbf{k}_g| = |\mathbf{k}_0| = 1/\lambda$  and  $d_H = 1/|\mathbf{b}_H|$ . The Ewald condition expresses the conservation, on scattering, of energy and linear momentum of the incident electrons. It leads to a simple geometric construction of the scattered beam direction. Consider a sphere with radius  $1/\lambda$  and with its center C in  $-\mathbf{k}_0$  with respect to the origin O of the reciprocal lattice (Figure 3b). Diffraction will occur when the sphere touches a reciprocal lattice node. The wavevector of the scattered wave  $\mathbf{k}_g$  is then obtained by joining the center of Ewald's sphere C with the excited reciprocal lattice node.

**2.2.3.3 Thin Foil Effects** The specimens used in TEM have to be thin (of the order of 100 nm). The actual useful thickness depends on the accelerating voltage of the electrons as well as on the material. For thin specimens, the diffraction conditions are relaxed (Figure 4a and b). Even if the Ewald condition is not exactly satisfied, diffraction occurs. In terms of reciprocal space, the nodes become 'rods' (relrods) having a weight profile (Figure 5a) and they are perpendicular to the specimen plane. If Ewald's sphere intersects these 'relrods,' diffraction occurs, the amplitude being proportional to

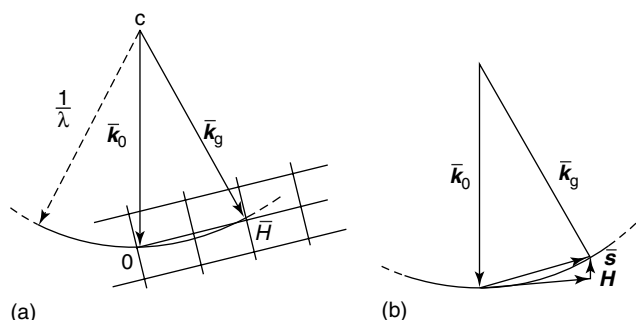


**Figure 4** Diffraction condition in thin foil. (a) The Ewald condition is exactly fulfilled for the reciprocal lattice node  $\bar{H}$ . (b) The Ewald condition is only approximately satisfied; the node  $\bar{H}$  is missed by the excitation error  $\bar{s}$  along the 'relrod.'

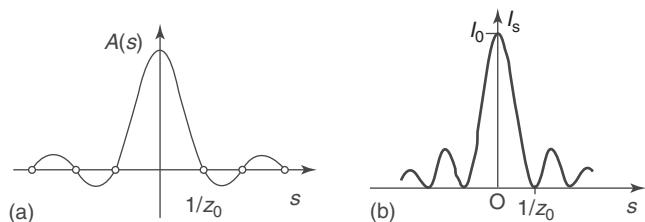


**Figure 5** (a) Weight profile of the amplitude along the 'relrod' as a function of the excitation error  $\bar{s}$  ( $z_0$  = foil thickness). (b) Rocking curve according to the kinematic diffraction theory: scattered intensity  $I_s$  as a function of the excitation error  $\bar{s}$  ( $z_0$  = foil thickness).

the local value of the weight function. The intersection point of Ewald's sphere with the rod is defined by its excitation error value ( $s$  measures the deviation from the exact Bragg condition). The scattered amplitude (or intensity) as a function of  $s$  is called the *rocking curve* (Figure 5b).

The smallness of the Bragg angles in TEM and the small foil thickness together with the occurrence of multiple scattering cause the electrons to travel through the foil along narrow columns parallel to the incident beam (Figure 6). The intensity observed in a point along the exit plane of the specimen depends only on the scattering within the column centered on that point. In an undeformed foil of constant thickness and orientation, the intensity does not depend on the column position; it is uniform. In faulted crystals, the intensity does depend on the position of the column. The intensity distribution along the exit surface then acquires some structure: the image, which is in fact a map of the intensity distribution either in a given diffraction spot (DF image) or in the direct beam (BF image) magnified by the lens system (Figure 7).

#### 2.2.4 Kinematic Diffraction Theory

According to the kinematic theory,<sup>(17,18,24,29)</sup> the scattered intensity  $I(s, z_0)$  for a foil with a thickness  $z_0$  is given by the following equation:

$$I(s, z_0) = F_H^2 \frac{\sin^2 \pi s_H z_0}{(\pi s_H)^2} \quad (6)$$

where  $F_H$  is the structure factor of reflection  $\mathbf{H}$  for which the corresponding excitation error is  $s_H$ . This relation

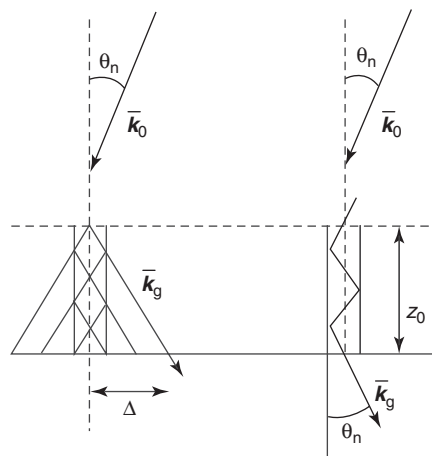


**Figure 6** Propagation of electrons along a column. (Left) According to the kinematic theory, only single scattering events occur. (Right) According to the dynamical theory, multiple scattering events occur.



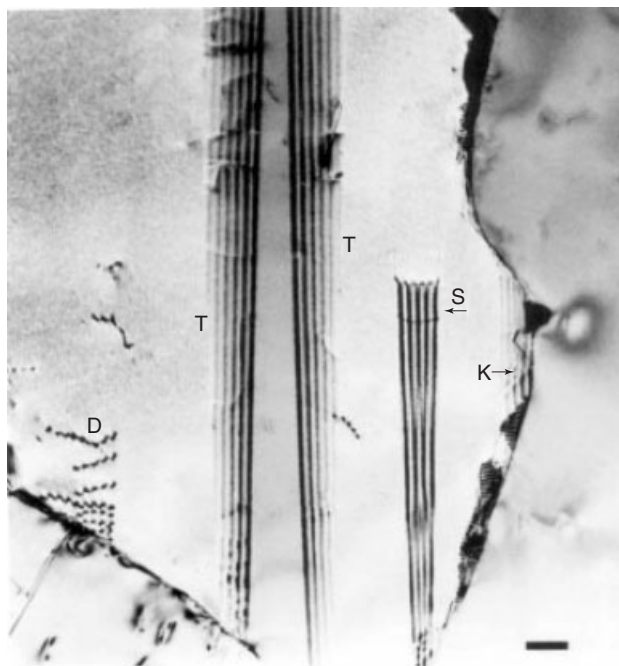


**Figure 7** BF diffraction contrast image of a stainless-steel foil containing various types of defects: dislocations (D), twin boundaries (T), stacking faults (S), and grain boundaries (K).

describes the 'rocking curve' shown in Figure 5(b). The loci corresponding to  $s_H = \text{constant}$  or  $z_0 = \text{constant}$  values corresponding to maxima of  $I(s, z_0)$  are imaged as bright fringes.

The electron wavevector ( $k_0 \sim (1/0.004) \text{ nm}^{-1}$  at 100 kV) is of the order of 50 times larger than the mesh size of the reciprocal lattice ( $\sim 1/0.1 \text{ nm}^{-1}$ ); the Ewald sphere can thus be approximated by a plane perpendicular to  $\mathbf{k}_0$  and the geometry of the ED is thus given by a planar section of reciprocal space. Usually the diffraction pattern will thus exhibit a planar lattice of spots (Figure 8a and b).

By tilting the specimen, an orientation can be achieved, whereby one diffracted beam is much more intense than all others and comparable in intensity to that of the transmitted beam. Such a 'two-beam situation' is desirable for a detailed interpretation of defect images since the diffraction vector producing the image is well defined.

### 2.2.5 Dynamical Theory

In a two-beam situation, the diffracted and the incident beam play equivalent roles in the interior of the crystal, the diffracted beam being incident under the Bragg angle for the same set of planes as the incident beam. The dynamic interplay of incident and diffracted beams leads to a rocking curve for the scattered beam given by the

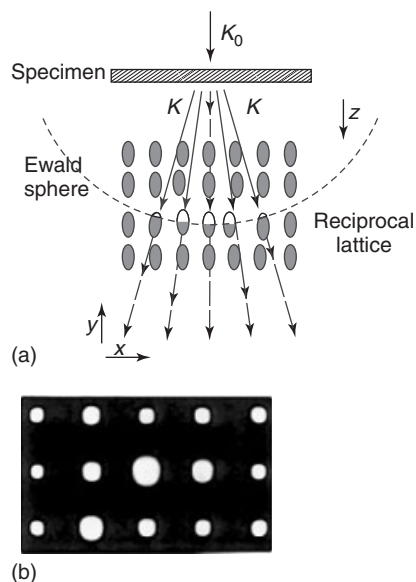


**Figure 8** Formation of the ED pattern. (a) Each diffracted beam corresponds to an intersection point of the 'relrods' in reciprocal space with Ewald's sphere. (b) In fact Ewald's sphere is well approximated by a plane normal to  $\mathbf{k}_0$ .

following equation<sup>(16,24,29)</sup>:

$$I_s = \frac{1}{(\sigma_H t_H)^2} \sin^2 \pi \sigma_H z \quad (7)$$

where  $1/\sigma_H = t_H/(1 + S_H^2 t_H^2)^{1/2}$ ,  $t_H$  being the 'extinction distance,' which is inversely related to the structure factor  $F_H$ ; it is a measure for the strength of the reflection  $\mathbf{H}$ ; a long  $t_H$  corresponds to a weak reflection; and  $z$  is the level behind the entrance face of the foil. The rocking curve of the transmitted beam is then  $I_T = 1 - I_s$ , if absorption is neglected. For  $s_H = 0$ , i.e. for the exact Bragg condition,  $I_s$  and  $I_T$  vary periodically in depth ( $z$ ) with a period  $t_H$ ,  $I_s$  and  $I_T$  being in antiphase. This periodic character is attenuated by absorption (Figure 9).

### 2.2.6 Diffraction Contrast Images

Diffraction contrast images made under two-beam conditions are maps of the intensity distribution in a magnified diffraction spot: either the direct spot (BF image) or the diffracted beam (DF image). They reveal deviations from the perfectly periodic structure of the crystalline foil, but they cannot provide information on the periodic structure.

Diffraction contrast arises because the intensity emerging from a column depends, in general, on its position. In a perfect undeformed foil of constant thickness,  $s$  is constant along a column and the same for all columns. The thickness and the  $s$  value determine the emerging

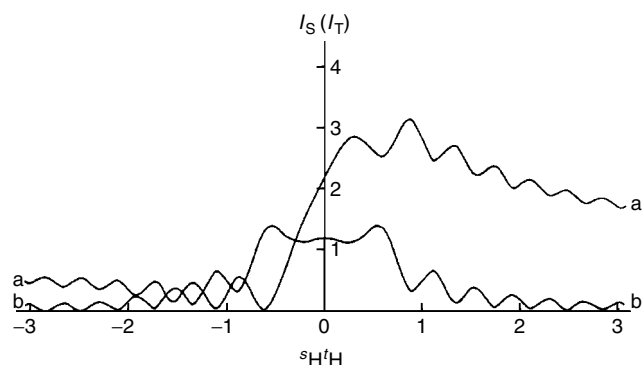


**Figure 9** Rocking curves according to the dynamic diffraction theory taking absorption into account:  $I_T$  (curve a) and  $I_S$  (curve b) as a function of  $s_H t_H$  ( $s_H$ , excitation error of reflection  $\bar{H}$ ;  $t_H$  = extinction distance of reflection  $\bar{H}$ ).

uniform intensity, as given by the rocking curve. If the foil has constant thickness, but is bent, the image will exhibit bright contours corresponding to loci of constant  $s$ , the so-called bend contours. If, on the other hand, the foil is undeformed but has a wedge shape, the image will consist of loci of constant thickness called *thickness* or *wedge fringes*. Often, a foil will exhibit both types of contours simultaneously. They should be distinguished from defect images.

### 2.2.7 Defect Images and Their Interpretation

A dislocation line produces a line of contrast because in the vicinity of the dislocation the lattice planes change in orientation as a consequence of the associated strain field (Figure 10). On one side of the dislocation  $E$  a given set of lattice planes is inclined in one sense, whereas it is inclined in the opposite sense on the other side. On one side ( $E_1$ ) of the dislocation, the Bragg condition may thus be better satisfied than in the perfect part, whereas on the other side ( $E_2$ ) the Bragg condition is then less well satisfied than in the perfect part (Figure 10). Along the columns, on one side of the dislocation more intensity will then be diffracted than in the perfect part; the reverse is true on the other side of the dislocation. Hence, on one side of the dislocation a bright line is produced in a DF image, whereas on the other side a dark line is produced. The image is thus asymmetric and the line image does not coincide exactly with the position of the dislocation line. Diffraction by lattice planes, which are not deformed by the presence of the dislocation, does not produce an image. In general, the lattice defects will be invisible when the diffraction vector is perpendicular to the local displacement vector  $\mathbf{R}$  defining the lattice distortion, i.e.  $\mathbf{g} \cdot \mathbf{R} = 0$ .<sup>(17,18,30)</sup> A network of dislocations in graphite in which one set of dislocation segments remains invisible is shown in Figure 11(a) and (b).

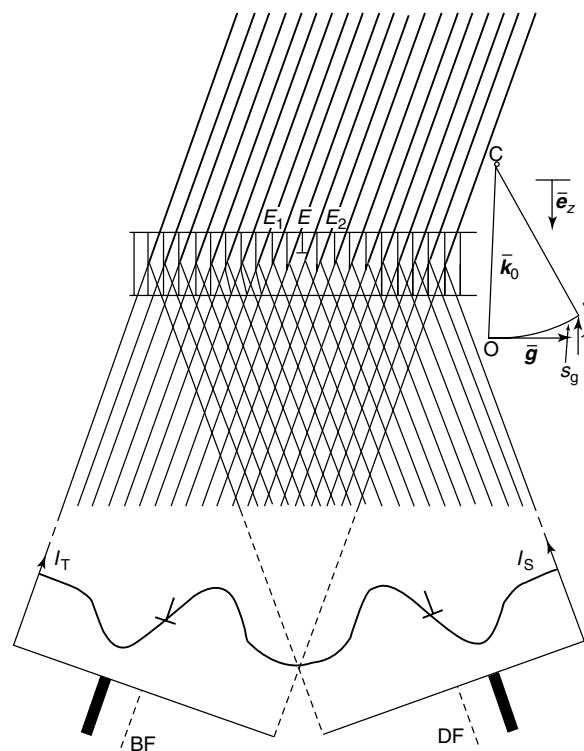


**Figure 10** Formation of diffraction contrast image at an edge dislocation  $E$ . Left (at  $E_1$ ) and right (at  $E_2$ ) of the dislocation the considered lattice planes are inclined in opposite directions: the intensity distributions in the transmitted beam ( $I_T$ ) and in the scattered beam ( $I_S$ ). The resulting image profiles are denoted BF and DF, respectively. The two beam diffraction conditions are also represented in reciprocal space.

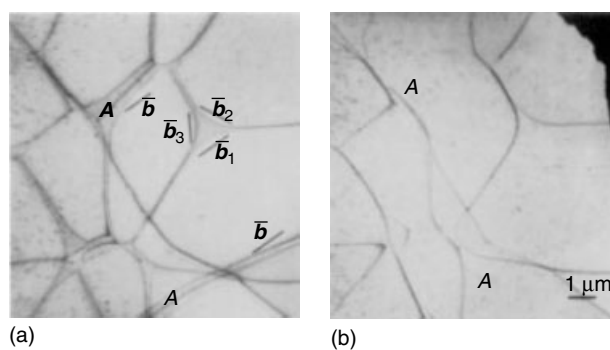


**Figure 11** Network of dislocations in graphite as imaged in diffraction contrast. (a) All dislocations exhibit line contrast and (b) one family of dislocations is out of contrast.

A stacking fault parallel to the foil plane changes the intensity emerging from a column intersecting the fault plane. This intensity therefore depends on the depth at which the fault occurs in the column. This intensity change results from the phase change of the diffracted electron wave caused by the parallel relative shift of the crystal structures above and below the fault plane.

Inclined stacking faults are imaged as fringe patterns in the projected area of the fault plane (Figure 12a and b). The fringes are parallel to the intersection line of the fault plane and the foil surface; they result from the fact that the relative shift of the two crystal parts, separated by the fault plane, occurs at a varying depth along the fault plane. The periodicity of the fringes is equal to the 'extinction distance.'

### 2.2.8 Lattice Fringes

Instead of providing an image by selecting a single beam, one can select both beams in a two-beam orientation (or more) by means of a large enough aperture. The interference of the beams produces a set of sinusoidal fringes with a spacing  $d_H = 1/g$  equal to the interplanar spacing corresponding to the selected diffraction vector  $g$ , the direction of the fringes being perpendicular to  $g$ . An intuitive, purely geometric model allows one to understand the formation of the lattice fringes. In the foil  $F$  represented in Figure 13(a) and (b), the set of indicated lattice planes with diffraction vector  $g$  has an interplanar spacing of  $d_H = 1/g$ . The incident beam  $I$  satisfies the Bragg condition for diffraction by this set of planes, i.e.  $s = 0$ . The transmitted beam is  $T$  and the Bragg scattered beam is  $S$ ; they are assumed to represent plane waves with wavelength  $\lambda$ , which are

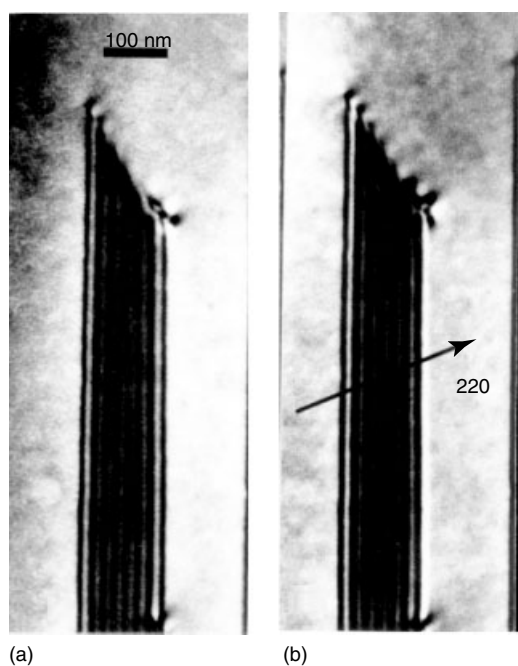


**Figure 12** Diffraction contrast images of an intrinsic stacking fault in stainless steel situated in a plane, which is inclined with respect to the foil plane. (a) BF image: the intensity profile of the fringe patterns is symmetric. (b) DF image: the intensity profile of the fringe patterns is asymmetric.

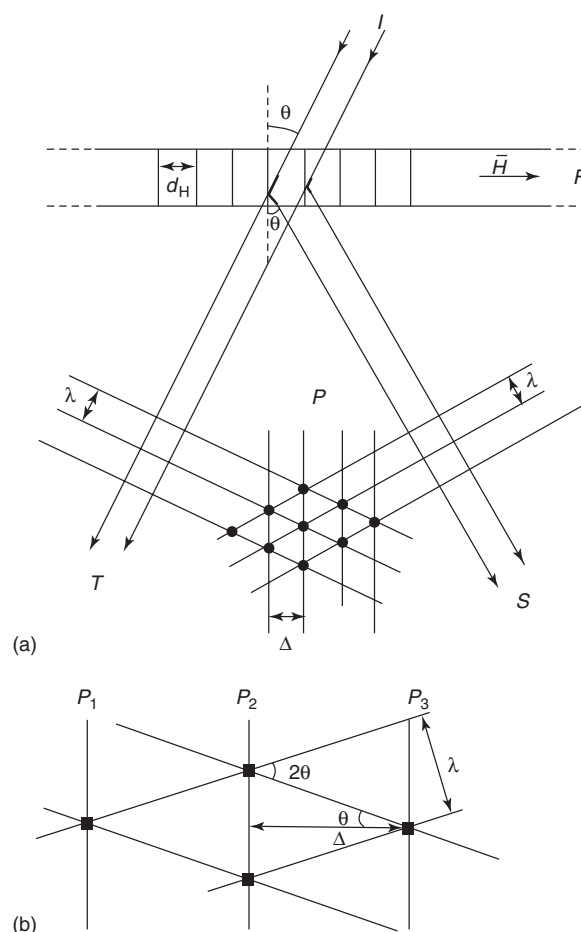


**Figure 13** Geometric model illustrating the formation of two-beam lattice fringes associated with diffracting planes with indices  $H$ . The incident beam satisfies the Bragg condition ( $\theta$ , Bragg angle;  $F$ , foil;  $d_H$ , interplanar spacing; and  $\Delta(d_H)$ , interfringe distance). (b) This is a magnified view of (a).

perpendicular to the corresponding beams; they have maximum elongation along the heavy lines shown in Figure 13(a) and (b). The plane waves interfere behind the foil and intensity maxima will occur along the straight lines where the planes of maximum elongation of  $T$  and  $S$  intersect. The maxima are thus located along the straight lines seen end-on as black dots in Figure 13(a) and (b). As both waves propagate with the same speed, these lines of maxima move along planes  $P_1$ ,  $P_2$ ,  $P_3$  with spacing  $\Delta$ , parallel to the considered lattice planes. Simple geometric considerations show that  $d_H = \Delta$ . The planes of maximum intensity form a stationary pattern and can thus be observed behind the exit plane of the foil. This pattern is an 'image' of the lattice planes. The localization of the fringes (the image) relative to the lattice planes (the object) depends in reality on the diffraction conditions (in particular on  $s$ ), but this has no practical significance in this simple case.

If we include next to the beam with diffraction vector  $\mathbf{g}$  the diffracted beam with diffraction vector  $2\mathbf{g}$ , the resulting interference pattern will also include parallel fringes with a spacing  $1/(2|\mathbf{g}|) = 0.5d$ , i.e. features within the basic period  $d$  are now imaged. As higher order reflections  $n\mathbf{g}$  are included in the interference pattern, the resulting fringe pattern will contain contributions (i.e. Fourier components) with period  $d/n$  consisting of fringes perpendicular to  $n\mathbf{g}$ . The higher the order of the included reflections, the finer is the detail that can be imaged, provided that the resolution of the microscope is able to resolve these fine details. In practice, the lattice resolution of present-day HRTEM is routinely limited to 0.14 nm. For comparison, the point resolution defined as the smallest distance between two points that can be resolved at optimal imaging conditions (the Scherzer defocus) is usually 0.2 nm. With corrections of the higher order aberrations, it could be further improved to about 0.05 nm. In terms of the information limit governed by high spatial frequencies carrying finest structural details that can be transferred from the exit-surface wave to the image intensity, the resolution can be extended from 0.2 to 0.1 nm.<sup>(1,2,31)</sup>

## 2.2.9 High-resolution Images

**2.2.9.1 Fourier Approach** If one selects a two-dimensional array of spots centered on the direct beam, each pair of spots determines a diffraction vector  $\bar{\mathbf{g}}_j$ , which will lead on interference to a set of parallel lattice fringes perpendicular to this vector (Figure 14a and b). According to this model, the image will be formed by the superposition of all Fourier components admitted through the selector aperture. Unfortunately, the limited resolution due to the lens aberrations restricts the useful diffraction vectors  $\bar{\mathbf{g}}_j$  and hence limits the observed details. This is due to the fact that beams enclosing increasing angles with the optical axis become out of phase with the paraxial beams and moreover become damped.

**2.2.9.2 Channeling Approach** An alternative intuitive model emphasizes the fact that one images atom columns parallel to the incident beam rather than single atoms. It considers the propagation (channeling) of electrons in the cylindrically symmetric electrostatic potential well due to the linear strings of atoms forming the columns (Figure 15). On propagating along such a column, the electron wavefunction is centered on the column and oscillates periodically in lateral extent and in intensity with a characteristic depth period  $\Delta_A$  (or  $\Delta_B$ ) (comparable to the extinction distance in dynamic diffraction theory). This period is shorter for the larger the average

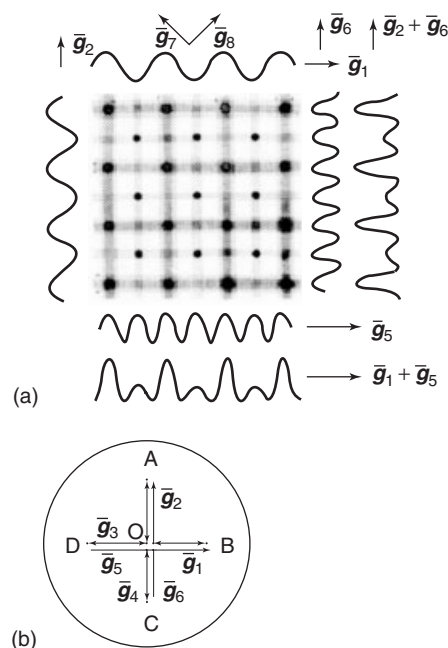


**Figure 14** Formation of two-dimensional high-resolution image by the interference between the direct beam O and four diffracted beams (A–D)(a). Each pair of beams produces a Fourier component with a wavevector given by the line segment connecting the two diffraction spots (b).

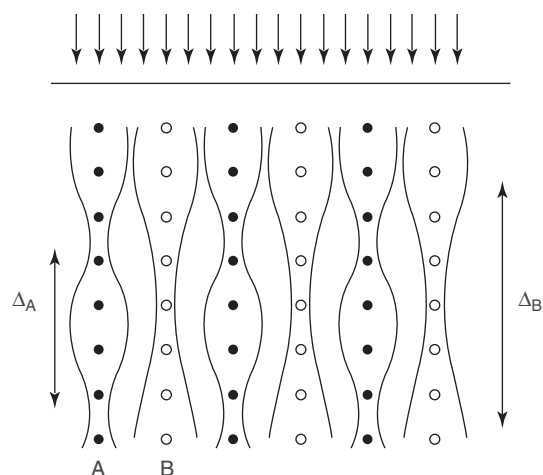


**Figure 15** Formation of 2-D dot patterns as a result of channeling of the electrons along atom columns parallel to the incident beam. The periods  $\Delta_A$  (or  $\Delta_B$ ) of the depth variation of the intensity depend on the atom species A (or B) along the column.

Z value of the atoms in the string; it varies in length in the range from 4 to 20 nm. Depending on the foil thickness, columns may thus exhibit either a maximum or a minimum in brightness at the level of the exit surface. At a given thickness, columns having a different composition will, in general, produce dot images of a different brightness (Figure 16). However, whether a bright or a dark dot



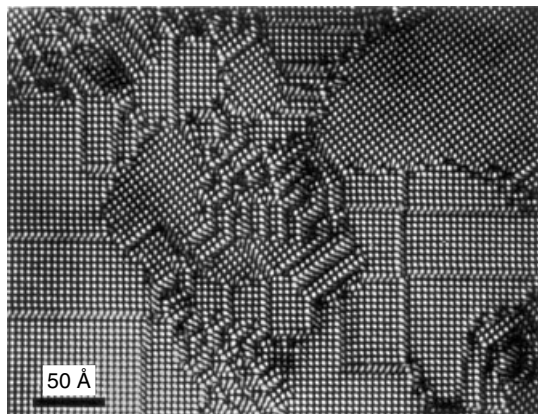


**Figure 16** High-resolution image of the ordered alloy  $\text{Au}_4\text{Mn}$ . The bright dots correspond to the minority columns (consisting of manganese). Antiphase boundaries are observed in two orientation structural variants. (Courtesy of Professor G. Van Tendeloo.)

will be produced in the final image depends not only on the foil thickness but also on the imaging conditions, i.e. whether the microscope is either over- or underfocused. Images are mostly taken under slightly underfocused conditions (which produces the best contrast), optimizing in this way the window in the image transfer function<sup>(29,31)</sup> (Figure 17a and b).

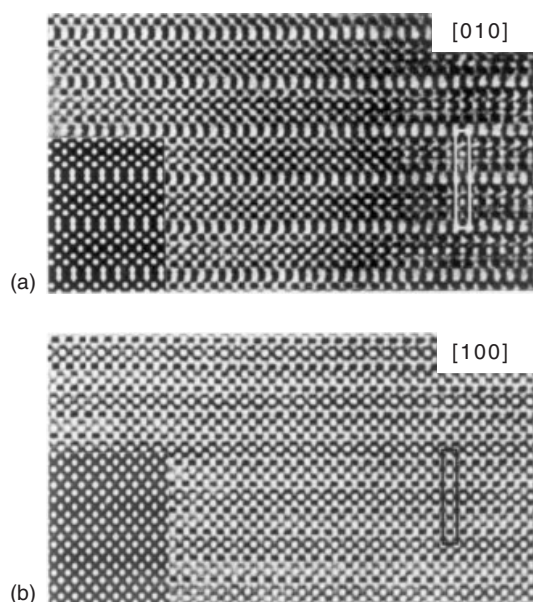


**Figure 17** High-resolution image of the high-temperature superconductor  $\text{Y}_2\text{Ba}_4\text{Cu}_7\text{O}_{15-8}$ . The bright dots reveal the heavy atom columns as projected along two different zones i.e.  $[010]$  (a) and  $[100]$  (b), respectively. Simulated images are reproduced as insets. The projected unit cell is outlined (Courtesy of Professor G. Van Tendeloo). The images were made at optimum defocus. The two images refer to different specimens, with comparable thickness.

## 2.2.10 Image Interpretation

**2.2.10.1 Trial and Error** Digital simulation programs for HRTEM are usually based on the Fourier approach.<sup>(28,32)</sup> They allow one to compute the image of a given structure projected along a given zone axis as a function of the foil thickness and of the imaging conditions (defocus) for a microscope with known characteristics (spherical aberration coefficient, accelerating voltage, and beam convergence; Figure 17a and b).

Identification of a structure or of a defect in a structure proceeds by 'trial and error.' A model is proposed and a matrix of images, varying the two main independent variables (foil thickness and defocus), is computed (Figure 17a and b). These theoretical images are then compared with the observed images at the different thicknesses along a wedge-shaped part of the foil. A solution is considered acceptable when the correspondence between observed and computed images is judged visually to be 'good enough' for all available thicknesses at a constant defocus. This comparison allows one at the same time to estimate the foil thickness and the defocus; these quantities are usually not known *a priori*. Numerical criteria to quantify the 'goodness of fit' have been proposed<sup>(31)</sup> but have seldom been applied as yet. In recent developments, high-resolution images have been used to determine the chemical composition along individual columns in rather special circumstances such as along the interfaces in synthetic layer structures of semiconductors grown by molecular beam epitaxy. The composition profile across an interface can be obtained at an atomic scale. The application of these methods requires a certain amount of *a priori* knowledge concerning the structure.

## 2.2.10.2 Direct Retrieval

'Direct retrieval' methods have been developed, which use as the input a series of images taken at closely spaced defocus values (focus variation method).<sup>(28,29)</sup> Knowing the microscope parameters describing the transfer function and its inverse, the projected wavefunction at the exit plane of the foil can be reconstructed. From this, the projected structure (the object) can be retrieved using an analytical formulation of the channeling model. Knowing the projected structure along more than one zone axis allows one to reconstruct the three-dimensional structure. Less *a priori* knowledge is required than for the methods based on 'trial and error.'

## 2.2.11 High-resolution Defect Images

From high-resolution images with well-resolved atom columns, the presence of translation interfaces, such

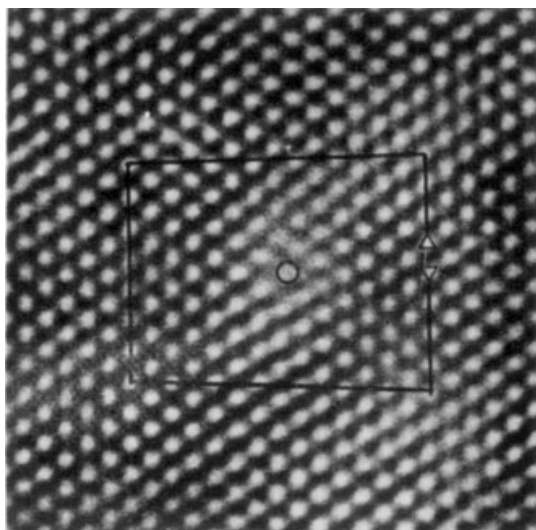


**Figure 18** Core configuration of an edge dislocation in germanium as revealed by HRTEM. A Burgers circuit surrounds the dislocation.

as stacking faults and out-of-phase boundaries, can be deduced directly from the relative shift of the column configurations in the two crystal parts. Only the component of the displacement vector perpendicular to the incident beam direction is obtained in this way. Since the lattice of the structure is represented directly by the dot configuration, the orientation domain microstructure and its interfaces, for instance twins, can also be imaged directly. The core configuration of dislocation lines parallel to the viewing direction can be imaged directly (Figure 18).

#### 2.2.12 Selected-area and Nanobeam Electron Diffraction

ED methods (SAED, CBED, and NBD) are a useful complement to X-ray diffraction, especially when the material is available only as small microcrystals. Then, only powder diffractometry can be applied when using X-rays. However, even fine powders usually contain single crystals of a sufficient size to produce a single-crystal ED pattern, and hence to allow the approximate (but unambiguous) determination of the lattice parameters. These approximate lattice parameters then in turn allow unambiguous indexing of the powder diffraction pattern and subsequently make possible a precise lattice parameter measurement. In addition, SAED patterns often exhibit weak reflections due to superstructures, which are not visible in X-ray powder diffraction.<sup>(17,18,24,28)</sup>

The spatial geometry of diffuse scattering can be reconstructed more easily from SAED patterns than from X-ray diffraction patterns since ED patterns are planar

sections of reciprocal space, which is not the case for X-rays.

In NBD, a nanometer-sized probe with reduced convergence angles (0.1–1 mrad) is directed to the sample, producing diffraction patterns with sharp spots similar to those of conventional SAED. As an advantage, the sample can remain aligned along a chosen zone axis with no need to be tilted off the axis to avoid dynamic interactions as in CBED.

#### 2.2.13 Convergent-beam Electron Diffraction

In most commercial microscopes, it is possible to produce a 'stationary' convergent incident beam rather than a parallel beam by means of the condenser lens system. The electron beams are then incident along directions either within a cone of revolution or confined to a conical surface (hollow cone method), with a semiapex angle within the range 2–10 mrad. The apex of the cone is mostly situated close to the sample plane. The CBED pattern now consists of circular disks of which the size is proportional to the semiapex angle; they are centered on the positions of the Bragg spots that would be produced if the incident beams were parallel to the cone axis. If the semiapex angle is small enough, these disks do not overlap. However, if the semiapex angle exceeds the Bragg angle of the lowest order reflections, these disks overlap and interference occurs between the electron waves in the overlap parts of adjacent disks. For a perfectly flat foil of constant thickness, the intensity distribution within well-separated disks images in a sense the rocking curve associated with the corresponding Bragg spot. The interference between different, partly overlapping disks gives rise to complex contrast, which nevertheless still reflect the symmetry along the zone axis and are representative of the point group and of the space group of the crystalline sample, provided that the selected area is free from defects. A major application of CBED is the determination of crystal symmetry and of the strains in crystals, but defects can also be characterized using DF images and local strain patterns can be revealed. From intensity oscillations in the rocking curve obtained from DF images in a known disk, the foil thickness can be deduced with good accuracy.<sup>(17,18,24,28)</sup>

#### 2.2.14 Scanning Transmission Electron Microscopic Images

The commonly used stationary beam imaging modes (CTEM and HRTEM), being based on interference and diffraction, rely strongly on coherently scattered electrons. However, simultaneously with the coherent scattering, incoherently scattered electrons are also produced by thermal diffuse scattering and in particular by Rutherford scattering. In the STEM, these incoherently scattered



electrons can be used to image atom columns, provided that the proper electron optics are available.<sup>(33–35)</sup> A fine electron probe is obtained by focusing the incident convergent electron beam in the sample and scanning over the foil. Thereby, forward-scattered electrons, i.e. the electrons scattered mainly on axis and forming BF STEM images (<10 mrad) and the ones scattered through small angles and forming Annular Dark Field (ADF) STEM images (between 10 and 50 mrad), respectively, are registered using retractable semiconductor detectors. In addition, a significant fraction of the incoherently scattered electrons emerging from the sample at relatively large scattering angles (>50 mrad off axis) is captured in an annular aperture and detected in a HAADF or Z-contrast mode.

In the case of incoherent imaging conditions, the contrast transfer function is a monotonically decreasing function of the spatial frequency, whereas under coherent imaging conditions it is a rapidly oscillating function. This has important consequences. In the coherent case, the brightness of a dot imaging a given atom column may change from bright to dark and vice versa as a function of defocus. In contrast, in the incoherent case, the relative brightness of a dot remains consistently the same, independent of defocus, i.e. there is no contrast reversal. Moreover, the dot brightness increases monotonically with increasing average *Z* value of the atoms in the column ( $\sim Z^2$ ) as a consequence of the contribution of the Rutherford scattering to the incoherently scattered electrons. Incoherent Z-contrast images can therefore be interpreted on an intuitive basis even for relatively large thickness. It can be shown that structure retrieval is in principle possible and simpler than in the case of coherent imaging.<sup>(28)</sup> The Z-contrast STEM method is, therefore, well suited to the study of geometric defects in crystals.

### 2.2.15 Diffractive (Lensless) Imaging

For a long time, CTEM was constrained by the relatively poor lenses used to form the image. In diffractive imaging, an inverse computation using scattered diffraction intensity data potentially can replace image-forming optics, thus eliminating lens aberrations. This could realize a substantial improvement in resolution (at least by a factor of five over that for the lens) limited by the electron wavelength. A form of diffractive imaging, called *electron ptychography*, has demonstrated that it is possible to recover the complex exit wave in modulus and phase at atomic resolution over an unlimited field of view using low-energy (30 keV) electrons.<sup>(36)</sup>

## 2.3 Inelastic Scattering Processes

Part of the electron kinetic energy is converted in the course of inelastic scattering due to the following atom–electron excitations<sup>(17,18)</sup>:

1. Phonon excitations in solids ( $0.002 \text{ eV} \leq E \leq 0.1 \text{ eV}$ ) normally superimposed with the beam energy spreading.
2. Volume and surface plasmon losses ( $0 \text{ eV} \leq E \leq 50 \text{ eV}$ ) due to longitudinal oscillations of the plasma of valence and/or conduction electrons. The plasmon energy loss,  $E_p$ , is expressed according to the following equation:

$$E_p = \hbar\omega_p = \hbar \left[ \frac{ne^2}{(\epsilon_0 m)} \right]^{1/2} \quad (8)$$

where  $\omega_p = [ne^2/(\epsilon_0 m)]^{1/2}$  is the plasma resonance frequency,  $n$  is the electron density,  $e$  is the electron charge,  $\epsilon_0$  is the permittivity of vacuum, and  $m$  is the electron mass. The low-loss region may also contain losses from the excitations of intra- and interband transitions and of Cerenkov radiation, sometimes overlapped by low-energy ionization edges of outer shells.

3. Quasi-free single-electron excitations (Compton scattering) due to an electron–electron collision, when the transferred energy is larger than the binding energy of excited electrons.
4. Inner-shell ionizations of electrons to a free state or to the continuum beyond the Fermi level resulting in the appearance of an elemental edge at  $E = E_I$  followed by an intensity decrease in a long tail for  $E > E_I$ . The edge profiles (particularly for L- and M-edges) may often exhibit delayed maxima and narrow ‘white’ lines. An energy-loss near-edge structure (ELNES), which is dependent on the local bonding and coordination of atoms, can be detected up to 50–60 eV beyond the ionization edge. An extended energy-loss fine structure (EXELFS) covering several hundred electron-volts beyond the edge may be observed owing to interference between the outgoing spherical ejected electron wave and reflected electron waves backscattered from neighboring atoms, thus giving information about interatomic distances.

## 2.4 Auger Electrons

AE emerge from a solid sample as a consequence of nonradiative rearrangement of the electrons in atoms in which a core hole has been created by the exciting radiation. For an Auger transition involving, for instance, the *j*, *k*, and *l* levels, an electron leaves the solid with a

certain kinetic energy, the atom being left behind in a doubly ionized state (Equation 9)<sup>(37,38)</sup>:

$$E_{\text{kin}}(jkl; X) = E_b(j) - E_b(k) - E_b(l) - F(kl; X) + R_c \quad (9)$$

where  $X$  is the multiplet state resulting from the coupling of the two holes  $k$  and  $l$  in the final state;  $E_b(j)$ ,  $E_b(k)$ , and  $E_b(l)$  are corresponding ground-state one-electron binding energies, which take into account initial chemical shifts and one-hole relaxation phenomena;  $F$  is the two-electron term; and  $R_c$  is a supplementary cross-relaxation energy containing both an atomic and extra-atomic contribution.

Since the primary energy of the exciting electrons in AES is normally in the range 3–10 keV, only K-shell core holes of the light elements can be created, giving rise to the K-series Auger lines. For medium and heavy elements, one excites the L- and M-series Auger lines. The observed AE kinetic energies are usually situated in the range 0–2 keV, limiting the information depth. Electrons must escape from the sample surface without suffering inelastic collisions to be identified, and therefore the escape depth is limited only to a few atomic layers. Depending on the chemical environment of the ionized atom, shifts in the positions of AE peaks are observed. The shape of an AE line also strongly depends on the chemical environment. Both effects are important for chemical composition imaging.

## 2.5 X-rays

The X-ray emission spectra, shown in Figure 19(a–d) for a high-temperature superconductor  $\text{YBa}_2\text{Cu}_3\text{O}_{7-x}$  ceramic, consist of a background (continuum X-rays, bremsstrahlung), which extends up to the energy of the incident beam, together with superimposed discrete characteristic lines of Cu (Cu K- and L-series), Y (Y K- and L-series), Ba (Ba L-series), and O (O K-series). Wavelength-dispersive X-ray spectra (b–d) clearly demonstrate much better resolution than energy-dispersive X-ray spectrum (a). The relationship between the energy of characteristic X-ray emission lines and the atomic number of the element of interest is described by Moseley's law (Equation 10):

$$E = A(Z - 1)^2 \quad (10)$$

where  $A$  is constant within the K-, L-, and M-series and  $Z$  is the target atomic number. When an inner shell electron is ejected from the atom, the latter becomes ionized and goes to a higher energy state. An electron from one of the outer levels must fill the hole vacancy formed in this way. Electron transitions are regulated by the selection rule in which  $\Delta n \neq 1$ ,  $|\Delta l| = 1$ ,  $|\Delta j| = 0$ , where  $n$ ,  $l$ , and  $j$  denote principal quantum number, azimuthal quantum number, and inner quantum number, respectively. An X-ray quantum can be emitted with a discrete energy corresponding to the difference in energy between the levels involved. Major X-ray emission

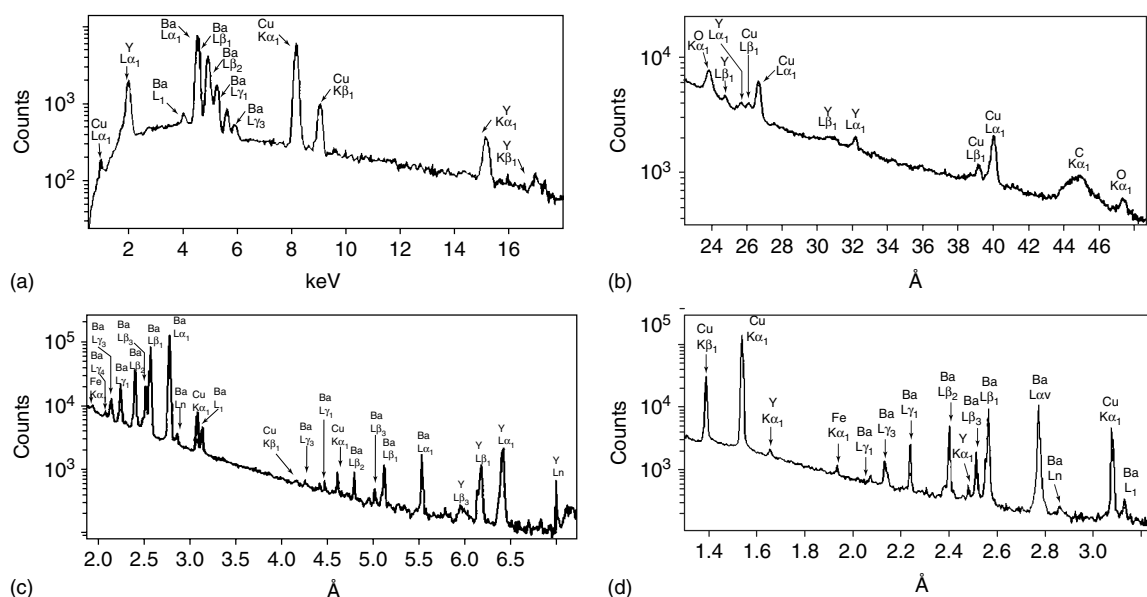


**Figure 19** X-ray emission spectra of a high-temperature superconductor  $\text{YBa}_2\text{Cu}_3\text{O}_{7-x}$  ceramic recorded at accelerating voltage of 25 kV by EDS ((a) 1 nA probe current) and WDS ((b–d), 200 nA probe current). (b) Lead stearate crystal (STE); (c) pentaerythrite (PET) crystal; (d) LiF crystal. The peak of C K $\alpha$  at 4.47 nm (0.277 keV) in spectrum (b) belongs to a carbon conductive coating deposited on the specimen surface. X-ray spectra (c) and (d) exhibit also the presence of traces of Fe (Fe K $\alpha$  at 0.194 nm (6.398 keV) and Pt (Pt L $\alpha$  at 0.131 nm (9.441 keV)), probably from crucible material.



using soft X-ray emission. However, soft X-rays may be produced not only owing to electron transitions involving inner orbitals of the atoms but also as a result of transitions associated with outer orbitals containing valence electrons. The overlap of the valence energy states leads to a decrease in X-ray intensity from ionized atoms. Moreover, since the inner levels are relatively discrete compared with the valence band transitions associated with outer orbitals, the low-energy X-ray lines sensitively reflect the energy states of valence electrons. Chemical bonding effects in the soft X-ray emission spectra are usually more pronounced in insulators than in conductors because the binding energies of valence electrons increase from metallic, through covalent, to ionic bonding. At the same time, the energy of the soft X-ray emission correspondingly decreases. Line shifts and change of shape due to the chemical bonding may be observed in the  $K\alpha$  series from the light elements ( $Z < 10$ ), where the L-shells involved in K–L transitions are incomplete, and also in the L-series from transition metals and their compounds ( $21 < Z < 28$ ). Analysis of the fine structure of soft X-ray spectra recorded with the appropriate resolution can give not only the elemental composition of an object under study but also important information on electronic structure and bonding.<sup>(22)</sup> Application of low-energy X-rays to layered specimens enables one to obtain a reduced depth of ionization. It also permits the elimination of most of the secondary X-ray fluorescence emission that occurs when lines of higher energy are employed, particularly for the EPXMA of multiphase specimens. However, quantitative analysis in this case may be complicated by a number of problems such as contamination, coating, background subtraction, and line interference.

Bremsstrahlung is produced as a consequence of the slowing of electrons in the Coulomb field of atomic nuclei. The continuous X-rays form a background over an energy range  $0 \leq E \leq eU$  extending up to an energy corresponding to the conversion of the entire energy of an incident electron into a radiation photon in a single interaction. The energy distribution of bremsstrahlung may be expressed by Kramers' equation (Equation 13)<sup>(9)</sup>:

$$N(E)dE = bZ \frac{E_0 - E}{E} dE \quad (13)$$

where  $N(E) dE$  is the number of photons within the energy interval  $E$  and  $E + dE$ ,  $b = 2 \times 10^{-9}$  photons  $s^{-1} eV^{-1} electron^{-1}$  is Kramers' constant, and  $E_0 = eU$  is the incident electron energy in electron volts, where  $e$  is the electron charge and  $U$  is the electrostatic potential. The angular distribution of the X-ray continuum is anisotropic and forward peaked. The bremsstrahlung intensity also contributes to the background below the

characteristic X-ray peaks, thereby decreasing the peak-to-background ratio; the latter can be improved with increasing energy of the incident electron beam. The bremsstrahlung can be used to calibrate the film thickness.

## 2.6 Cathodoluminescence

Electron bombardment of semiconductors results in the generation of electron–hole pairs, leading to the CL emission of photons in the ultraviolet, visible, and IR regions. The photons are emitted as a result of electronic transitions between the conduction and valence bands and levels lying in the bandgap, which are ascribed to the crystal structure, chemical composition, doping, and impurities.<sup>(39)</sup> Various defects, dopants, and surface and external perturbations (temperature, electric field, and stress) of the analyzed specimen drastically affect the CL signal. The CL wavelength strongly correlates with the electronic structures, while the CL intensity is a measure of the crystal perfection: it is attenuated when the band structure is perturbed.

## 2.7 Overview of Instrumentation

Hybrid S/TEM, analytical SEM, and EPXMA instruments and specially designed AE microanalyzers equipped with corresponding analytical facilities to detect X-rays, inelastically scattered electrons and/or AE are the most important electron-optical instruments for the analytical and structural investigation of the number of bulk and thin samples. Table 1 lists basic data characterizing state-of-the-art modern EM techniques.

### 2.7.1 Analytical Transmission Electron Microscopes and Nanoscopes

A remarkable capability of STEM is the formation of very small electron probes less than 0.1–1 nm in diameter by means of a field-emission gun (FEG) and a three-stage condenser–lens system. This enables the instrument to operate in the STEM mode with a resolution determined by the electron probe diameter and sample thickness. The main advantage of equipping a TEM system with a STEM attachment and especially with a FEG source is the possibility of producing a very small-electron probe, with which X-ray analysis can be performed on extremely small areas, while switching to operation in the scanning observation modes allows the probe to be conveniently situated on points of interest for analysis.

X-ray generation in thin foils is confined to the small volume excited by the electron probe only slightly broadened by multiple scattering. Better spatial

**Table 1** Basic characteristics of EM methods<sup>(1,2,6,9,16–18,20,22,23,30,33–44,64,65)</sup>

Methods	Signals <sup>a</sup>	Types of contrast	Resolution (nm) (magnification)	Information obtained <sup>a</sup>	Information depth (nm)	Element range	Detection limit (at. % (accuracy, %))
HRTEM	TE/DE	Phase	0.05–0.5 (point) 0.06–0.4 (lattice) ( $\times 20$ – $2 \times 10^7$ )	Structural (lattice imaging), elemental (binary systems)	1–100	–	0.1 (10)
CTEM	TE/DE	Amplitude (diffraction)	0.3–0.5 (point)	Structural (BF, DF imaging)	–	–	–
SAED, CBED	DE	–	–	Structural (point and ring nano- and microdiffraction patterns)	–	–	–
NBD	Z-contrast	–	–	Structural (DF images)	–	–	–
STEM	TE, DE	Diffraction	0.047–0.5 (point-to-point)	Structural (BF, DF images)	–	–	–
	TE + DE	Phase	( $\times 300$ – $10^7$ )	Structural (lattice images)	–	–	–
	DE, TE + DE	Topography, Atomic number	0.1–1 ( $\times 10$ – $10^6$ )	Structural (surface topography images)	–	–	–
	SE	–	0.15–1	Elemental	5–50 $t$ (film)	$\Delta Z < 0.1$	2–3 (10)
SAED/STEM	DE	–	1000	Structural (point, ring diffraction patterns)	–	–	–
CBED/STEM	DE	–	5	Structural (microdiffraction patterns)	–	–	–
(FE)SEM	SE	Topography, atomic number, orientation	0.4–4 (edge-to-edge) ( $\times 10$ – $10^6$ )	Structural (surface topography images)	5–50	–	–
	BSE	Atomic number	1.5–10 ( $\times 10$ – $10^4$ )	Elemental (composition images)	100	$\Delta Z < 0.1$	–
	BSE	'compo,' topography 'topo,' orientation	–	Structural (surface topography images)	–	–	–
	Diffraction	–	–	Structural (electron BS diffraction (Kikuchi) patterns, EBSD)	–	–	–
	Atomic number, orientation	–	–	Elemental (composition images)	1000	–	–
WDS	SC	–	3–100	Structural	–	–	–
	X-ray photons	–	1000 (bulk)	Elemental (spot spectra, profiles, mapping)	1000 (bulk)	3–92	0.01 (2–6)
EDS	X-ray photons	–	1000 (bulk) 0.6–1 (film)	Elemental (spot spectra, profiles, mapping)	1000 (bulk)	4–92	0.1 (2–6)
EFTM/EELS	ELE with $0 < E < 2$ keV	–	1–10	Elemental (spot spectra, 2-D-spectral profiles, mapping)	$t$ (film)	(1) 3–92	1–5 (10–20)
	Chemical (ELNES, EXELFS)	–	–	Structural (ESI images, diffraction patterns)	–	–	–
EH	TE + DE	–	–	3-D Structural, elemental	–	–	–
ET	TE + DE TEM, STEM ELE	–	0.5 $\pm$ 0.1 $\times$ 0.5 $\pm$ 0.1 $\times$ 0.7 $\pm$ 0.2 nm <sup>3</sup>	Surface	–	–	–
	X-ray photons	–	8–300	Elemental (spot spectra, mapping)	1	3–92	0.1 (10)
AES/SAM	SE, AE	–	30–500	Chemical (spectra)	–	–	–
CL, SEM	UV/VIS, IR photons, $0 < h\nu < 1 - 3$ eV	–	–	Chemical (spectra)	–	–	–
	Structural (spectroscopic images)	–	–	–	–	–	–

<sup>a</sup> ELE, electrons with loss of energy; ESI, electron spectroscopic imaging; and UV/VIS, ultraviolet/visible.

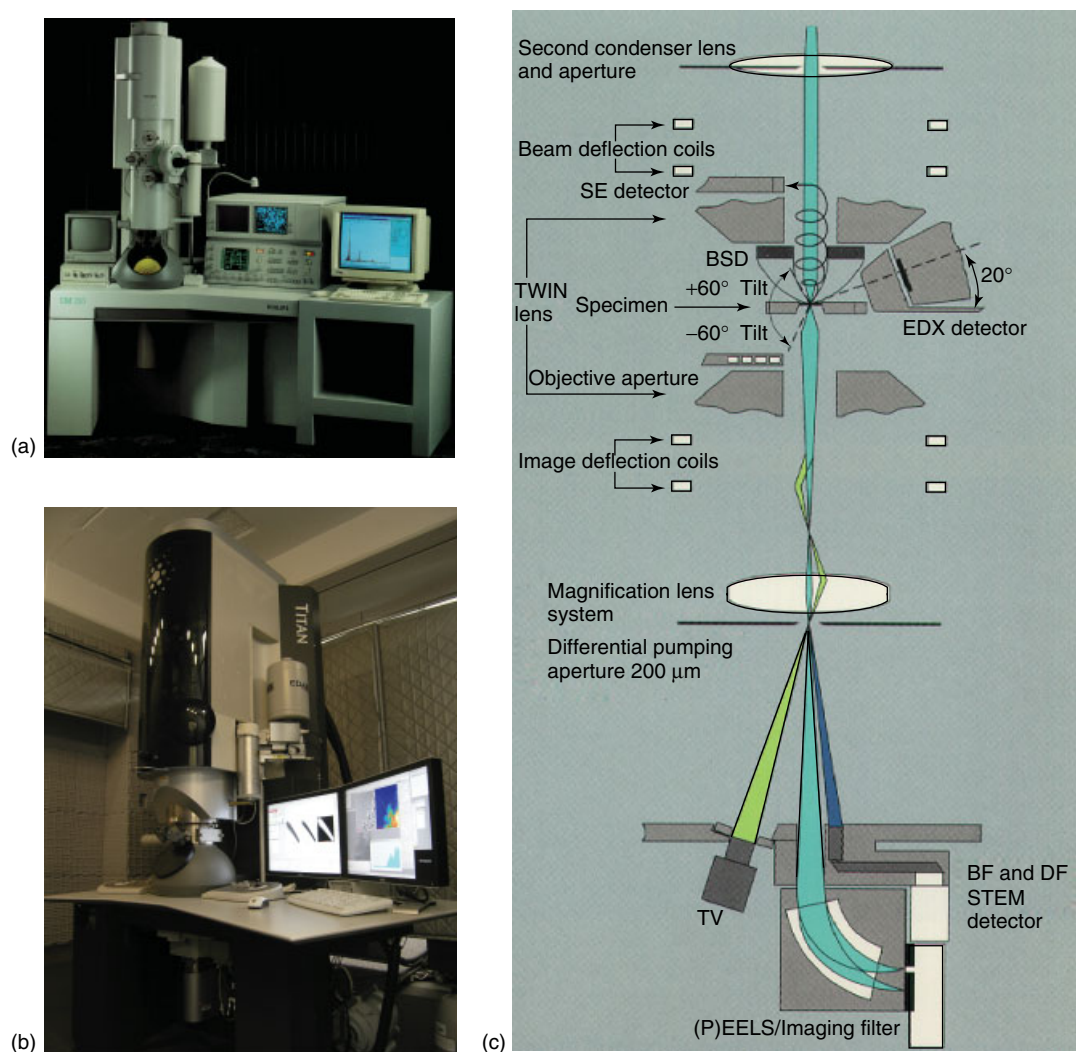


**Figure 22** (a, b) General views and (c) column schematic diagram of electron optics of an analytical S/TEM system showing evolution in its design, (a) Philips CM 200, circa 1997 and (b) FEI Titan 80–300, circa 2009. On the left in (a) are the high-resolution TV monitor and the electron optical column with side-entry airlock, windowless EDS X-ray detector, cold finger, and imaging filter attached at the bottom. On the right are the scanning observation attachment, control panel, and X-ray EDS system. On the left to right in (b) are the shielded electron optical column with the high-brightness Schottky FEG, 6-lens illuminating system with an extra condenser for flexibility, symmetric S-TWIN objective lens, computerized 5-axis stage, biprism for holography, side-entry airlock, HAADF STEM and EDS X-ray detectors, cold finger, and high-resolution multifunctional flat monitor. (Courtesy of Dr M. Otten, FEI, former Philips Electron Optics.)

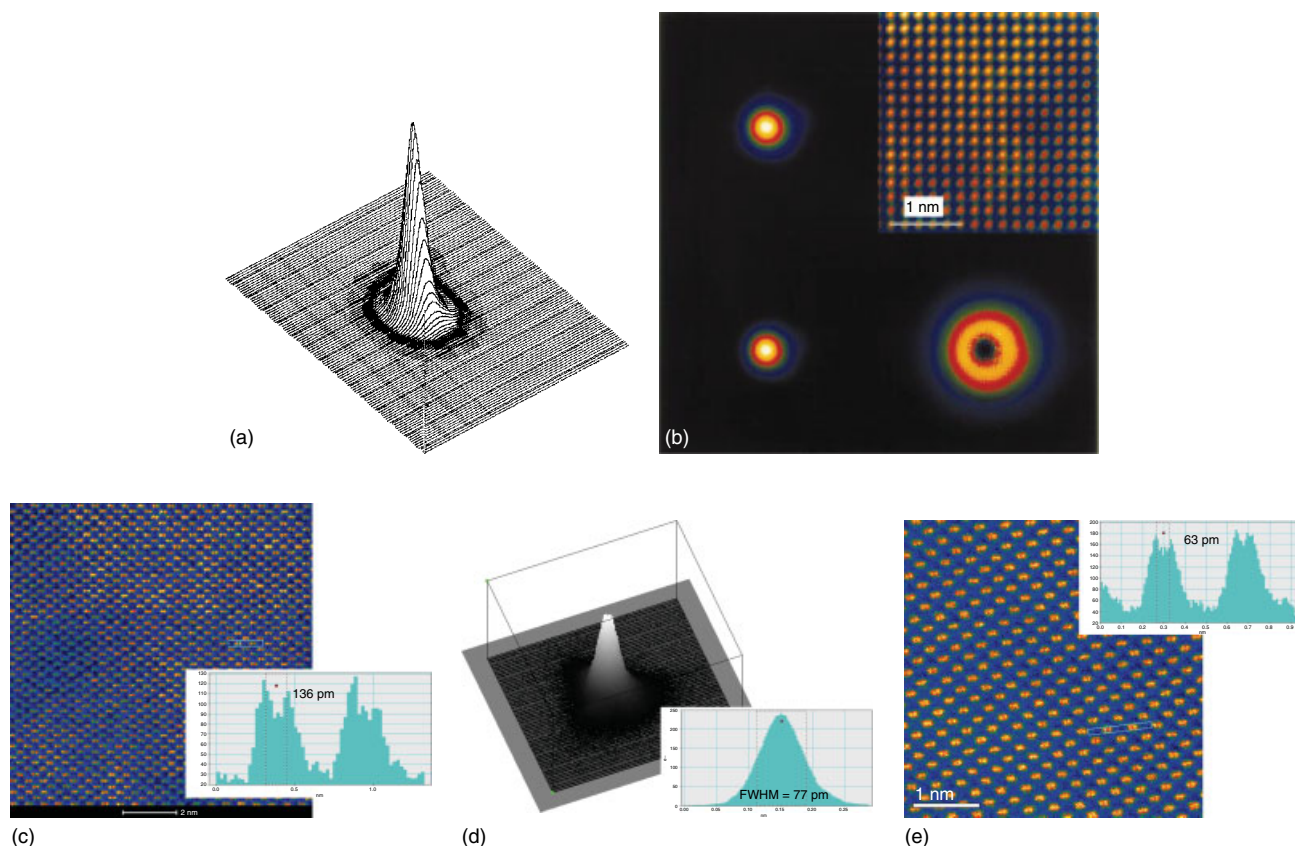
resolution is therefore obtainable for precipitates, or for segregation effects at crystal interfaces, than in an X-ray microanalyzer with bulk specimens, where the spatial resolution is limited to 100–1000 nm by the diameter of the electron interaction volume.

Figure 22(a) and (b) shows evolution in the design of analytical S/TEM systems during the last decade.<sup>(1,2)</sup> Normally such an instrument involves a FEG, a probe-forming condenser–lens system, an objective lens, and an X-ray detection system (EDS), often together with a PEEL spectrometer or imaging filter such as Gatan imaging filter (GIF). Electron probes of 0.07–0.5 nm in

diameter can be formed (Figure 23a and b), the spherical aberration of the lens being the limiting factor in this case. An advantage of STEM instruments is that the contrast can be enhanced by collecting several signals and displaying differences and/or ratios of these by analog or digital processing. Single atoms of heavy elements on an appropriate thin substrate can be imaged with a wide-angle ADF semiconductor detector (Z-contrast) with a higher contrast than in BF- or DF-CTEM modes.<sup>(33–35,41)</sup>

X-ray microanalysis in the STEM mode has a significant advantage over the classical EPXMA in that the lateral resolution can be improved by reducing the





**Figure 23** (a) Three-dimensional view of a 0.4 nm (FWHM) electron probe and (b) spot-size measurements at a current of 30 pA using a slow-scan CCD camera, Philips CM 200. (b) Top left: original image. Top right: lattice image of gold in [100] orientation recorded and displayed at exactly the same magnification as the image of the spot, showing the 0.2-nm spacing for calibration. Bottom left: original image corrected for the response of the CCD camera (beam spreading in scintillator), reducing the apparent spot size by 0.05–0.1 nm. Bottom right: difference between top left and bottom left, showing that the original image is wider (yellow–white ring) and has an extended tail (in blue to black) due to the CCD. (c) High-resolution HAADF STEM image of a silicon specimen acquired on the FEI Titan 80–300 with a probe of about 0.13 nm. The image shows corresponding 0.136 nm dumbbell spacing of Si <110>. (d) Three-dimensional view of a 77 pm (FWHM) monochromatic electron probe, 0.13 eV (FWHM), FEI Titan<sup>3</sup>™ G2 60–300 with probe and image correctors. (e) High resolution HAADF STEM image of GaN (211) acquired on the double-corrected FEI Titan<sup>3</sup>™ G2 60–300 showing 63 pm spacing (Courtesy of Dr M. Otten, S. von Harrach, S. Lazar, M. Bischoff, FEI, former Philips Electron Optics.)

illumination area below 1 nm (nanoanalysis). The fraction of continuous X-ray emission is lower than for bulk samples because of preferential emission in the forward direction. Improvements in X-ray detection have been achieved by increasing the collection angle for a solid-state detector up to 0.3 sr and the X-ray count rate up to 29 000 cps by the use of electrostatic blanking, simultaneous X-ray collection from two detectors with equivalent view points and increase in peak-to-background value for the intrinsic germanium detector up to 6300.<sup>(42)</sup> Determination of the minimum mass fraction (MMF) for Cr measured on a standard thin film showed that an MMF below 0.1–0.05 mass% is possible. With dedicated STEM instruments, ultrasensitive analysis of a single atom and at subnanometer lateral resolution has been realized.<sup>(20,22,23,33–35,42)</sup> Owing to the complementary

nature of the information obtained, the simultaneous high-resolution Z-contrast imaging and EDS/EELS in a dedicated STEM instrument provide a unique tool for insights into a deeper understanding of correlations between the atomic and electronic structure of materials at the atomic scale.

### 2.7.2 Electron Probe X-ray and Auger Microanalyzers and Analytical Scanning Electron Microscopes

The main task of the EPXMA instrument (Figure 24) is to analyze the elemental compositions of flat, polished surfaces at normal electron incidence with a high analytical sensitivity. The ray diagram of such an instrument is similar to that in SEM, but it contains an additional optical microscope to perform fine alignments of the full-focusing WDS spectrometers and to select

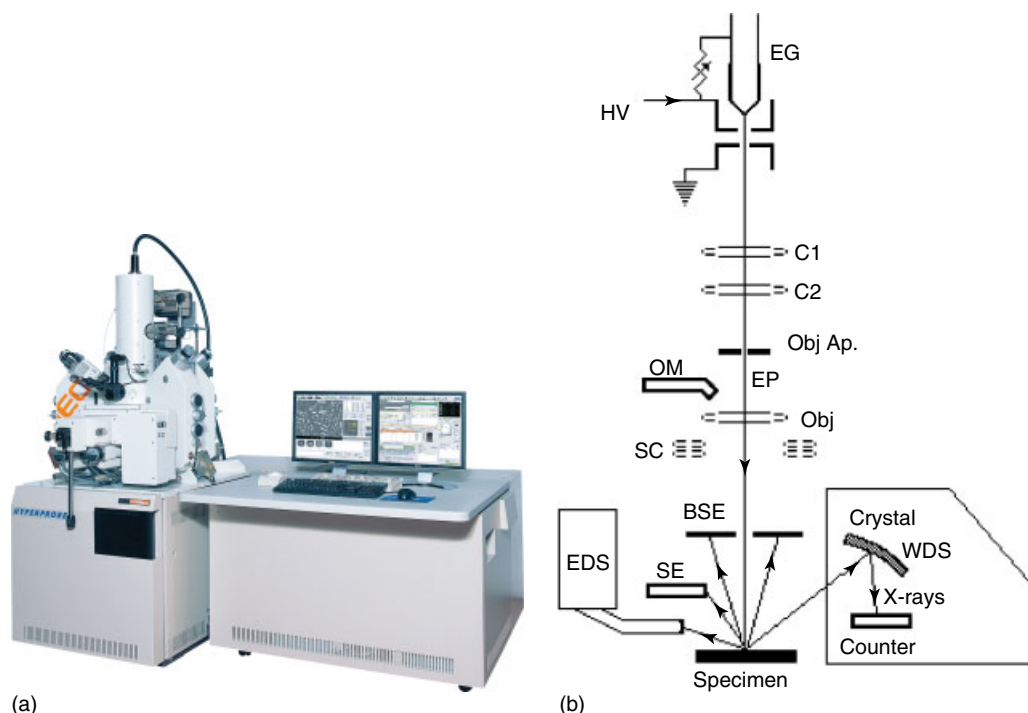


**Figure 24** General view (a) and (b) ray diagram of an electron microprobe/analytical scanning electron microscope. (a) JEOL JXA-8530F HyperProbe, the first FE-Electron Probe Microanalyzer, circa 2010. (Courtesy of Dr V. Robertson and Dr C. Nielsen, JEOL, USA). (b) (FE-) EG, electron gun; HV, high voltage; C1, first condenser lens; C2, second condenser lens; Obj Ap., objective lens aperture; OM, optical microscope; EP, electron probe; Obj, objective lens; SC, scanning coils; BSE, backscattered electron detector; and SE, secondary electron detector.

the specimen points, profiles, and/or areas to be analyzed. It contains up to five WDS X-ray crystal spectrometers, which can record different characteristic X-ray wavelengths, and often also an EDS instrument, which can detect X-rays in a wide energy range. An electron probe (from about 6 nm to 1  $\mu\text{m}$  in diameter is governed by the acceptable probe current range from  $10^{-12}$  to  $10^{-5}$  A) is produced by a one-, two-, or three-stage demagnification of the smallest cross-section of the electron beam after acceleration. Images and spectra are displayed on a monitor with multiple windows combining the different signals, i.e. SE, BSE, SC, CL, or X-rays that result from the electron–specimen interactions.

The combined WDS/EDS microanalyzer controls its EDS and WDS components with the aid of a powerful computer multitasking workstation and presents X-ray data acquired by both spectrometers and images as a unified analysis result. Combination of WDS and EDS systems can increase the number of simultaneously detectable elements to 13 (five with WDS and eight with EDS). TV display allows the optical microscope image and one of the SEM modes (SE or BSE images) to be observed simultaneously.

A microanalyzer may also be equipped with a cylindrical mirror AE spectrometer.<sup>(43)</sup> This, however,

needs an ultrahigh vacuum. AE microanalyzers, in which the 10-keV electron gun is incorporated in the inner cylinder of the spectrometer, can work in the scanning mode so that an image of the surface is formed with SE or an element-distribution map, especially of light elements, is generated using AE (SAM). In the recent generation of AE microanalyzers equipped with a Schottky FEG and a low-aberration condenser lens, in which an electrostatic field and a magnetic field are superposed, one can significantly reduce spot sizes and use beam currents up to 200 nA (Figure 25a).

An electrostatic hemispherical analyzer (HSA) with a multichannel detector optimally designed for Auger analysis provides extreme energy resolution without sacrificing sensitivity (Figure 25b). With the new instruments, high-resolution SEM and SAM imaging are possible together with image and line profile analyses. In addition, depth profile analysis during ion etching is possible using an ion gun for high-speed sputtering and low-energy charge neutralization. New AE microanalyzers also offer the flexibility of optional analysis functions such as EDS and X-ray photoelectron spectroscopy (XPS).

Traditionally, electron probe microanalysis (EPMA) or analytical SEM are operated at an accelerating voltage in the range 15–40 kV when used with EDS and WDS.

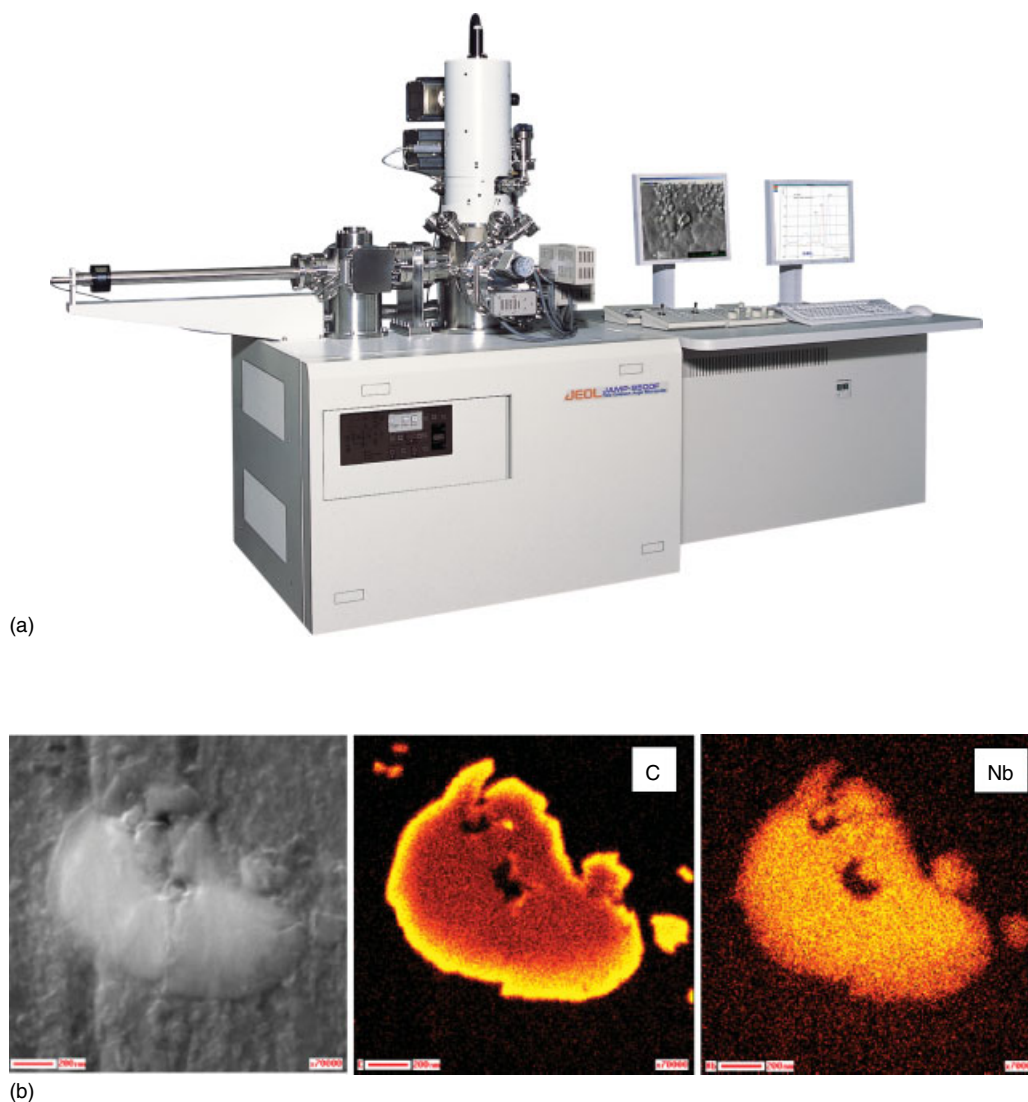


**Figure 25** (a) General view of a JEOL JAMP-9500F FE-Auger Microprobe, circa 2004, and (b) secondary electron image and carbon and niobium Auger maps of NbC particles 400–500 nm in diameter in a stainless steel, showing a carbon-enriched 50-nm-thick layer surrounding NbC particles. (Courtesy of Dr V. Robertson and Dr C. Nielsen, JEOL USA and Dr. K. Tsutsumi, Electron Optics Division, JEOL Ltd.)

These conditions are sufficient to allow excitation of X-ray emission of all relevant elements. However, with the increasing interest in the detection of light elements and the availability of ultrathin window or windowless detectors, the importance of low voltages ( $<1$  kV) is also emphasized. With FEGs that produce sufficient current density even in the low voltage range from 5 to 2 kV, the lateral resolution for X-ray analysis may be significantly improved.<sup>(44)</sup> As a consequence, thin layers and small particles can be examined by SEM without interference of the bulk support. Low-voltage field emission scanning electron microscopy (LV-FESEM) offers both high spatial resolution and reduced X-ray generation depth.<sup>(64,65)</sup>

Using the scanning beam facilities of the EPMA or SEM instrument, panchromatic CL imaging, CL emission spectroscopy, and micro-Raman spectroscopy may be easily combined with EDS/WDS and X-ray mapping and electron imaging to perform comprehensive spatially resolved microanalysis of point defects in minerals and ceramics and dopant impurities in semiconductors.<sup>(64–66)</sup> Variable-pressure scanning electron microscopy (VP-SEM) and environmental scanning electron microscopy (ESEM), respectively, are the natural extensions of conventional SEM that can operate from high vacuum up to a pressure level that can maintain fully wet specimens. This is useful for microanalytical studies of

uncoated insulating specimens by EDS, CL, and micro-Raman spectroscopy in conjunction with morphological characterization by SE/BSE imaging.<sup>(45)</sup> Combining electron beam capabilities with focused ion beam (FIB), dual-beam FIB/SEM/EDS has become the powerful tool both for machining, fabrication, and 3D structural and compositional characterization<sup>(64,65,67)</sup> (also see Table 4).

### 2.7.3 Integrated Analytical Electron Microscopy Systems

AEM and EPXMA use electron excitation for carrying out chemical analysis. Digital image processing of multiple detector signals (TE/DE/SE/BSE(EBSD)/SC/AE/X-ray/CL and/or light image) and computer control with the aid of a powerful multitasking workstation, conversion and storage of data, on-line processing for immediate interpretation of images and spectra, and feedback to the instrument significantly increase the capability of modern analyzers.

The new generation of aberration corrected 60–300 kV FEG-AEMs have been commercialized during recent years by several vendors (FEI, JEOL, Nion, Hitachi, and Zeiss), and offer advanced imaging capabilities in CTEM, HRTEM, EFTEM, STEM, and SEM modes and enable to attain the best possible analytical sensitivity, resolution, and versatility for EDS, EELS, SAED, CBED, NBD,

tomography, and holography consistent with state-of-the-art materials research. The high-end aberration-corrected S/TEM and high-performance-dedicated STEM systems comprise a Schottky or high-brightness cold FEG with gun lens and monochromator, a probe and/or image C<sub>s</sub>-correctors coupled with a triple condenser, objective, and quadruple projector. The gun brightness is sufficient to provide the nominal image resolution at or better than 0.1 nm in TEM mode (point-to-point) and/or in high-resolution (HA)ADF-STEM mode. The FEG-AEMs may be controlled either directly or using the personal computer and a mouse-directed interactive graphical user interface, thus providing telepresence microscopy remote control and operation over the Internet.<sup>(2,20,22)</sup>

## 3 ANALYTICAL METHODS

### 3.1 X-ray Emission Spectrometry in the Transmission Electron Microscopy, Scanning Transmission Electron Microscopy, and Scanning Electron Microscopy Modes

There are two main spectroscopic systems that can be coupled to SEM, STEM, or TEM instruments to record X-ray quanta, i.e. WDS and EDS. Their principal features are compared in Table 2.

**Table 2** Comparison of WDS and EDS<sup>(9,20,22,23,30,42,46,51,64–71)</sup>

Items compared	WDS	EDS		
Basic method	Wavelength dispersion by diffracting crystals	Energy dispersion by solid-state Si(Li) or Ge X-ray detector	Si drift X-ray detector (SDD)	Superconducting transition-edge X-ray microcalorimeter
Available elemental range	<sup>3</sup> Li– <sup>92</sup> U	<sup>4</sup> Be– <sup>92</sup> U	<sup>4</sup> Be– <sup>92</sup> U	<sup>4</sup> Be– <sup>92</sup> U
Resolution (Mn K $\alpha$ , FWHM) (eV)	2–20	100–150	150–230	3–10
Probe current range (A)	10 <sup>–9</sup> –10 <sup>–5</sup>	10 <sup>–12</sup> –10 <sup>–9</sup>	10 <sup>–10</sup> –10 <sup>–8</sup>	4 × 10 <sup>–11</sup> –2.5 × 10 <sup>–7</sup>
Detection limit (ppm)	50–100	1500–2000	1500–2000	–
Number of simultaneously analyzed elements	1	Up to 25	Up to 25	Up to 25
Maximum X-ray acquisition rate	10 <sup>2</sup> –10 <sup>5</sup>	10 <sup>3</sup> –3.10 <sup>4</sup>	~10 <sup>6</sup>	1.5 × 10 <sup>2</sup> –2.5 × 10 <sup>3</sup>
Solid angle (msr)	8–25	150–300	900–3140	0.01–4
Collection efficiency (%)	<0.2	<2.0		0.005–2
Typical active area of detector (mm <sup>2</sup> )	Not applicable	10–30	30–80	
Time to acquire full spectrum (min)	30	1	1	
Artifacts	High-order lines	Escape peaks, pulse pileup, sum peaks, Si K (Ge K (L)) internal fluorescence	Escape peaks, pulse pileup, sum peaks, Si K (Ge K (L)) internal fluorescence	–

**Table 3** Elemental range of analyzing crystals<sup>(9,20,22,23,70,71)</sup>

Crystal (abbrev.)	2d (nm)	Wavelength range (nm)	Detectable elements (Th)
STE	10.04	2.22–9.3	<sup>5</sup> B– <sup>8</sup> O, <sup>16</sup> S– <sup>23</sup> V
TAP	2.576	0.569–2.38	<sup>8</sup> O– <sup>15</sup> P, <sup>24</sup> Cr– <sup>41</sup> Nb <sup>46</sup> Pd____ <sup>79</sup> Au
PET	0.8742	0.193–0.81	<sup>13</sup> Al– <sup>25</sup> Mn, <sup>36</sup> Kr <sup>65</sup> Tb, <sup>70</sup> Yb____ <sup>92</sup> U
LIF	0.4027	0.0889–0.373	<sup>19</sup> K____ <sup>37</sup> Rb <sup>48</sup> Cd____ <sup>92</sup> U
MYR	8.0	1.77–7.41	<sup>5</sup> B– <sup>9</sup> F, <sup>17</sup> Cl– <sup>25</sup> Mn
LDE1 <sup>a</sup>	6.0		<sup>6</sup> C– <sup>9</sup> F
LDE2 <sup>a</sup> , LDEN	10.0		<sup>5</sup> B– <sup>8</sup> O
LDEB <sup>a</sup>	14.5		<sup>4</sup> Be– <sup>5</sup> B
VLS grating <sup>b</sup>		38.738–6.198	<sup>3</sup> Li____ <sup>12</sup> Mg

STE: lead stearate; TAP: thallium acid phthalate; PET: pentaerythrite; LIF: lithium fluoride; MYR: lead myristate (Langmuir–Blodgett fatty acid pseudocrystal); LDE1: layered dispersion element 1; LDE2: layered dispersion element 2; LDEB: layered dispersion element B; and LDEN: layered dispersion element N.

<sup>a</sup>Superlattice crystals.

<sup>b</sup>Laminar-type VLS grating.

WDS uses the Bragg reflection of X-ray emission dispersed from the lattice planes of an analyzing curved crystal ( $2d \sin \theta = n\lambda$ ). Crystals with different lattice spacings (0.4–10 nm) (Table 3) are used usually to analyze the whole wavelength range from below 0.1 nm (U L $\alpha$   $\approx$  0.091 nm) to above 11 nm (Be  $\alpha$   $\approx$  11.3 nm). Laminar-type varied-line-spaced (VLS) grating for ultrasoft X-ray spectroscopy enabled to extend the lower limit of detection energy to 32 eV using a spectrometer composed of the grating and a multichannel plate detector attached to a TEM. At the low-energy end of this spectrometer, Li K $\alpha$  emission spectra with a peak at 54.1 eV were obtained with an energy resolution of 0.2 eV.<sup>(70,71)</sup>

The spot irradiated by the electron beam on the specimen acts as an entrance slit, while the analyzing crystal and the exit slit are mounted on a Rowland circle. The lattice planes of the crystal are bent so that their radius is  $2R$  and the crystal surface is ground to a radius  $R$ . Focusing allows a better separation of narrow characteristic lines and a solid angle of collection of nearly  $10^{-3}$ – $10^{-2}$  sr.

Behind the slit, X-ray photons are recorded by a proportional counter and their energy is converted to a voltage pulse. The detection efficiency of the Bragg reflection and the proportional counter is about 10–30%.<sup>(9,17,18)</sup> The number of electron–ion pairs generated in the counter is proportional to the quantum energy  $E = h\nu$ . The pulses are further amplified, discriminated in a single-channel analyzer, and counted by a scaler. The pulse intensity per second is indicated by a ratemeter. Counters with ultrathin Mylar windows are available to detect the weak K $\alpha$  lines of light elements ( $4 \leq Z \leq 11$ ) more efficiently than with EDS. WDS systems offer better energy (wavelength) resolution and higher count rates (above 50 000 cps) than conventional Si(Li) EDS

systems but require a higher beam current (Figure 19a–d and Table 2). For scanning across a chosen spectral region, the counter and the analyzing crystal should be moved by a pivot mechanism. Usually X-ray microanalyzers are equipped with several WDS instruments, which enable different wavelengths to be recorded simultaneously.

With EDS, a solid-state detector is positioned before the dispersing system to collect the distribution of X-ray emission in a wide energy range (0.1–40 keV for a conventional Si(Li) detector and even up to 80 keV for an intrinsic Ge detector). Dispersion of the signal detected then takes place by electronic processing using pulse-height amplification, pileup rejection of possible coincidence of pulses, and sorting by a multichannel analyzer, which relates the measured pulse height to the energy of the incoming photon. The entire assembly of a conventional detector, including a field-effect transistor preamplifier, is cryo-cooled under vacuum at near liquid nitrogen temperature to minimize thermally induced signals. The detection efficiency of an Si(Li) detector is nearly 100% in the range 3–15 keV. The decrease at low energies is caused by the absorption of the X-rays in the thin Be window, separating the high-vacuum microscope column from the detector. Both windowless and ultrathin window detectors can record K $\alpha$  quanta from light elements down to Be. At energies higher than 15 keV, the decrease in the efficiency is caused by the increasing probability of transmission through the sensitive layer of the detector without photoionization.

A 42.5 mm<sup>2</sup> silicon drift EDS detector (SDD) in transmission geometry interfaced to an FESEM<sup>(68)</sup> and the combination of multiple SDD detectors attached to an FEG-S/TEM<sup>(69)</sup> have been optimized to achieve a continuously variable solid angle of 3.14 sr and 0.9



sr, respectively, compared to 0.1–0.3 sr of previous designs in S/TEMs. These new designs result in a large increase in count rates for a given beam current, thus providing opportunities for high-speed sub-nanometer resolution X-ray spectral imaging. Recent developments in EDS detector fabrication have led to significant characteristic improvements in low-energy performance and achieving ultimate sensitivity limits. Modern EDS detectors can be exploited without permanent cooling; they can be kept at room temperature without any degradation in performance. Newly designed models are electrically cooled with an incorporated Peltier device or need no cooling at all, although still at the cost of some decrease in the resolution. SDDs are rapidly replacing Si(Li) detectors for EDS microanalysis in SEM, providing the higher count rate capability and subsequently the throughput improvement (Table 2). The microcalorimeter EDS detector with an energy resolution of 3–10 eV allows detection not only of closely spaced X-ray peaks but also of chemical shifts, although the acceptable counting rate is still rather low.<sup>(46)</sup>

Unlike WDS, where the irradiated point has to be carefully adjusted on the Rowland circle, an EDS instrument does not need any mechanical adjustment, and therefore can be used much more effectively for profile or area analyses by scanning over large and/or rough specimens. Since an EDS system occupies a smaller space than a WDS system, it is commonly used in analytical SEM and S/TEM setups. A further advantage of EDS is that most of the characteristic X-ray lines can be recorded simultaneously in a short time. For this reason, X-ray microanalyzers that work with WDS are often also equipped with an EDS instrument under the control of the same computer, thus forming an integrated WDS/EDS system to provide more rapid and accurate assessments of the specimen elemental composition. This includes the following capabilities: (i) simultaneous data acquisition of up to 13 elements with the combination of five WDS and one EDS instruments, which is more than twice the number measurable with WDS alone; (ii) microanalysis of light elements and microvolume elements with a high beam current of  $10^{-9}$ – $10^{-5}$  A (WDS) and of heavy elements of a few percent under the same conditions as for SEM observations at a current of  $10^{-12}$ – $10^{-9}$  A (EDS) for increasing the total analysis efficiency; and (iii) preliminary evaluation of beam-sensitive samples by EDS.

### 3.2 Cathodoluminescence Spectroscopy in the Scanning Electron Microscopy, Scanning Transmission Electron Microscopy, and Transmission Electron Microscopy Modes

CL is a powerful technique that provides microcharacterization of the optical and electronic properties of

luminescent materials with the detection limit as low as  $10^{14}$  atoms  $\text{cm}^{-3}$  and a spatial resolution down to 10 nm and even less for adsorbed or thin specimens. Owing to the scattering of the beam electrons and the large escape depth of light, the spatial resolution may not reach that of an SE image. CL is a well-established technique in SEM,<sup>(17,18,39)</sup> although the CL signal can, of course, also be collected in an S/TEM system equipped with a detector for the light quanta. An advantage of CL is the possibility of simultaneously imaging crystal defects including depth-resolved information by varying the beam energy and examining their CL nature. Additional information concerning variations in the concentration of dopants acting as luminescence centers and recombination centers is obtainable. The CL intensity is usually low and requires a highly efficient light-collection system with a large solid angle and lateral selection of the irradiated area to avoid the contribution of diffusely scattered electrons.

### 3.3 Energy-filtering Transmission Electron Microscopy and Electron Energy-Loss Spectroscopy

EELS measures the energy distribution of electrons that have been transmitted through a specimen. EFTEM/EELS using an imaging filter or magnetic sector spectrometer offer possibilities to select electrons with a well-defined energy loss (zero-loss, plasmon, and elemental imaging on inner-shell ionization edges) and to record spatially and angularly resolved EEL spectra providing local analyses of plasmon losses and inner-shell excitations with ELNES and EXELFS.<sup>(6)</sup> The transferred energy can be recorded as an energy loss of the incident monochromatic electrons and reduces their kinetic energy to  $E_0 - \Delta E$ . This results from excitations from occupied states below the Fermi level to unoccupied states above it, allowed by selection rules. Indeed, EELS is spectroscopy of excited electron states beyond the Fermi level. An EEL spectrum (Figure 26a and b) is more complicated than an X-ray emission spectrum and contains information from several excitation processes.<sup>(15)</sup>

Always being delocalized to some extent, inelastically scattered electrons considerably reduce the image contrast. Furthermore, the chromatic aberration of the objective lens also reduces the resolution for thicker specimens. The great advantage of energy filtering is that it allows the separation of the contribution of inelastically scattered electrons from that of elastically scattered electrons and selection of inelastically scattered electrons with certain energy losses. With column-incorporated and postcolumn imaging filters, a new era of AEM began. The different operating modes of the EFTEM/EELS instrument are usually combined to switch easily between ESI and electron spectroscopic diffraction (ESD) to different EELS modes. Because electron images and



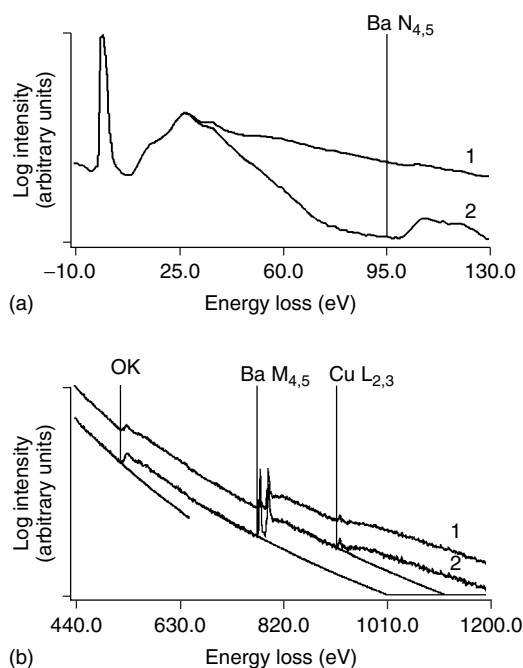


**Figure 26** EEL spectra of a specimen of high-temperature superconductor  $\text{YBa}_2\text{Cu}_3\text{O}_{7-x}$  ceramic: (a) the zero-loss peak and low losses; (b) the inner-shell region. Background assigned by a power-law function is shown. 1, Experimental spectrum, 2, single scattering distribution. Removal of multiple scattering improves the resolution of low-loss features and elemental ionization edges.

diffraction patterns as projections of the reciprocal lattice represent 2-D intensity distributions, selection of energy losses with an appropriate energy window allows a new dimension in EM (spectrum imaging and image-spectrum techniques<sup>(15,16)</sup>).

#### 4 IN SITU ELECTRON MICROSCOPY

In situ EM combines stationary beam and scanning (S/TEM and SEM) imaging, diffraction and spectroscopy modes with physical and chemical processing (e.g. mechanical or (electro) chemical testing, heating/cooling, radiation damage experiments, and gas (vapor)-solid chemical reactions in environmental cells).<sup>(72,73)</sup> These capabilities essentially expand the use of electron beams for studies of dynamic processes and reactions in real time (see Section 9.1 for examples).

The concept of the material processing laboratory in an EM, which allows several high spatial resolution analytical modes to be combined with experiments that are traditionally carried out *ex situ*, is highly attractive for solving a number of problems in strategic R&D areas identified as having the potential to realize significant economic, governmental, and societal impacts.

In situ high-resolution AEM coupled with dual-beam FIB/SEM can be transformed into the advanced nanolab for the material characterization, testing, fabrication, manipulation, and metrology of materials dynamic response to various external variables (Section 9).

The atomic level spatially resolved real-time perspective of nanoscale transformations is crucial for a number of practically important nanomaterials-related applications. In this case, the transformation mechanisms or reaction kinetics can be directly connected to energetics and dynamics of individual elementary steps and related to the structure of the active sites involved.

In high-speed transmission electron microscopy (HSTEM) or dynamic transmission electron microscopy (DTEM), fast dynamic phenomena in materials can be captured with nanosecond time resolution using an electron gun modulated by short laser pulses via an attached disk photocathode.<sup>(74)</sup> The high time resolution of in situ observations by the HSTEM can provide new insights into the phases and morphological evolution (e.g. occurring in solid-state reactions of NiAl reactive multilayer films, during martensitic transformations in nanocrystalline Ti and the catalytic growth of Si nanowires). It is expected that improvements to the electron optics and laser systems will continue to expand the instrument's capabilities, which at present include the ability to capture single-shot images with 15 ns and 10 nm spatiotemporal resolution. Four-dimensional ultrafast electron microscopy (4D UEM) enables by 10 orders of magnitude better resolution than that of conventional EM limited by the video-camera recording rates.<sup>(75)</sup> In ultrafast electron microscopy (UEM), real-space stroboscopic imaging, including 4-D tomography, Fourier-space diffraction and energy-space electron spectroscopy can be obtained with single-electron coherent packets even at higher spatiotemporal resolutions than in HSTEM. The transition to 4-D UEM has the potential to display complex physical, chemical, and biological phenomena of different length and time scale, ranging from atomic motions in structural dynamics (e.g. graphite in 3D space) to irreversible phase transitions and crystallization.

#### 5 SPECIAL MODES (HOLOGRAPHY AND TOMOGRAPHY)

Electron holography (EH) is based on the formation of an interference pattern or 'hologram' in a TEM.<sup>(1,2,17,18)</sup> In contrast to conventional imaging, it provides a method for detecting the phase shift of the electron wave due to magnetic field or electric field. In practice, EH is carried out using an FEG TEM, which has been fitted with a beam splitter (the biprism)<sup>(30)</sup>. For this purpose, the biprism is

placed for EH experiments below the objective lens at the position usually occupied by the selected-area diffraction aperture.

Electron tomography (ET) enables 3-D reconstruction of objects using single- and dual-axis tilting series.<sup>(1,2,17,18)</sup> ET has recently evolved into an important tool to study materials at the nanoscale (for EFTEM tomography, see Section 9.4.2). The quality of a 3-D reconstruction depends on a number of experimental factors (the tilt range, total number of 2-D projection images, and the alignment of the images in the tilt series) and the reconstruction algorithm. BF-TEM and HRTEM were initially the primary imaging methods for 3-D tomography. Acquiring an interpretable 3-D tomogram, however, requires that the projected image intensities vary monotonically with material thickness. This condition is difficult to fulfill in BF-TEM/HRTEM, where image intensities are dominated by diffraction contrast or phase-contrast with the potential for multiple contrast reversals with thickness, making it difficult to distinguish voids from high-density inclusions. In addition, the contrast transfer function of BF-TEM acts as a high-pass filter and information at low spatial frequencies is significantly suppressed, thus leading to an exaggeration of sharp features. On the contrary, ADF-STEM more effectively suppresses phase and diffraction contrast, providing image intensities that vary with the projected mass-thickness of samples up to microns thick for low atomic number materials. ADF-STEM also acts as a low-pass filter, eliminating the edge-enhancing artifacts common in BF/HRTEM. In such a way, ADF-STEM tomography often yields a reliable reconstruction of the underlying specimen with a sub-nanometer 3-D resolution, which is extremely important for its applications.

## 6 DIGITAL IMAGE ANALYSIS

Image analysis converts the information in the electron image into numerical form. In addition to on-line image acquisition, this is usually also off-line or on-line gray-scale processing, discrimination, and binarization followed by quantitative evaluation of features of interest. Processing of data may vary in a wide range from size/shape population distributions, stereological measurements, 3-D tomographic image reconstruction, and specimen restoration to fractal analysis.<sup>(3–6,17,18,30,47)</sup> Advanced statistical algorithms (multivariate statistical analysis, automated feature sizing/chemical typing) allow processing of high volumes of quantitative information from a series of acquisitions. This offers flexible means for various measurements (e.g. sizes/shapes of surface features, classification of the analyzed specimen areas vs

chemical contents of constituents, and phase identification and enhancement of the SNR for SI signals limited by low acquisition rates). The next important application of image analysis (Section 2.2.10) is simulation, and matching of conventional and HRTEM and STEM lattice images and diffraction patterns, particularly by multislice calculations, taking into account the contrast transfer function, astigmatism, and beam tilt correction.<sup>(17,18,30)</sup> Some specific applications of image analysis in EM are considered in Section 9.

## 7 SAMPLE PREPARATION TECHNIQUES

A number of techniques are commonly used for specimen preparation in conventional EM (SEM and TEM) and high-resolution (S)TEM. Sample and standard preparation for analytical SEM, AEM, and AES/SAM includes some additional requirements aimed at providing correct qualitative assignment and further quantification of the data (Table 4).

## 8 QUANTIFICATION

### 8.1 X-ray Microanalysis

To quantify X-ray spectra, the measured intensity of a particular characteristic X-ray line from the bulk specimen should be compared with the same one produced by a reference bulk standard of known composition. The procedure involving the use of bulk pure-element standards for EXPMA of bulk specimens can, in principle, also be adapted for the microanalysis of thin films.<sup>(9,17,18)</sup> Hence, by keeping instrumental settings (probe current, high voltage, detector efficiency, etc.) constant, while the X-ray intensity readings are being taken with dead time corrections related to the spectrometer, one can consider the ratio of the X-ray intensities of the  $i$  line of an element  $a$ ,  $k_a^i$ , measured respectively in the specimen,  $I_{sp}^i$ , and a standard,  $I_{st}^i$  (Equation 14):

$$\frac{I_{sp}^i}{I_{st}^i} = k_a^i \quad (14)$$

where the intensity ratio can be related to the mass concentration,  $c_a$ , of the analyte element as  $k_a^i = f(c_a)$  and  $\sum c_a = 1$ .

An accurate quantitative evaluation can be performed if the  $k_a^i$  ratio is corrected for various effects: the atomic number correction for the differences between the electron scattering and penetration in the sample and the standard; the absorption correction for the difference in

**Table 4** Main material preparation techniques for EM, analytical SEM, AEM, and AES/SAM Studies<sup>(30,37,38,45,67,76,77)</sup>

EM technique	Samples	Standards	Preparation methods	Support
SEM/WDS/EDS	Bulk specimens ( $\geq 1\ \mu\text{m}$ thick) mounted in beam-stable low-viscosity resin	Known compositions (inner and secondary standards) stable under the beam and homogeneous on the submicron/nanometer scale, may be mounted in ordered arrays in resin	Mechanical polishing + conducting coating with a 10–20-nm thick carbon layer (if necessary), FIB	Not necessary
STEM/TEM/WDS/EDS	Thin specimens deposited on thin (lacey, holey) carbon (SiO, SiN) films	Known compositions (inner and secondary standards) stable under the beam and homogeneous down to the nanometer scale with known thickness	(Cryo-)ultramicrotomy, ion thinning, mechanical polishing followed by electrochemical and/or ion thinning + conducting coating with thin carbon layer (if necessary); deposition on thin (holey, lacey) film supports, FIB with a low-kilovolt cleaning and lift-out	Self-supported specimens or ones deposited on thin, stable films (should not contain elements of interest)
EFTEM/EELS	1–1000-nm-thick specimens deposited on thin (lacey, holey) carbon (SiO) films	Accurately known compositions, stable under the beam and homogeneous down to the nanometer scale	(Cryo-)ultramicrotomy, ion thinning, mechanical polishing followed by (electro)chemical and/or ion thinning + conducting coating with thin carbon layer (if necessary); deposition on thin (holey, lacey) films, FIB with a low kilovolt cleaning and lift-out	Self-supported specimens or ones deposited on thin, stable films (should not contain elements of interest)
AES/SAM	Bulk specimens, thin films deposited on bulk substrates	Accurately known bulk and surface compositions, stable under the beam and homogeneous on the nanometer scale	In situ ultrahigh vacuum preparation (scraping, fracture, cleavage); surface cleaning by Ar <sup>+</sup> bombardment, degreasing using detergents followed by rinsing in clean water and ultrasonic bath treatment + careful drying	Not necessary

the absorption of the emitted X-rays as they pass through the sample or standard; and the fluorescence correction for the secondary X-ray fluorescence generated by the X-ray emission in the specimen and in the standard.

### 8.1.1 ZAF Method

The ratio of X-ray intensities emitted from element *a* in the specimen and in the pure standard is given by the

following equation:

$$\frac{I_{\text{sp}}^a}{I_{\text{st}}^a} = \frac{\varphi(\rho z)_{\text{sp}}^a \left[ \int_0^\infty \varphi(\rho z) d\rho z \right]_{\text{sp}}^a f(\chi)_{\text{sp}}^a (1 + \gamma + \beta)_{\text{sp}}^a}{\varphi(\rho z)_{\text{st}}^a \left[ \int_0^\infty \varphi(\rho z) d\rho z \right]_{\text{st}}^a f(\chi)_{\text{st}}^a (1 + \gamma + \beta)_{\text{st}}^a} \quad (15)$$

The first ratio in Equation (15), which corresponds to the ratio of the emission of element *a* from an isolated thin layer of mass thickness  $\rho z$  in the specimen and in the standard, respectively, is proportional to the

number of ionizations produced by the electron beam, i.e. (Equation 16)

$$\frac{\varphi(\rho z)_{\text{sp}}^{\text{a}}}{\varphi(\rho z)_{\text{st}}^{\text{a}}} = \frac{Q\omega(Nc_{\text{a}}/A)d\rho z}{Q\omega(N/A)d\rho z} = c_{\text{a}} \quad (16)$$

where  $Q$  is the ionization cross-section of atoms  $a$ ,  $\omega$  is the X-ray emission yield,  $N$  is Avogadro's number,  $A$  is the atomic weight of  $a$ , and  $c_{\text{a}}$  is the mass concentration of element  $a$  in the specimen. Then one can deduce from Equation (15) that the next three ratios may be used to represent the atomic number, absorption, and fluorescence correction factors,  $k_{\text{Z}}$ ,  $k_{\text{A}}$ , and  $k_{\text{F}}$ , respectively. The corresponding corrections are considered in the ZAF method as independent multiplicative factors of the  $k$  ratios (Equation 17):

$$k_{\text{a}}^{\text{i}} = k_{\text{Z}}k_{\text{A}}k_{\text{F}}c_{\text{a}} \quad (17)$$

The atomic number correction should be applied to the  $k$  ratio to compensate for the difference between the electron retardation and electron backscattering in the specimen and the standard. Because each correction factor is a function of  $c_{\text{a}}$  rather than  $k_{\text{a}}^{\text{i}}$ , iteration procedures (normalization, hyperbolic, or Wegstein methods) should be employed to improve further the precision of the data.<sup>(9)</sup> The  $k_{\text{Z}}$  for element  $a$  can be written as the following equation:

$$k_{\text{Z}}^{\text{a}} = \frac{R_{\text{sp}}^{\text{a}} \int_{E_{\text{c}}}^{E_0} (Q/S)_{\text{sp}}^{\text{a}} dE}{R_{\text{st}}^{\text{a}} \int_{E_{\text{c}}}^{E_0} (Q/S)_{\text{st}}^{\text{a}} dE} \quad (18)$$

where the terms  $R$  and  $S$  refer to the electron backscattering and the electron stopping power, respectively, and  $Q$  is the ionization cross-section. The integral limits are from the incident electron beam energy  $E_0$  to the critical excitation band  $E_{\text{c}}$  for the chosen X-ray line of  $a$ . The electron stopping power  $S = -1/\rho dE/dx$ , defined as the energy lost per unit electron path length in material of density  $\rho$ , may be approximated according to the following equation<sup>(9)</sup>:

$$S = 78\,500 \frac{Z^{\text{a}}}{A^{\text{a}}} \frac{1}{E} \ln \left( \frac{1.166E}{J^{\text{a}}} \right) \quad (19)$$

where  $J = [10.04 + 8.25 \exp(-Z/11.22)]Z$ . The expressions for the ionization cross-section  $Q$  have the general form of the following equation:

$$Q = C \frac{\ln U}{UE_{\text{c}}^2} \quad (20)$$

where  $C$  is a constant and  $U = E_0/E_{\text{c}}$  is the overvoltage.

The electron backscattering factor  $R = (I_{\text{t}} - I_{\text{b}})/I_{\text{t}}$ , defined as the fraction of total generated X-ray intensity excluding loss due to BSE, may be calculated using empirical expressions. In a multielement system, the factor  $R$  for element  $i$  may be derived from the following equation:

$$R_i = \sum_j C_j R_{ij} \quad (21)$$

where  $i$  represents the element being measured and  $j$  denotes the elements in the specimen including  $i$ ;  $R_{ij}$  is the backscatter correction factor for element  $i$  in the presence of element  $j$ . Several tabulations and fitted polynomial expressions are available to estimate values of  $R$  for various elements as a function of  $Z$  and  $U$ .<sup>(50)</sup>

The absorption correction factor  $k_{\text{A}} = f(\chi)_{\text{sp}}^{\text{a}}/f(\chi)_{\text{st}}^{\text{a}}$  reflects the attenuation of the X-ray intensity measured by the detector. The basic formulation for the absorption term  $f(\chi)$  is given by the Philibert–Duncumb–Heinrich equation (Equation 22)<sup>(9)</sup>:

$$\frac{1}{f(\chi)} = \left(1 + \frac{\chi}{\sigma}\right) \left(1 + \frac{h}{1+h}\right) \frac{\chi}{\sigma} \quad (22)$$

where  $\sigma = 4.5 \times 10^5 / (E_0^{1.65} - E_{\text{c}}^{1.65})$  is Lenard's constant and  $h = 1.2A/Z^2$ .

The variable  $h$  is dependent on the composition and must be averaged over the various elements present in multielement specimens according to the following equation:

$$h_i = \sum_j c_j h_j \quad (23)$$

In addition, the mass absorption coefficient  $\mu/\rho$  for the characteristic line of element  $i$  must be the weighted sum over all elements, i.e. (Equation 24)

$$\left(\frac{\mu}{\rho}\right)_i^{\text{sp}} = \sum_j c_j \left(\frac{\mu}{\rho}\right)_i^j \quad (24)$$

The calculation of  $f(\chi)$  from Equation (22) is most accurate for values greater than 0.7.

The characteristic fluorescence correction is necessary when the energy  $E_j$  of the characteristic X-ray line from an element  $j$  is greater than the critical excitation energy  $E_{\text{c},i}$  for an element  $i$  and when the difference  $E_j - E_{\text{c},i} < 0.5$  keV. This may result in excitation of the characteristic emission of element  $i$  by the corresponding characteristic line of element  $j$ . The basic formulation of the characteristic fluorescence correction is given by the

following equation:

$$F_i = \frac{\left(1 + \sum_j I_{i,j}^f/I_i\right)_{\text{sp}}}{\left(1 + \sum_j I_{i,j}^f/I_i\right)_{\text{st}}} \quad (25)$$

where  $I_{i,j}^f/I_i$  is the ratio of the characteristic intensity of element  $i$  excited by fluorescence to the electron-excited intensity. The total correction should be summed over all the elements in the specimen. In practice, when the standard is either a pure element or there is no significant fluorescence of element  $i$  by other elements in the standard, Equation (25) can be simplified to Equation (26):

$$F_i = \left(1 + \sum_j I_{i,j}^f/I_i\right)_{\text{sp}} \quad (26)$$

In addition, the calculation of the continuum fluorescence is relatively complicated, involving integration over the range from  $E_0$  to  $E_c$  for each element in the sample. When  $f(\chi) > 0.95$ ,  $c_i < 0.5$ , and  $z_{\text{sp}} \neq z_{\text{st}}$ , the correction can be as large as 2–4%, and it should be included for highest accuracy.

### 8.1.2 $\phi(\rho z)$ Methods

Quantitative microanalysis can be carried out more suitably by treating the atomic number and absorption factors together rather than as separate entities. The correction by the  $\phi(\rho z)$  procedure is based on the integration of X-ray distributions,  $\phi(\rho z)$  curves; it is attractive for the analysis of low-energy X-ray lines, where  $f(\chi)$  is much less than 0.7 and the accuracy of the ZAF method is low. However, results of the analysis based on the  $\phi(\rho z)$  methods are dependent on the accuracy of description of the experimental  $\phi(\rho z)$  curves (especially in the case of systems with unknown X-ray depth distributions) and/or fitting to the corresponding results of Monte Carlo simulation.<sup>(9)</sup>

For instance, the Packwood–Brown model<sup>(48)</sup> uses a modified surface-centered Gaussian function to describe the shape of  $\phi(\rho z)$  curves. The Gaussian nature of the curve implies some random distribution of electron scattering events. The surface modification should be applied to take into account that the incoming accelerated electrons require some finite distance range before becoming randomized. The general expression for  $\phi(\rho z)$  is given by the following equation:

$$\phi(\rho z) = \gamma \exp[-\alpha^2(\rho z)^2] \left[ 1 - \left( \frac{\gamma - \phi(0)}{\gamma} \right) \exp(-\beta \rho z) \right] \quad (27)$$

The Gaussian is modified by a transient function to model an increase of the X-ray production away from the near-surface region. The coefficient  $\alpha$  relates to the width of the Gaussian and  $\gamma$  relates to the amplitude. The term  $\beta$  in the transient is related to the slope of the curve in the subsurface region: this means the rate at which the focused electron beam is randomized through scattering in the sample. The intercept  $\phi(0)$  is related to the surface ionization potential. The  $\alpha$ ,  $\beta$ , and  $\gamma$  parameters are expressed in terms of several different experimental terms, i.e. elemental composition of the sample, incident electron energy, atomic number, etc.

### 8.1.3 Standardless Analysis

In standardless analysis, the measured standard intensities are substituted with calculated values based on atomic data and empirical adjustments to experimental data. Better quantitative procedures were developed in the last two decades to validate better standardless calculations. In particular, with the K-lines a relative accuracy of 1–5% is reached.<sup>(49)</sup> Some uncertainties exist with the L-lines and especially with the M-lines where atomic data sets are still incomplete or not accurate enough. Further study of the effect of the incompletely filled inner shells is necessary to obtain better atomic data.

The X-ray intensity generated in a bulk sample (standard) for the simpler case of the K-line<sup>(50)</sup> may be expressed by the following equation:

$$I = g \epsilon p \omega f(\chi) \frac{N}{A} R \int_{E_0}^{E_c} \frac{Q}{dE/d\rho s} dE \quad (28)$$

where  $g$  is a normalization factor that depends on the experimental parameters (beam current, acquisition time, solid angle of the detector, etc.),  $\epsilon$  is the detector efficiency,  $p$  is the transition probability,  $\omega$  is the fluorescence yield,  $f(\chi)$  is the absorption correction,  $R$  is the backscatter factor, and  $Q$  is the ionization cross-section given in general form by Equation (20). The additional intensity induced by the secondary X-ray fluorescence is not considered here. When calculating the number of ionizations for the L- and M-shells, both direct ionizations induced by the bombarding electrons and indirect ionizations caused by the nonradiative Coster–Kronig transitions between subshells before the emission of the X-ray line must also be taken into account. The Si(Li) detector efficiency can be given by the following equation:

$$\varepsilon = \left\{ 1 - \exp \left[ - \left( \frac{\mu}{\rho} \right)_{\text{Si}} \rho d_{\text{Si,act}} \right] \exp \left[ - \left( \frac{\mu}{\rho} \right)_{\text{Be}} \rho d_{\text{Be}} \right] \right. \\ \left. \times \exp \left[ - \left( \frac{\mu}{\rho} \right)_{\text{Au}} \rho d_{\text{Au}} \right] \exp \left[ - \left( \frac{\mu}{\rho} \right)_{\text{Si}} \rho d_{\text{Si,dead}} \right] \right\} \quad (29)$$

where Be, Au, Si,act, and Si,dead refer to the beryllium window, the gold contact, and the active and the dead silicon layer of the detector, respectively.

The  $k$  ratios obtained by comparing experimental spectra with calculated standard intensities may be used as concentrations of first approximation following the iteration correction until convergence is achieved.<sup>(9,49)</sup>

#### 8.1.4 Quantitative Analysis of Thin Films and Particles

Thin films and particles are conveniently analyzed in AEM by high-energy electron beams with accelerating voltages not less than 80 keV. Under these conditions, the effect of electron backscattering is minimal and electron energy losses in the specimen are rather small. For specimens in which the thin-film criterion is fulfilled, i.e. the X-ray absorption is < 3% and/or fluorescence < 5%, the atomic number correction can be neglected and the characteristic X-ray intensity of element  $i$  produced can be expressed according to the following equation<sup>(51)</sup>:

$$I_i = K \varepsilon_i c_i \omega_i Q_i a_i \frac{t}{A_i} \quad (30)$$

where  $K$  is a constant,  $\varepsilon_i$  is the efficiency of the EDS detector to detect X-ray emission from element  $i$ ,  $c_i$  is the mass concentration of element  $i$ ,  $\omega_i$  is the fluorescence yield for the analyzed X-ray peak of element  $i$ ,  $a_i$  is the measured fraction of total series intensity,  $t$  is the film thickness, and  $A_i$  is the atomic weight of element  $i$ . To avoid the influence of the substrate, the particles should be deposited on thin-film supports of low atomic number such as carbon. Furthermore, the particles should be scanned in a raster because in general the uniformity of the beam density cannot be assured when the probe diameter is comparable to or larger than the particle size.

In practice, it is suitable to measure the relative concentration of element  $i$  to another element  $j$ , which can be given by the following equation<sup>(52)</sup>:

$$\frac{c_i}{c_j} = k_{ij} \frac{I_i}{I_j} \quad (31)$$

where  $c_i$  and  $c_j$  are the mass concentrations of elements  $i$  and  $j$ , respectively,  $I_i$  and  $I_j$  are their corresponding X-ray line intensities, and  $k_{ij}$  is the Cliff–Lorimer sensitivity factor. The sensitivity factors can be related to an inner

standard element by the following equation :

$$k_{ij} = \frac{k_{i,\text{is}}}{k_{j,\text{is}}} = \frac{k_i}{k_j} \quad (32)$$

where  $k_{i(j),\text{is}} = k_{i(j)}$  are the relative sensitivity factors. The index is usually referred to silicon and iron commonly used as internal standard (is) elements. The tabulated experimental values of the sensitivity factors for K-, L-, and M-line emission from various elements are available.<sup>(52–55)</sup> It is also possible to calculate the sensitivity factors using a set of parameterized equations.<sup>(51,56)</sup>

Equation (31) may be expanded to take into account the effects of absorption and fluorescence as follows (Equation 33):

$$\frac{c_i}{c_j} = k_{ij} \frac{I_i}{I_j} k_a \frac{1}{1 + I_i^i/I_0^i} \quad (33)$$

where  $I_i^i$  and  $I_0^i$  are the fluorescent and primary X-ray intensities of  $i$ , respectively, and  $k_a$  is the absorption factor given by the following equation<sup>(50)</sup>:

$$k_a = \frac{(\mu/\rho)_{\text{sp}}^i}{(\mu/\rho)_{\text{sp}}^j} \frac{1 - \exp[-\chi^i(\rho t)]}{1 - \exp[-\chi^j(\rho t)]} \quad (34)$$

The parameterless extrapolation method proposed by Van Cappellen<sup>(57)</sup> is based on measurements of the relative intensities  $I_i/I_j$  at various thicknesses following extrapolation to zero thickness ( $I_i = 0$ ) by plotting  $I_i/I_j$  versus  $I_i$ . Then, if the secondary emission of the elements is much smaller than the primary emission, the mass concentration ratio can be determined, such as (Equation 35)

$$\frac{c_i}{c_j} = k_{ij} \lim_{t \rightarrow 0} \frac{I_i}{I_j} \quad (35)$$

Other methods based particularly on convergence between two or more different measurements for simultaneous determination of film composition and thickness and Monte Carlo techniques are discussed in the literature.<sup>(9,20,50,51)</sup>

## 8.2 Quantitative Electron Energy-Loss Spectroscopy

Inelastically scattered electrons produce a complex EEL spectrum briefly described in Section 2.3. For low energy losses, an EEL intensity expressed as the differential cross section  $d^2\sigma/d\Omega dE$  is related to the imaginary part of the reciprocal complex dielectric permittivity  $\varepsilon(\mathbf{q}, E)$  as a function of wave vector  $\mathbf{q}$  and energy  $E$ . It thus reflects the local dielectric response of the media to a longitudinal



field (Equation 36):

$$d^2\sigma/d\Omega dE \propto 1/q^2 \quad \text{Im}(-1/\varepsilon(\mathbf{q}, E)) \quad (36)$$

Here  $\varepsilon(\mathbf{q}, E) = \varepsilon_1 + i\varepsilon_2$ . The real part describes the dispersion (polarizability), while the imaginary part is related to electromagnetic absorption in the specimen in the  $\mathbf{q} = 0$  limit. The optical constants  $\varepsilon_1(\mathbf{q}, 0)$  and  $\varepsilon_2(\mathbf{q}, 0)$  can be extracted from the energy-loss function  $\text{Im}(-1/\varepsilon(\mathbf{q}, 0))$  using Kramers–Kronig transformations because of the causality involved in the dielectric response. Quantitative analysis of the low-loss EEL spectra allows useful information about local joint densities of states, interband transitions and band structure, bandgap, bonding, and dielectric and optical properties to be obtained.<sup>(3–6,17,18)</sup>

With increasing interest in the mechanical and transport properties of nanostructured materials, the fact that strong scaling correlations exist between the plasmon energy and valence-electron density, cohesive energy, elastic moduli, hardness, and other solid-state parameters of some nanophase materials (structural alloys, carbon fibers, and diamondlike coatings) leads to a resurgence of interest in this part of the low-loss spectrum.<sup>(30)</sup> As a consequence of the universal binding energy relation (UBER), a fundamental scaling relation exists for materials with preferential metallic or covalent bonding between the cohesive energy,  $E_{\text{coh}}$ , the bulk modulus,  $B_m$ , and the volume plasmon energy,  $E_p$ <sup>(78)</sup> (Equation 37):

$$B_m = (1/12\pi)r_{\text{wse}}^{-3}E_{\text{coh}}\eta^2 \\ = (\varepsilon_0 m_0 / 9e^2 \hbar^2 N_{\text{ve}}) E_{\text{coh}} \eta^2 (E_p^2 - E_g^2) \quad (37)$$

Here  $r_{\text{wse}} = (3/4\pi V_{\text{wse}})^{1/3}$  the equilibrium Wigner–Seitz (WS) atomic radius,  $\eta = r_{\text{wse}}/l$  is the dimensionless anharmonicity parameter,  $l$  is the characteristic length describing the width of the binding energy curve or the range over which strong forces act (this sets the range of the Hooke's law region),  $N_{\text{ve}}$  is the number of valence electrons per atom, and  $V_{\text{wse}}$  is the WS volume per atom.  $E_p = \hbar\omega_p \cong [(\hbar\omega_p^f)^2 + E_g^2]^{1/2}$ , where  $\omega_p^f = [ne^2/(\varepsilon_0 m)]^{1/2}$  is the free electron plasma frequency,  $n$  is the valence electron density,  $e$  is the electron charge,  $\varepsilon_0$  is the permittivity of vacuum,  $m$  is the electron mass, and  $E_g$  is the bandgap energy.

The origin of the connections lies in the nature of electron–ion (atom nuclei) interactions and in the essential exponential decay of electron density with interatomic distance. Figure 27 shows 3-D correlations between  $E_p$ , experimental and self-consistent local density functional (LDF) calculated elastic constants, and bonding densities at the boundary of WS cells for polycrystalline and single-crystal monoelement materials.

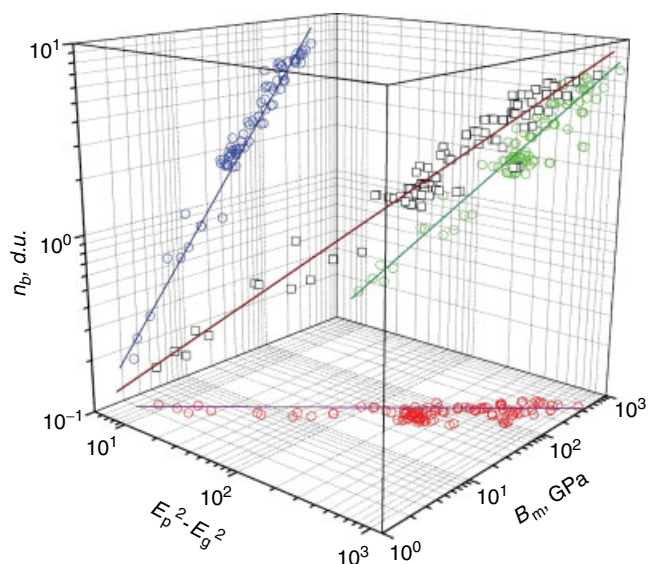


**Figure 27** Three-dimensional correlations between the electron density at the boundary of WS cells,  $n_b$ , the bulk modulus,  $B_m$ , and  $E_p^2 - E_g^2$  for monoelemental materials. Solid lines represent lsf-linear regressions of the type  $\lg P_m = A + B \lg E_p$ , where  $P_m = n_b$  or  $B_m$  ( $A$  and  $B$  are lsf-parameters of linear regressions with the correlation coefficient,  $R \geq 0.95$ ).  $n_b$ , d.u. (1 d.u. =  $6 \times 10^{22}$  el  $\text{cm}^{-3}$ ) is the electron density at the boundary of WS cells (upper left inset),  $\lg n_b = -1.5 + 0.8 \lg (E_p^2 - E_g^2)$ ,  $R = 0.96$ ;  $B_m$  is the LDF calculated bulk modulus and average experimental bulk modulus for 58 polycrystalline metals, B, C, Si, and Ge,  $\lg B_{\text{mcal}} = -0.79 + 1.1 \lg (E_p^2 - E_g^2)$ ,  $R = 0.96$ , and  $\lg B_{\text{mexp}} = -0.79 + 1.1 \lg (E_p^2 - E_g^2)$ ,  $R = 0.95$ , respectively.

The correlations reflect the dominant role of the valence electron density as a basic factor in determining the solid-state properties.<sup>(79)</sup>

These findings suggest that the volume plasmon energy can be used to investigate the nanoscale properties of engineering materials. Of course, other factors such as effects of the band structure, crystal symmetry, type of bonding, and size confinement should be also taken into account in specific cases. Determination of materials properties is necessary for understanding the behavior of contemporary nanostructured materials to provide ultimate performance and fully use their technological advantages. It is, however, difficult or sometimes impossible to measure elastic, cohesive, thermal, and electrical properties of small particles or metastable nanoprecipitates because of limitations due to their specific geometry (small size), complex morphology or high reactivity. Therefore, nanoscale analyses of physical properties by valence electron energy-loss spectroscopy (VEELS)/EFTEM (plasmon spectroscopic property imaging) when it is difficult or impossible by any other means offer attractive opportunities for material research.<sup>(6,78,79)</sup>

Multiple scattering can alter the EEL spectrum (Figure 26a and b, curve 1), taking the form of one or more low-loss excitations if the specimen thickness is of the order of or more than the estimated inelastic mean free path. Multiple scattering effects can be removed from the spectra using a number of procedures, although the most commonly employed procedures are based on fast Fourier transforms and are known as *Fourier-log* and *Fourier-ratio techniques*.<sup>(58,59)</sup>

For Fourier-log deconvolution, the recorded spectral intensity may be written in the form of the following equation<sup>(59)</sup>:

$$J(E) = \sum_n C_n [R(E) \otimes S_n(E)] \quad (38)$$

where  $R(E)$  is a unit-area resolution function,  $\otimes$  represents a convolution with respect of energy loss,  $S_n(E)$  is the  $n$ -fold self-convolution of the single scattering distribution (SSD),  $S(E)$ , and the Poisson coefficient  $C_n = I_0^{n-1}/n!$ . The Fourier transform of Equation (37) gives a simple product, and taking into account that the zero-loss profile  $Z(E) = I_0 R(E)$ , one can obtain the following equation:

$$\begin{aligned} j(v) &= \sum C_n r(v) [s(v)]^n = I_0 r(v) \exp \left[ \frac{s(v)}{I_0} \right] \\ &= z(v) \exp \left[ \frac{s(v)}{I_0} \right] \end{aligned} \quad (39)$$

The SSD (Figure 26a and b, curve 2) may be computed as the inverse Fourier transform of the following equation:

$$s(v) = I_0 \ln \left[ \frac{j(v)}{z(v)} \right] \quad (40)$$

where  $j(v)$  and  $z(v)$  are the Fourier transforms of the experimental EEL spectrum and of the zero-loss peak, respectively.

For quantitative EELS, the number  $n_a$  of atoms of element  $i$  per unit area may be obtained as the following equation<sup>(6)</sup>:

$$n_a = \frac{1}{\sigma_i(\alpha, \Delta)} \frac{N_i(\alpha, \Delta)}{N_0(\alpha, \Delta)} \quad (41)$$

where  $\sigma_i(\alpha, \Delta)$  is the partial cross-section for ionizations, which result in scattering of the PE within  $0 \leq \theta \leq \alpha$  and the energy-loss region with an energy window of width  $\Delta E_1 \leq \Delta E \leq E_1 + \Delta$ ;  $N_0$  and  $N_i$  are the number of electrons in the range  $0 \leq \Delta E \leq \Delta$  and  $E_1 \leq \Delta E \leq E_1 + \Delta$ , respectively.

As in X-ray analysis, a ratio method is used to determine the relative number of atoms  $n_i/n_j$  of two elements

(Equation 42):

$$\frac{n_i}{n_j} = \frac{N_i \sigma_j(\alpha, \Delta)}{N_j \sigma_i(\alpha, \Delta)} \quad (42)$$

## 9 APPLICATIONS

Examples selected in this section demonstrate some practically important EM applications such as in situ real-time environmental transmission electron microscopy (ETEM) of gas phase Ziegler–Natta (ZN) catalytic polymerization of propylene (Section 9.1), electron tweezers (Section 9.2), EPXMA particle analysis of populations of mixed silver halide microcrystals of industrial photographic emulsions under cryogenic conditions (Section 9.3), combined WDS/EDS X-ray compositional mapping (Section 9.4.1), EELS spectrum imaging and image spectrum (Section 9.4.2), and local specimen thickness determination (Section 9.5).

### 9.1 In Situ Real-Time Environmental Transmission Electron Microscopy of Gas Phase Ziegler–Natta Catalytic Polymerization of Propylene

Catalytic ZN polymerization is the major industrial process for manufacturing of  $\alpha$ -polyolefins and their copolymers. In contemporary heterogeneous ZN catalysts, a  $\text{TiCl}_4$  active component is chemisorbed onto the high-surface-area-defective  $\text{MgCl}_2$  support and an alkyl-aluminum cocatalyst is complexed with electron donors. In spite of continuing progress in developing high activity commercial polypropylene (PP) catalysts, present understanding of ZN catalysis is incomplete. Its high sensitivity to trace impurities, poisoning, and the complexity of the multitude component catalyst has led to a multitude of local site environments. From a practical point of view, the actual need is to control precisely the growth of the catalyst/polymer particle during the polymerization process. The relationships between the catalyst/polymer structures, process conditions, and final product properties should be clarified in more detail. Real-time ETEM (Figure 28) at intermediate pressure of a few torr is able to provide direct information on the local reaction kinetics and evolution of catalyst nanostructure and PP growth morphology during the very early stages of the polymerization corresponding to about 2 monomer insertions per second.<sup>(80)</sup>

### 9.2 Electron Tweezers

Nondestructive trapping of small particles in a liquid by a laser beam, which is refracted by the particle and transfers momentum to it, is known as *optical tweezers*. Gradient electromagnetic forces in optical

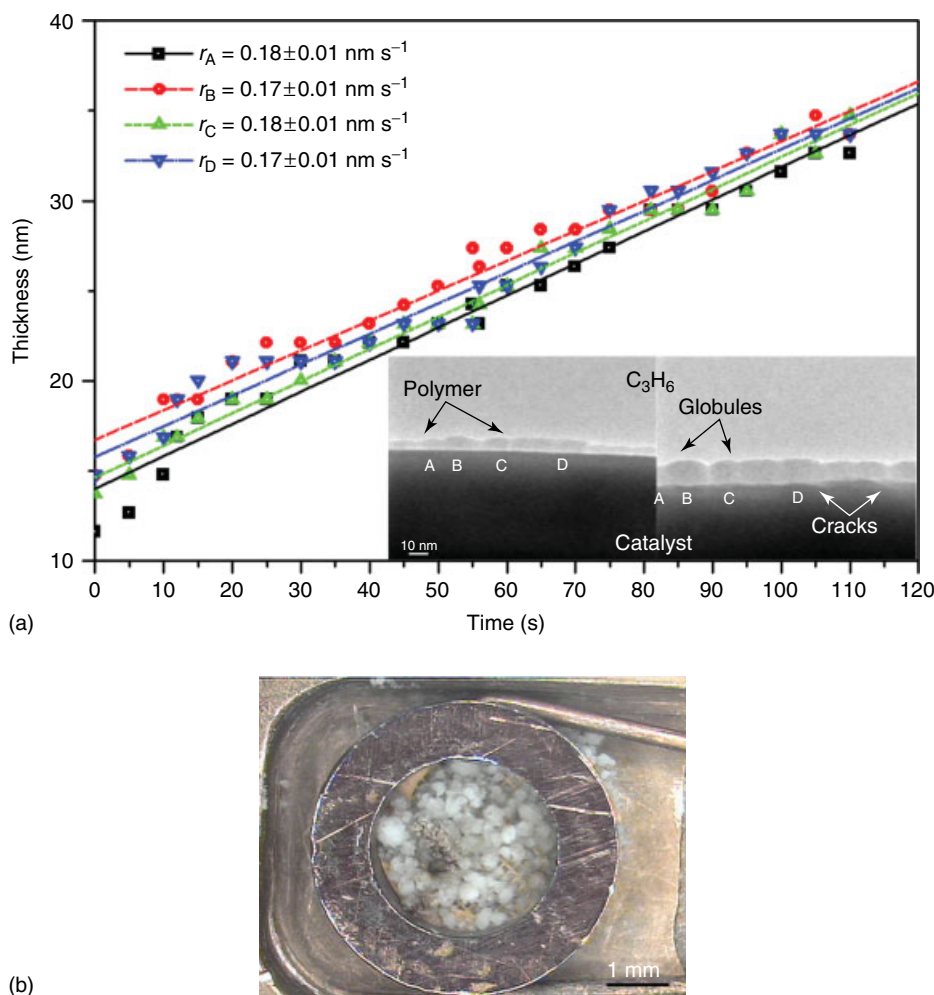


**Figure 28** (a) Local kinetics of PP growth derived directly from video images. (a) The time growth for the thickness of a nonuniform polymer layer growing at 25° C on a relatively flat catalytic surface in about 1 torr of C<sub>3</sub>H<sub>6</sub> in selected points A, B, C, and D, respectively, as shown in zero-loss filtered TEM images. Time separation between left and right images is 100 s. (b) Color light microscopy photograph of PP beads grown in an ETEM on the Au microscope grid, reflection mode.

tweezers have been employed to trap dielectric and metal particles ranging in size from tens of nanometers to several micrometers, and to manipulate them in all spatial directions. Analogously, recent experiments have demonstrated thermally assisted electron tweezers, i.e. trapping and stirring of solid Al nanospheres by transferring linear and angular mechanical momenta from an electron beam.<sup>(81)</sup> About 20–100 nm particles formed inside molten opaque 100–400 nm Al–Si eutectic alloy droplets were monitored in real time by EFTEM (Figure 29).

It is anticipated that extending optical trapping down to the nanoscale could enable ultra-accurate positioning of nanoobjects at the atomic level lateral resolution and sensitivity provided by S/TEMs. This is by three orders of magnitude better than for light microscopy used in conventional optical tweezers. Implementation of

electron nanotweezers could facilitate real-time manipulation of nanoparticles and even single atoms in confined volumes and at atomically flat and curved surfaces, 3-D-assembly of nanostructures, separation and sorting of nanoparticles in oscillating electromagnetic fields, coupling with laser optical tweezers for enhancing surface plasmon resonances, and levitation of unsupported nanoobjects.

### 9.3 Automated Population Analysis: Size–Thickness–Elemental Composition

Figure 30(a–c) shows (i) a typical X-ray spectrum, (ii) some results on elemental compositions, and (iii) thickness analyses obtained by cryo-EPXMA for 700 Ag (Br, I) microcrystals of an industrial photographic emulsion.<sup>(60)</sup> A JEOL JXA-733 electron microprobe operating at a 25 kV accelerating voltage and 1 nA

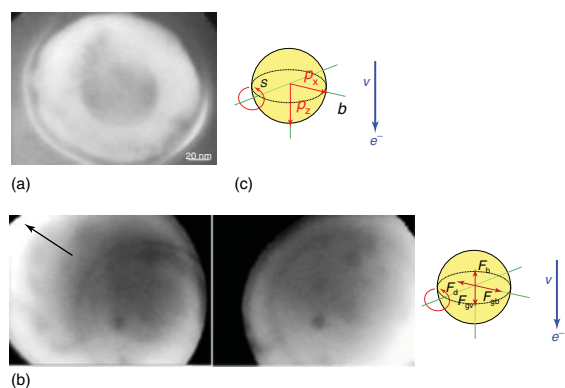


**Figure 29** In situ ‘ball-in-ball’ EFTEM, 15 eV energy loss, a 6 eV window. (a) Electron-beam-assisted generation of a 70-nm-diameter solid particle inside a partially molten Al-11.6 at. % Si sphere surrounded by a 10-nm-thick oxide shell. (b, c) Steering of a solid particle by translating the beam in the direction shown by the arrow and/or moving the microscope stage in the opposite direction. The video frame (b) is separated from the frame (c) by 17 s. The inset in (a) describes transfer of a momentum  $\mathbf{p} = (p_x, p_z)$  of a fast electron with impact parameter  $b$  and velocity  $v$  to a polarizable particle via electromagnetic interaction. Here,  $S$  is a surface embedding the particle. The inset in (c) schematically describes forces exerted on the trapped particle.  $F_{gv}$ ,  $F_d$ ,  $F_b$ , and  $F_{gd}$  denote gravitational, drag, buoyant, and gradient forces, respectively.

beam current was equipped with a Noran Si(Li) EDS detector placed at a take-off angle of  $40^\circ$ , a Wolf–Everhart BSE detector, an Everhart–Thornley SE detector, a scintillator TE detector, and a transmission specimen holder. The crystal size was determined by SE/BSE imaging, the thickness was estimated from

the BSE intensity, and the X-ray spectra provided the required composition information. However, to perform automated analyses, several serious problems had to be overcome. First, the AgX ( $X = \text{Br}, \text{I}$ ) microcrystals are not only sensitive to light irradiation but also degrade rapidly under the influence of the electron beam. Under normal analysis conditions, the crystals are often destroyed within seconds owing to the partial evaporation of halogens. Lowering the sample temperature to about  $-190^\circ\text{C}$  by the use of a liquid-nitrogen-cooled Oxford C10001 cryo-stage increased the resistance against radiation damage, thus allowing an X-ray analysis during 20 s or more.

Sample cooling inevitably caused sample drift; large temperature differences inside the microprobe instrument led to metal shrinkage, which in turn resulted in unpredictable motion of the sample under the electron beam. This drift continued for several hours after sample insertion and was far too large (about  $50 \text{ nm min}^{-1}$ ) for the usual particle analysis software; indeed, the detected particles had moved away from their detected position before their X-ray spectrum acquisition even began. The problem was resolved by employing an original algorithm, which detects and analyzes particles sequentially during (and not following) the BSE image acquisition.

Particles were distinguished from the background by selecting a threshold value. To avoid missing small or very thin crystals, the threshold value was set as close to the background as possible. Owing to the limited sharpness of the BSE image, however, this might sometimes cause an overestimation of the projected area or diameter of the crystal. An accurate area

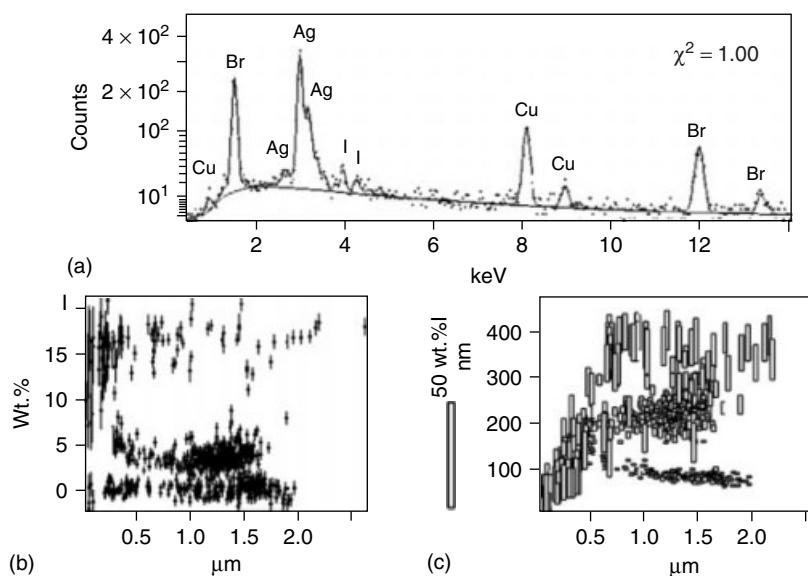


**Figure 30** (a) X-ray spectrum of an Ag (Br, I) microcrystal, (b) iodine content (wt.%) of 700 crystals as a function of crystal diameter (micrometer) showing standard deviations on iodine concentrations, and (c) iodine content of the population as a function of crystal diameter (micrometer) and thickness (nanometer). Background fitted by least squares is shown in (a).

determination was achieved by setting a second threshold value, different for every particle, halfway between the background image brightness and the maximum particle brightness. If the number of particle pixels rejected by this second threshold was too large, this was considered as an indication that the detected structure was in fact composed of overlapping particles. Therefore, it was eliminated from the analysis. The occurrence of large shape factor ( $\text{perimeter}^2/4\pi \times \text{area}$ ) values indicates touching or overlapping of crystals; they were also eliminated.

Since the crystals were very thin and high-beam currents were undesirable because of possible crystal destruction, the X-ray emission was relatively low. Therefore, a large  $30\text{ mm}^2$  area Si(Li) detector placed as close as possible to the sample was used. The crystals were mounted on a very thin supporting foil (e.g. carbon foil on copper grid) using a transmission holder to reduce the bremsstrahlung background. Net peak intensities used for the accurate determination of the crystal composition were obtained by means of least-squares fitting.

## 9.4 X-ray and Electron Energy-Loss Spectroscopic Imaging

In spectroscopic imaging (SI), a multidimensional data set is generally obtained by combining SEM, STEM or (EF)TEM 2-D spatially resolved imaging with X-ray EDS, WDS, EELS, or CL-spectroscopy modes (the third dimension) and, sometimes, with time or a diffraction pattern at each probe position, for example (the fourth dimension). Using scanning beam EM techniques, the spectral image can be acquired simultaneously with various signals, thus potentially allowing absolute correlation of the spectroscopic and structural data pixel-by-pixel using drift compensation, followed by multivariate statistical analysis. As a result of significant instrumentation advances in the last decade, multiscale SI primarily using X-ray EDS, EELS, and CL is already changing the way of conducting materials research. It is expected that STEM/EELS/EDS SI in aberration-corrected atomic resolution and single-atomic sensitivity AEMs will provide unprecedented new insights into structures, bonding and the origin of material properties.

### 9.4.1 Combined WDS/EDS X-ray Mapping

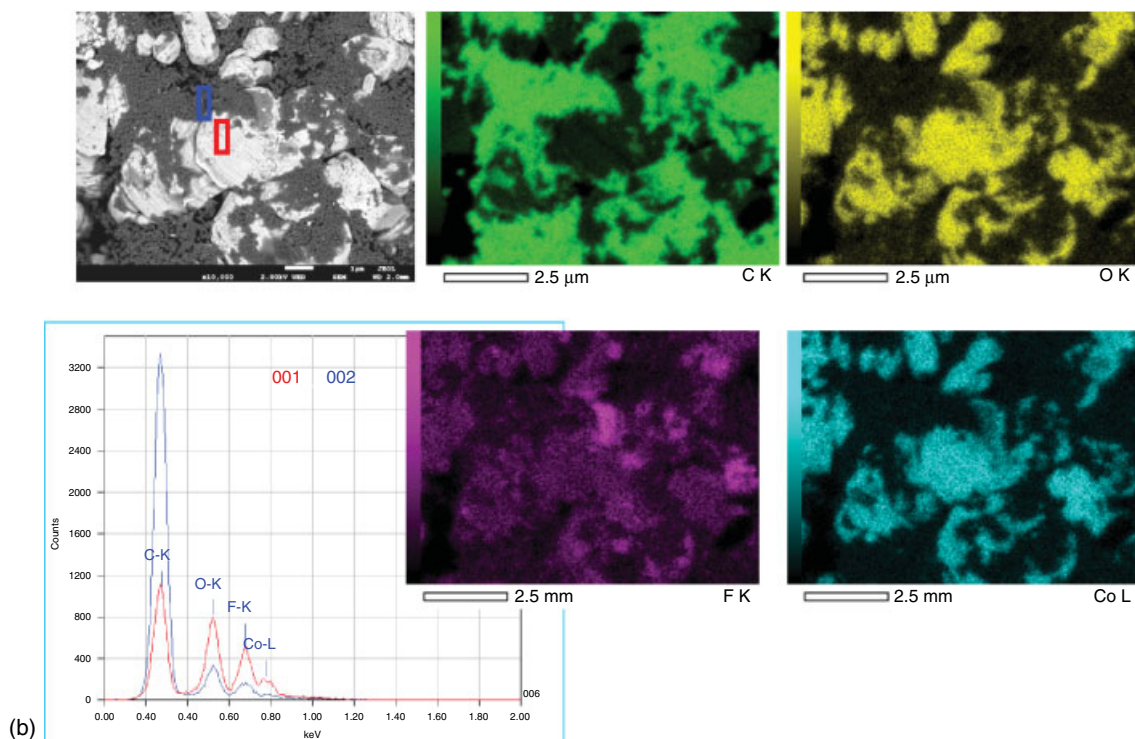
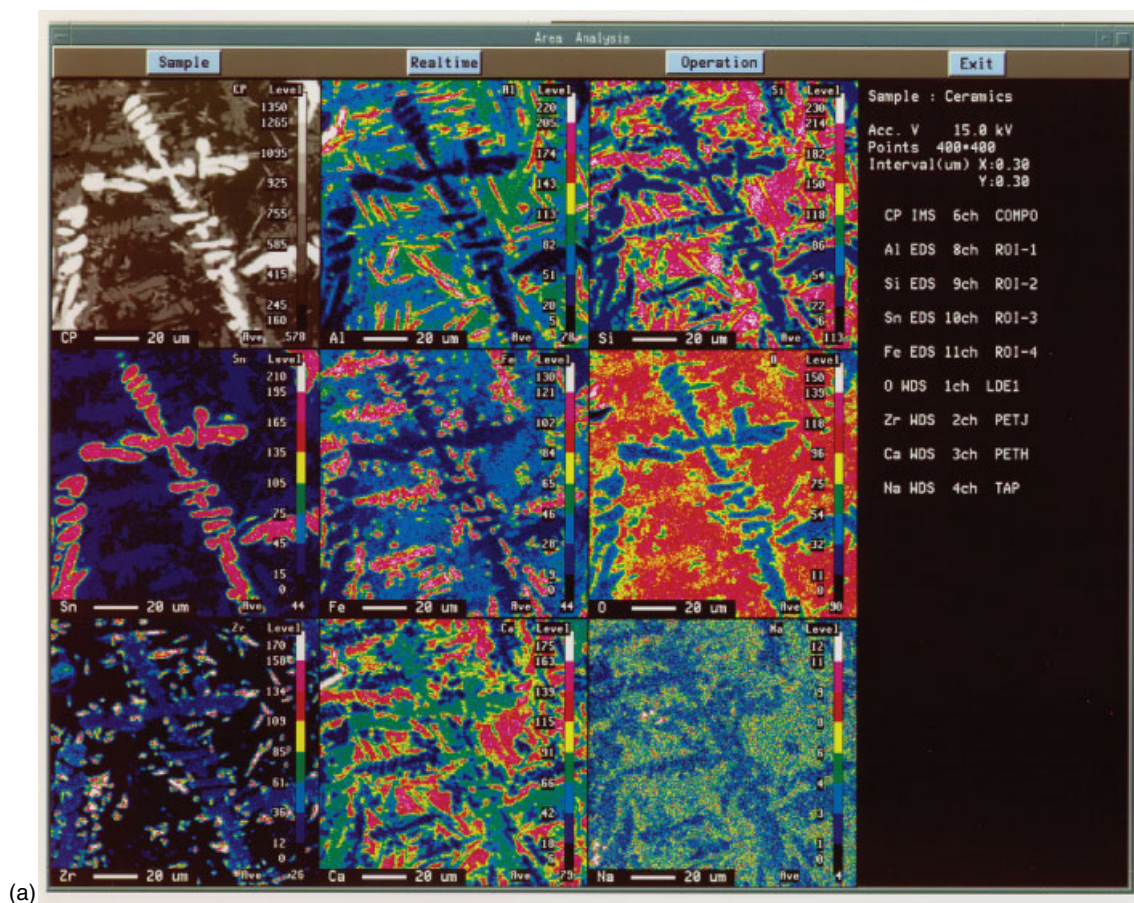
X-ray maps provide valuable information on 2-D elemental distributions over bulk or thin samples.<sup>(3–5,9,20,22,23,30,50)</sup> X-ray mapping can be undertaken with both EDS and WDS, where incoming counts for elements of interest are fed back into the SEM or STEM instrument. The X-ray analyzer takes control over the electron beam via a special interface, driving the beam around in a rectangular frame and collecting the X-ray emission for each pixel separately. An external beam deflection interface allows X-ray mapping by beam rocking also on TEM instruments using the standard hardware and software. In the case shown in Figure 31(a), combined WDS/EDS X-ray composition maps of an Na–Al–Si–Ca–Fe–Zr–Sn–O ceramic were acquired on a JEOL JXA-8900 WDS/EDS combined automated microanalyzer operating at 15 kV accelerating voltage. The simultaneous composition measurements of eight constituent elements by EDS (Al, Si, Fe, and Sn) and by WDS (O, Na, Ca, and Zr) and BSE imaging in a ‘compo’ mode were performed on a  $140 \times 140\text{ }\mu\text{m}^2$  area. Using the FEG with much higher beam currents in the next generation of EPXMA systems allows high count rates with a correct probe shape while maintaining significantly improved spatial resolution even at low accelerating voltages (<2 kV, Figure 31b)

Color compositional maps represent spatially resolved X-ray multielemental analysis within the chosen region of the sample. However, it is often difficult to visualize the compositional ranges and resulting interelement correlations from the map, particularly for minor or trace constituents. As an alternative method, a composition–composition histogram displaying the numerical relationship between concentrations of the components at various points of the sample can be proposed.<sup>(50)</sup>

The SE/BSE images are normally used to select regions for subsequent X-ray mapping. If features of interest are not differentiated in the monochrome black–white electron image, then they can easily be overlooked for further analysis. Using the X-ray spectrum detected by EDS, one can construct a color response directly related to the underlying elemental composition where the spectrum from each compound has a characteristic color. Thus, topography and elemental composition of a specimen are compressed into a single view. Furthermore, using this technique, it is not necessary to monitor the

**Figure 31** (a) WDS/EDS combined  $140 \times 140\text{ }\mu\text{m}^2$  area analysis of an Na–Al–Si–Ca–Fe–Zr–Sn–O ceramic,  $400 \times 400$  points. X-ray maps of eight constituent elements and BSE image (‘compo’ mode, CP) recorded at an accelerating voltage of 15 keV. Mapping was performed simultaneously by EDS (Al, Si, Fe, and Sn) and WDS (O, Na, Ca, and Zr) (Courtesy of Dr R. Herstens, JEOL (Europe) B.V., Belgium). (b) Ultralow kilovolt BSE imaging and X-ray EDS mapping of a cathode material in a Li-ion battery. Analyses were performed at 1.2 kV accelerating voltage and 6 nA probe current at magnification of  $10000\times$  on a JEOL JXA-8530F HyperProbe Probe Microanalyzer. (Courtesy of Dr V. Robertson and Dr C. Nielsen, JEOL, USA.)





X-ray spectrum, set windows, or collect X-ray maps. Compositional data even in samples with a rough surface are automatically acquired into the SEM images because the colors displayed always relate to the sample composition.<sup>(20,22,23)</sup>

#### 9.4.2 Electron Energy-loss Spectroscopic Spectrum-imaging and Image-spectrum

Using an EEL spectrometer (and/or EDS) fitted to a dedicated STEM instrument (FEG-VG H501) and/or TEM/STEM (a Hitachi H700H and a Philips EM430 were first used), a large 4-D data array may be recorded, which corresponds to electron intensity within a 3-D ( $x, y, E$ ) space, one independent scattering angle dimension and a dependent counts dimension.<sup>(6,16,61,62)</sup> Here  $x$  and  $y$  are image coordinates and  $E$  is the selected energy loss. A similar series of energy-filtered images at different energy losses can be also acquired using EFTEM equipped with an imaging filter (image spectrum<sup>(16,63)</sup>).

These techniques enable one to collect a very large amount of information for subsequent off-line processing to subtract the pre-edge background, to calculate local thickness, and to perform mean least-squares fitting, deconvolution, and Kramers–Kronig analyses. The data may be displayed as line scans, 2-D arrays of spectra or 2-D images of elemental concentration, thickness, complex dielectric permittivity, etc. Furthermore, EFTEM tomography is an area where emerging nanotechnology applications are expected, especially with regard to high precision manufacturing of the devices in a controlled manner from the atom/molecule upward.<sup>(1,2,17,18,30)</sup> The ability of EFTEM/EELS SI and, to some extent, X-ray EDS SI to reveal the actual morphology (shapes/sizes) combined with the quantitative local chemistry of devices and their components (NEMS/MEMS, quantum dots, gate oxides, and other sub-nanometer fabrications) will surely enhance the EM's role in these rapidly growing fields.

### 9.5 Sample Thickness Determination

A need for the determination of the local specimen thickness is associated with absorption and/or fluorescence corrections and estimation of the spatial analysis resolution (EDS) and with multiple scattering corrections (EELS). Several means for measuring specimen thickness have been proposed (Table 5), but not one technique has been recognized as universal, although methods based on absorption of X-rays, EELS, and CBED may be recommended because they provide possibilities for automated on-line procedures.

## 10 CURRENT TRENDS

Since the discovery of the electron, the focused electron beam has been established as the most complete functional probe used for the characterization of materials. Electron beams are also suitable for probing local excitations of matter and direct processing and fabrication. The current state of the art in materials characterization is largely based on surface and internal electron imaging by (FE)SEM, TEM STEM, and HRTEM, crystallographic measurements by EBSD, SAED, CBED, and NBD, and compositional analyses using beam-induced EDS, WDS, EELS, and EFTEM.

The last two decades have shown remarkable progress in the instrumentation due to the successful correction of spherical and chromatic aberrations of electron lenses that enabled 50–80 pm spatial resolution in S/TEM and 0.1 eV energy resolution due to the incorporation of monochromators in combination with much higher current in a focused probe produced using Schottky and cold field-emission electron sources ( $\sim 10^8$ – $10^9$  A cm<sup>-2</sup> sr<sup>-1</sup>). These capabilities have significantly boosted both imaging and analytical modes. The computer software for data simulation and processing (3-D tomography reconstruction, spectral imaging, spectral spatial deconvolution, multivariate statistical analysis) and methodologies for fully quantitative and standard-less procedures, automatic instrumentation, low-voltage microanalysis of light elements, and super-high-sensitivity analyses at nanometer and sub-nanometer lateral resolution have been further improved.

Today, integrated S/TEMs, (FE)SEM, EPXMA, and AES/SAMs are equipped with multiple detector systems to detect with high efficiency both the effects of elastic and inelastic interactions of electron beams within the object. Powerful operating modes such as BF/DF-TEM, STEM, SEM, Lorentz microscopy, electron and X-ray diffraction (SAED, CBED, NBD, electron channeling, Kikuchi patterns), EH, stereo observations, spectroscopy, and spectroscopic imaging (EDS, WDS, EELS/EFTEM, CL, AES/SAM) can be used independently or in various combinations. As a result, conventional TEMs and SEMs have evolved from a purely imaging/diffraction microscopy instrument into multifunctional nanoscopy tools employing most of the signals produced in the course of electron beam-sample interactions. Although for ultimate performance, it is still mostly better to optimize an instrument for that particular purpose (for instance, as in the case of a dedicated high-resolution STEM). In HRTEM and STEM Z-contrast modes, spatial resolution (below 0.1 nm) has reached the atomic level. In high-resolution FESEM, one can achieve resolution of medium-resolution TEM but for bulk specimens. Recent



**Table 5** EM methods for the measurement of specimen thickness<sup>(3–6,30,59)</sup>

EM method	Signals used	Samples	Thickness–signal relation
CTEM	TE	Cross-sections	Direct measurement
CTEM	TE	Thin films	Beam current measurement vs thickness using a Faraday cup followed by densitometric calibration
CTEM	TE	Shadowing of latex particles, shadowed replicas, small fold	Direct measurement
CTEM	TE	Tilting of small latex spheres deposited on both sides	Measurement of parallax shift between balls on the top surfaces and bottom sides
CTEM	BSE	Thin films	Measurements of backscattering coefficient vs thickness using the equation $\eta = \text{constant} \times N_A Zt$
SEM	SE	Cross-sections, fractures	Direct measurement
SEM	Characteristic X-rays	Thin films on bulk support	Measurement of X-ray intensity vs thickness, accelerating voltage followed by calibration with standards
CTEM/STEM	TE	Contamination spots	Measurement of separation between spots on the top and bottom surfaces
CTEM/STEM	TE	Features intersecting both surfaces (faults)	Projection measurements of tilted and untilted features against the beam
CTEM/STEM/EELS	Zero-loss/ inelastically scattered electrons	Thin films	Relative and absolute measurements using a parameterized equation, $I_t/I_0 = t/\lambda$ . Bethe sum rule. Kramers–Kronig sum rule
CBED	TE	Thin crystalline films	Determination of deviations of diffraction fringes from the exact Bragg position
Off-axis EH	TE	Thin films	Interferometry of phase contour maps of equal phase shift combined with electron dynamic diffraction calculation of the phase shift vs specimen thickness

developments indicate rapid progress toward practical atomic-level analytical resolution.

Parallel EELS detection systems based on CCD offer better detection limits; they allow one to investigate simultaneously and with much higher efficiency not only the low losses but also the more local and less intense core losses up to 3000 eV. An integral energy filter/EELS spectrometer is a standard option on S/TEM instruments owing to the importance of EFTEM/EELS for associated imaging techniques such as elastic contrast, energy-loss tuning, and high-resolution electron spectroscopic elemental mapping. Recent developments in ultrasoft-X-ray emission spectroscopy in an energy range 50–200 eV for EPXMA and conventional TEM enable one to extend the analyzed elemental range to lithium (the Li K $\alpha$  at 55 eV) and to obtain partial density of states of valence electrons from selected specimen areas at an energy resolution better than 1 eV. Newly designed SDD detectors are rapidly replacing Si(Li) detectors for EDS microanalysis in SEM. The new designs enable higher count rate capability and subsequently throughput

improvement. In addition, they provide opportunities for high-speed sub-nanometer resolution X-ray STEM spectral imaging. Microcalorimeter EDS systems with an energy resolution of 3–10 eV allows the detection not only of closely spaced X-ray peaks but also of chemical shifts. To meet the complex and varying practical needs, EM methods are often coupled with other analysis techniques (FIB, Raman spectroscopy, X-ray fluorescence, X-ray tomography, Scanning tunneling microscopy (STM), atomic force microscopy (AFM), and XPS), e.g. for performing hyperspectral imaging.

Advances in nanotechnology are making real-time atomic-level control of the structure and composition increasingly desirable, e.g. in 0-D, 1-D (quantum dots, nanowires, and nanotubes), 2-D (graphene), and 3-D nanostructures (NEMS/MEMS, batteries, solar and fuel cells, sensors, and catalyst supports) due to their novel structures and unique properties. Furthermore, contemporary miniaturization tendency demands high precision EM micro- and nanometrology for providing picometer diameter electron beams. Hence, the versatility

of EM, combining high-resolution imaging, diffraction in different modes and powerful analytical facilities, the variety of signals, and contrast effects available in the course of electron beam–specimen interactions, establish it as an outstanding tool for universal applications and in situ experiments aimed at developing nanotechnology related to materials science, chemistry, physics, and biology. Future EMs will be key 3-D picoscopy tools capable of providing picoseconds time-resolved information ultimately spatially resolved at picometer scale. At the same time, it will be possible to probe and measure nanoscale material properties in situ by inducing various types of local optical, electric, thermal, and mechanical excitations under vacuum or in an ambient environment.

## ACKNOWLEDGMENTS

The authors are grateful to Dr R. Herstens, JEOL (Europe) B.V., Belgium, Dr V. Robertson, Dr C. Nielsen, JEOL (USA), Dr K. Tsutsumi, Electron Optics Division, JEOL Ltd., Dr M. Otten, S. von Harrach, S. Lazar, and M. Bischoff, FEI, former Philips Electron Optics, Eindhoven, the Netherlands, for providing valuable scientific and technical information. Critical reading of the article by Drs J.E. Bonevich, I. Levin, and D. Josell is gratefully acknowledged.

## ABBREVIATIONS AND ACRONYMS

ADF	Annular Dark Field
AE	Auger Electrons
AEM	Analytical Electron Microscopy
AES	Auger Electron Spectroscopy
AFM	Atomic Force Microscopy
BF	Bright Field
BSE	Backscattered Electrons
CBED	Convergent-Beam Electron Diffraction
CCD	Charge-Coupled Device
CL	Cathodoluminescence
CTEM	Conventional Transmission Electron Microscopy
DTEM	Dynamic Transmission Electron Microscopy
DE	Diffacted Electrons
DF	Dark Field
EBIC	Electron Beam-Induced Current
ED	Electron Diffraction
EDS	Energy-dispersive (X-ray) Spectroscopy
EEL	Electron Energy-Loss
EELS	Electron Energy-Loss Spectroscopy
EFTEM	Energy-Filtering Transmission Electron Microscopy

EH	Electron Holography
ELNES	Energy-Loss Near-Edge Structure
EM	Electron Microscopy
EMMA	Electron Microscope Microanalyzer
EP	Electron Plasmon
EPMA	Electron Probe Microanalysis
EPXMA	Electron Probe X-ray Microanalysis
ESD	Electron Spectroscopic Diffraction
ESEM	Environmental Scanning Electron Microscopy
ESI	Electron Spectroscopic Imaging
ET	Electron Tomography
EXELFS	Extended Energy-Loss Fine Structure
FE	Field Emission
FEG	Field-emission Gun
FIB	Focused Ion Beam
GIF	Gatan Imaging Filter
HAADF	High-Angle Annular Dark Field
HRTEM	High-Resolution Transmission Electron Microscopy
HVTEM	High-Voltage Transmission Electron Microscopy
IR	Infrared
LDE1	Layered Dispersion Element 1
LDE2	Layered Dispersion Element 2
LDEB	Layered Dispersion Element B
LDEN	Layered Dispersion Element N
LDF	Local Density Functional
LIF	Lithium Fluoride
LP	Lattice Phonon
MMF	Minimum Mass Fraction
MYR	Lead Myristate (Langmuir–Blodgett Fatty Acid Pseudocrystal)
NBD	Nanobeam Diffraction
PE	Primary Electrons
PEEL	Parallel Electron Energy-Loss
PET	Pentaerythrite
SAED	Selected-Area Electron Diffraction
SAM	Scanning Auger Microscopy
SC	Sample Current
SDD	Silicon Drift Detector
SE	Secondary Electrons
SEM	Scanning Electron Microscopy
SI	Spectroscopic Imaging
SNR	Signal-to-Noise Ratio
SSD	Single Scattering Distribution
STE	Lead Stearate
STEM	Scanning Transmission Electron Microscopy
STM	Scanning Tunneling Microscopy
TAP	Thallium Acid Phthalate
TE	Transmitted Electrons
TEM	Transmission Electron Microscopy
UV/IS	Ultraviolet/Visible

VLS	Varied-Line-Spaced (Grating)
VP-SEM	Variable-pressure SEM
WDS	Wavelength-Dispersive (X-ray) Spectroscopy
XPS	X-ray Photoelectron Spectroscopy or Electron Spectroscopy for Chemical Analysis (ESCA)

## RELATED ARTICLES

### Coatings (Volume 2)

Microscopy of Coatings

### Forensic Science (Volume 5)

Scanning Electron Microscopy in Forensic Science • X-Ray Fluorescence in Forensic Science

### Industrial Hygiene (Volume 5)

Aerosols and Particulates Analysis: Indoor Air

### Particle Size Analysis (Volume 6)

Particle Size Analysis: Introduction • Velocimetry in Particle Size Analysis

### Surfaces (Volume 10)

Auger Electron Spectroscopy in Analysis of Surfaces • Differential Reflectance Spectroscopy in Analysis of Surfaces • Electron Energy Loss Spectroscopy in Analysis of Surfaces • Scanning Electron Microscopy in Analysis of Surfaces • Scanning Tunneling Microscopy/Spectroscopy in Analysis of Surfaces

### Electroanalytical Methods (Volume 11)

Scanning Tunneling Microscopy, In Situ, Electrochemical

### Mass Spectrometry (Volume 13)

Secondary Ion Mass Spectrometry as Related to Surface Analysis

### X-Ray Photoelectron Spectroscopy and Auger Electron Spectroscopy (Volume 15)

X-ray Photoelectron Spectroscopy and Auger Electron Spectroscopy: Introduction • X-ray Photoelectron and Auger Electron Spectroscopy

### General Articles (Volume 15)

Archaeological Chemical Analysis • Spot Test Analysis

## REFERENCES

1. S. Amelinckx, D. Van Dyck, J. Van Landuyt, G. Van Tendeloo (eds), *Handbook of Microscopy*, VCH, Weinheim, Vols 1, 2, 1997.
2. G. Van Tendeloo, D. Van Dyck, S. Pennycook (eds), *Handbook of Nanoscopy*, Wiley-VCH, Weinheim, Vol. 1, 2012.
3. V. Oleshko, R. Gijbels, W. Jacob, M. Alifimov, 'Characterization of Complex Silver Halide Photographic Systems by Means of Analytical Electron Microscopy', *Microbeam Anal.*, **4**, 1–29 (1995).
4. V.P. Oleshko, R.H. Gijbels, W.A. Jacob, 'Analytical Electron Microscopy of Silver Halide Photographic Systems', *Micron*, **31**, 55–95 (2000).
5. V.P. Oleshko, 'Applications of Electron Microscopy in Photographic Science and Technology', in *Industrial Applications of Electron Microscopy*, ed. Z.R. Li, Marcel Dekker, New York, 51–112, 2003.
6. R.F. Egerton, *Electron Energy-loss Spectroscopy in the Electron Microscope*, 2nd edition, Plenum Press, New York, 1–29, 31–129, 245–299, 301–406, 1996; 3rd edition, Plenum Press, New York, 1–109, 231–291, 293–397, 2011.
7. J.J. Thomson, 'Cathode Rays', *Philos. Mag.*, **44**, 293 (1897).
8. The Nobel Prize in Physics 1986. Ernst Ruska, Gerd Binnig, Heinrich Rohrer. <http://www.nobelprize.org/nobel.prizes/physics/laureates/1986/>.
9. V.D. Scott, G. Love, S.J.B. Reed, *Quantitative Electron-probe Microanalysis*, 2nd edition, Ellis Horwood, New York, 1–75, 111–211, 1995.
10. P. Duncumb, 'Precipitation Studies with EMMA – a Combined Electron Microscope and X-ray Microanalyzer', in *The Electron Microprobe*, eds. T.D. McKinley, K.F.J. Heinrich, D.B. Wittry, John Wiley & Sons, New York, 490, 1966.
11. G. Rutherman, 'Diskrete Energieverluste Schneller Elektronen in Festkörpern', *Naturwissenschaften*, **29**, 648 (1941).
12. J. Hillier, R.F. Baker, 'Microanalysis by Means of Electrons', *J. Appl. Phys.*, **15**, 663–675 (1944).
13. R. Castaing, L. Henry, 'Filtrage Magnétique des Vitesses en Microscopies Electronique', *C. R. Acad. Sci.*, **B255**, 76–78 (1962).
14. M.T. Browne, 'Electron Energy Analysis in a Vacuum Generators HB5 STEM', *Scanning Electron Microscopy*, SEM Inc., AMF O'Hare, IL, Part 2, 827–834, 1979.
15. L. Reimer, 'Introduction and Electron Spectroscopic Imaging', in *Energy-filtering Transmission Electron Microscopy*, Springer Series in Optical Sciences, ed. L. Reimer, Springer, Berlin, 1–42, 347–400, Vol. 71, 1995.
16. Ch. Colliex, 'Electron Energy-loss Spectroscopy Imaging', in *Handbook of Microscopy*, eds. S. Amelinckx, D. Van Dyck, J. Van Landuyt, G. Van Tendeloo, VCH, Weinheim, 425–445, Vol. 1, 1997.
17. L. Reimer, 'Transmission Electron Microscopy', *Physics of Image Formation and Microanalysis*, 4th edition, Springer, Berlin, 1–15, 157–196, 251–273, 275–420, 423–461. 1997.

18. L. Reimer, H. Kohl, 'Transmission Electron Microscopy, Physics of Image Formation and Microanalysis', 5th edition, Springer, Berlin, 1–15, 77–194, 241–271, 273–416, 419–458, 2008.
19. F. Hofer, 'Inner-shell Ionizations', in *Energy-filtering Transmission Electron Microscopy, Springer Series in Optical Sciences*, ed. L. Reimer, Springer, Berlin, 225–268, Vol. 71, 1995.
20. V. Oleshko, R. Gijbels, 'Scanning Microanalysis', in *Handbook of Microscopy*, eds. S. Amelinckx, D. Van Dyck, J. Van Landuyt, G. Van Tendeloo, VCH, Weinheim, 661–690, Vol. 2, 1997.
21. D.E. Newbury, 'Monte Carlo Electron Trajectory Simulation for Electron Probe Analysis: Present Utility and Future Possibilities', *Microbeam Anal.*, **1**, 9–17 (1992).
22. V. Oleshko, R. Gijbels 'Scanning Microanalysis', in *Electron Microscopy, Principles and Fundamentals*, eds. S. Amelinckx, D. Van Dyck, J. Van Landuyt, G. Van Tendeloo, Wiley-VCH, Weinheim, 427–456, 1997.
23. J.I. Goldstein, D.E. Newbury, D.C. Joy, C.E. Lyman, P. Echlin, E. Lifshin, L. Sawyer, J.R. Michael, *Scanning Electron Microscopy and X-ray Microanalysis 3<sup>rd</sup> edition*, Kluwer Academic/Plenum Publ, New York, 1–673, 2003.
24. P.B. Hirsch, R.B. Nicholson, A. Howie, D.W. Pashley, M.J. Whelan, *Electron Microscopy of Thin Crystals*, 2nd edition, Butterworths, London, 1977.
25. G. Thomas, *Transmission Electron Microscopy of Metals*, John Wiley & Sons, New York, 1962.
26. H. Bethge, J. Heydenreich (eds), *Elektronenmikroskopie in der Festkörperphysik*, Springer, Berlin, 1982.
27. S. Amelinckx, R. Gevers, J. Van Landuyt (eds), *Diffraction and Imaging Techniques in Material Science*, North-Holland, Amsterdam, 1978.
28. S. Amelinckx, D. Van Dyck, J. Van Landuyt, G. Van Tendeloo (eds), *Electron Microscopy, Principles and Fundamentals*, Wiley-VCH, Weinheim, 1997.
29. S. Amelinckx, D. Van Dyck, 'Diffraction Contrast and High Resolution Electron Microscopy of Structures and Structural Defects', in *Electron Diffraction Techniques, IUC Monographs on Crystallography 4*, eds. J. Cowley, Oxford University Press, Oxford, 1–222, Vol. 2, 1993.
30. D.B. Williams, C.B. Carter, 'Transmission Electron Microscopy', *A Textbook for Materials Science*, Plenum Press, New York, 1–173, 177–345, 349–549, 553–703, 1996; 2nd edition, Plenum Press, New York, 1–193, 195–368, 371–578, 581–760, 2009.
31. J.C.H. Spence, 'Experimental High Resolution Electron Microscopy', *Monographs on the Physics and Chemistry of Materials*, Oxford Science Publications, Clarendon Press, Oxford, 1981; 3rd edition, Oxford University Press, Oxford, 2009.
32. A.K. Head, P. Humble, L.M. Clarebrough, A.J. Morton, G.T. Forwood, 'Computed Electron Micrographs and Defect Identification', in *Defects in Crystalline Solids*, eds. S. Amelinckx, R. Gevers, J. Nihoul, North-Holland, Amsterdam, 1–400, Vol. 7, 1973.
33. S. Pennycook, 'Scanning Transmission Electron Microscopy: Z Contrast', in *Handbook of Microscopy*, eds. S. Amelinckx, D. Van Dyck, J. Van Landuyt, G. Van Tendeloo, VCH, Weinheim, 595–620, Vol. 2, 1997.
34. P.D. Nellist, 'Scanning Transmission Electron Microscopy', in *Science of Microscopy*, eds. P. Hawkes, J.C.H. Spence, Springer, New York, 66–132, Vol. 1, 2008.
35. S. Pennycook, 'A Scan Through the History of STEM', in *Scanning Transmission Electron Microscopy. Imaging and Analysis*, eds. S. Pennycook, P.D. Nellist, Springer, New York, 1–90, 2011.
36. M.J. Humphry, B. Kraus, A.C. Hurst, A.M. Maiden, J.M. Rodenburg, 'Ptychographic Electron Microscopy Using High-angle Dark-field Scattering for Sub-nanometre Resolution Imaging', *Nature Commun.*, **3**, 730 (2012).
37. L. Fiermans, R. De Gryse, 'Scanning Auger Microscopy (SAM) and Imaging X-ray Photoelectron Spectroscopy (XPS)', in *Handbook of Microscopy*, eds. S. Amelinckx, D. Van Dyck, J. Van Landuyt, G. VanTendeloo, VCH, Weinheim, 621–659, Vol. 2, 1997.
38. M. Prutton, M.El. Gomani (eds), *Scanning Auger Electron Microscopy*, John Wiley & Sons, Chichester, 1–349, 2006.
39. B.G. Yacobi, D.B. Holt, *Cathodoluminescence Microscopy of Inorganic Solids*, Plenum Press, New York, 89–118, 121–268, 1990.
40. J.C.H. Spence, 'Diffractive (Lensless) Imaging', in *Science of Microscopy*, eds. P. Hawkes, J.C.H. Spence, Springer, New York, 1196–1227, Vol. 2, 2008.
41. N.D. Browning, S.J. Pennycook, 'Atomic Resolution Spectroscopy for the Microanalysis of Materials', *Microbeam Anal.*, **2**, 81–89 (1993).
42. C.E. Lyman, J.I. Goldstein, D.B. Williams, D.W. Ackland, S. Von Harrach, A.W. Nicholls, P.J. Statham, 'High-performance X-ray Detection in a New Analytical Electron Microscope', *J. Microsc.*, **176**, 85–98 (1994).
43. M.A. Baker, J.E. Castle, 'Scanning Auger Microscopy', in *Materials Science and Technology: a Comprehensive Treatment*, eds. R.W. Cahn, P. Haasen, E.I. Kramer, VCH, Weinheim, 220–239, Vol. 2B, Chapter 13, 1994.
44. C.E. Nockolds, 'Low-voltage Electron Probe X-ray Microanalysis in an In-lens Field Emission Gun SEM: an Evaluation', *Microbeam Anal.*, **3**, 185–189 (1994).
45. G.D. Danilatos, 'Environmental Scanning Electron Microscopy and Microanalysis', *Mikrochim. Acta*, **114/115**, 143–155 (1994).
46. D.A. Wollman, K.D. Irvin, G.C. Hilton, L.L. Dulcie, D.E. Newbury, J.M. Martinis, 'High-resolution, Energy-dispersive Microcalorimeter for X-ray Microanalysis', *J. Microsc.*, **188**, 196–223 (1997).

47. V. Oleshko, V. Kindratenko, R. Gijbels, P. Van Espen, W. Jacob, 'Study of Quasi-fractal Many-particle Systems by Zero-loss Spectroscopic Imaging, Electron Energy-loss Spectroscopy and Digital Image Analysis', *Mikrochim. Acta*, (Suppl. 13), 443–451 (1996).
48. R.H. Packwood, J.D. Brown, 'A Gaussian Expression to Describe  $\phi(\rho Z)$  Curves for Quantitative Electron Probe Microanalysis', *X-Ray Spectrom.*, **10**, 138–146 (1981).
49. J.L. Pouchou, 'Standardless X-ray Analysis of Bulk Specimens', *Mikrochim. Acta*, **114/115**, 33–52 (1994).
50. J.A. Small, 'Electron-induced X-ray Emission', in *Handbook of X-ray Spectrometry: Methods and Techniques*, eds. R.E. Van Grieken, A.A. Markowicz, Marcel Dekker, New York, 583–655, Chapter 12, 1993; 2nd edition, 811–932, Chapter 13, 2001.
51. J.I. Goldstein, D.B. Williams, 'X-Ray Microanalysis and Electron Energy Loss Spectrometry in the Analytical Electron Microscope: Review and Future Directions', *Microbeam Anal.*, **1**, 29–53 (1992).
52. G. Cliff, G.W. Lorimer, 'The Quantitative Analysis of Thin Specimens', *J. Microsc.*, **103**, 203–207 (1975).
53. J.I. Goldstein, 'Principles of Thin Film X-ray Microanalysis', in *Introduction to Analytical Electron Microscopy*, eds. J.J. Hren, J.I. Goldstein, D.C. Joy, Plenum Press, New York, 83–120, Chapter 3, 1979.
54. J.E. Wood, D.B. Williams, J.I. Goldstein, 'Experimental and Theoretical Determination of  $k_{AFe}$  Factors for Quantitative X-ray Microanalysis in the Analytical Electron Microscope', *J. Microsc.*, **133**(Pt. 1), 255–274 (1984).
55. R.J. Graham, J.W. Steeds, 'Determination of Cliff–Lorimer  $k$  Factors by Analysis of Crystallized Microdroplets', *J. Microsc.* **133**(Pt. 1), 275–280 (1984).
56. N. Zaluzec, 'Quantitative X-ray Microanalysis: Instrumental Considerations and Applications to Materials Science', in *Introduction to Analytical Electron Microscopy*, eds. J.J. Hren, J.I. Goldstein, D.C. Joy, Plenum Press, New York, 121–167, Chapter 4, 1979.
57. E. Van Cappellen, 'The Parameterless Correction Method in X-ray Microanalysis', *Microsc. Microanal. Microstruct.*, **1**, 1–22 (1990).
58. R.F. Egerton, 'Quantitative Analysis of Electron Energy-loss Spectra', *Ultramicroscopy*, **28**, 215–225 (1989).
59. R.F. Egerton, R.D. Leapman, 'Quantitative Electron Energy-loss Spectroscopy', in *Energy-filtering Transmission Electron Microscopy*, ed. L. Reimer, Springer, Berlin, 269–290, 1995.
60. C. Gregory, H.A. Nullens, R. Gijbels, W. Jacob, P.J. Van Espen, I. Geuens, R. De Keyser, 'Automated Particle Analysis of Populations of Silver Halide Microcrystals by Electron Probe Microanalysis under Cryogenic Conditions', *Anal. Chem.*, **70**, 2551–2559 (1998).
61. C. Jeanguillaume, Ch. Colliex, 'Spectrum-image: the Next Step in EELS Digital Acquisition', *Ultramicroscopy*, **28**, 252–257 (1989).
62. J.A. Hunt, D.D. Williams, 'Electron Energy-loss Spectrum Imaging', *Ultramicroscopy*, **38**, 47–73 (1991).
63. J.-L. Lavergne, C. Foa, P. Bongrand, D. Seux, J.M. Martin, 'Application of Recording and Processing of Energy-filtered Image Sequences for the Elemental Mapping of Biological Specimens: Image-spectrum', *J. Microsc.*, **174**(Pt. 3), 195–206 (1994).
64. D.C. Joy, 'Scanning Electron Microscopy', in *Handbook of Microscopy*, eds. S. Amelinckx, D. Van Dyck, J. Van Landuyt, G. Van Tendeloo, VCH, Weinheim, 539–561, Vol. 2, 1997.
65. R. Reichelt, 'Scanning Electron Microscopy', in *Science of Microscopy*, eds. P. Hawkes, J.C.H. Spence, Springer, New York, 133–272, Vol. 1, 2008.
66. C. Rinaudo, M. Allegrina, E. Fornero, M. Musa, A. Croce, D. Bellis, 'Micro-Raman Spectroscopy and VP-SEM/EDS Applied to the Identification of Mineral Particles and Fibres in Histological Sections', *Raman Spectroscopy*, **41**, 27–32 (2010).
67. N. Yao (ed.), 'Focused Ion Beam', *Basics and Applications*, Cambridge University, Cambridge, 1–390, 2007.
68. N.J. Zaluzec, 'Innovative Instrumentation for Analysis of Nanoparticles: The  $\pi$  Steradian Detector', *Microscopy Today*, **4**, 56–59 (2009).
69. H.S. von Harrach, P. Dona, B. Freitag, H. Soltau, A. Niculae, M. Rohde, 'An Integrated Multiple Silicon Drift Detector System for Transmission Electron Microscopes', *J. Phys.: Conf. Ser.*, **241**, 012015 (2010).
70. T. Ogiwara, T. Kimura, S. Fukushima, K. Tsukamoto, T. Tazawa, S. Tanuma, 'Analysis of Ultra Light Elements with Newly Developed Ultra-Soft X-Ray Spectrometer for Electron Probe Microanalysis', *Mikrochim. Acta*, **161**, 451–454 (2008).
71. M. Terauchi, H. Takahashi, N. Handa, T. Murano, M. Koike, T. Kawachi, T. Imazono, M. Koeda, T. Nagano, H. Sasai, Y. Oue, Z. Yonezawa, S. Kuramoto, 'Ultrasoft-X-Ray Emission Spectroscopy Using a Newly Designed Wavelength-Dispersive Spectrometer Attached to a Transmission Electron Microscope', *J. Electron. Microsc.*, **61**, 1–8 (2012).
72. F. Banhart, *In Situ Electron Microscopy at High Resolution*, ed. F. Banhart, World Scientific, Singapore, 1–14, 2008.
73. F. Ross, 'In Situ Transmission Electron Microscopy', in *Science of Microscopy*, eds. P. Hawkes, J.C.H. Spence, Springer, New York, 445–534, Vol. 1, 2008.
74. W.E. King, M.R. Armstrong, O. Bostanjoglo, B.W. Reed, 'High-Speed Electron Microscopy', in *Science of Microscopy*, eds. P. Hawkes, J.C.H. Spence, Springer, New York, 406–444, Vol. 1, 2008.

75. A.H. Zewail, 'Four-Dimensional Electron Microscopy', *Science* **328**, 187–193 (2010).
76. A.W. Robards, A.J. Wilson (eds), *Procedures in Electron Microscopy*, John Wiley & Sons, Chichester, 15, 1.4–15: 1.5, 15: 2.10–15: 2.24, 15: 5.1–15: 5.6, 1993, 1996, 1997.
77. P. Echlin, *Handbook of Sample Preparation for Scanning Electron Microscopy and X-Ray Microanalysis*, Springer, New York, 1–322, 2009.
78. V.P. Oleshko, J.M. Howe, 'In situ Determination and Imaging of Physical Properties of Metastable and Equilibrium Precipitates Using Valence Electron Energy-Loss Spectroscopy and Energy-Filtering Transmission Electron Microscopy', *J. Appl. Phys.*, **101**, 054308 (2007).
79. V.P. Oleshko, 'The Use of Plasmon Spectroscopy and Imaging in a TEM to Probe Physical Properties at the Nanoscale', *J. Nanosci. Nanotechnol.*, **12**, 8580–8588, (2012).
80. V.P. Oleshko, P.A. Crozier, R.D. Cantrell, A.D. Westwood, 'In Situ Real-Time Environmental TEM of gas Phase Ziegler-Natta catalytic Polymerization of Propylene', *J. Electron Microsc.* **51**(Suppl. 2), S27–S39 (2002).
81. V.P. Oleshko, J.M. Howe, 'Are Electron Tweezers Possible?', *Ultramicroscopy*, **111**, 1599–1606 (2011).